Chair of Functional Materials and Materials Systems

Doctoral Thesis

Pathways Towards the Functionalization of Three-Dimensional Substrates

Dipl.-Ing. Florian Knabl, BSc

April 2024

MONTANUNIVERSITÄT LEOBEN
www.unileoben.ac.at

AFFIDAVIT

I declare on oath that I wrote this thesis independently, did not use any sources and aids other than those specified, have fully and truthfully reported the use of generative methods and models of artificial intelligence, and did not otherwise use any other unauthorized aids.

I declare that I have read, understood and complied with the "Good Scientific Practice" of the Montanuniversität Leoben.

Furthermore, I declare that the electronic and printed versions of the submitted thesis are identical in form and content.

Date 22.04.2024

Signature Author
Florian Knabl

Acknowledgments

My deepest gratitude goes out to Christian Mitterer, an exceptional supervisor who has guided me tirelessly. His trust and the opportunity to prove myself at such a challenging level have been invaluable, pushing me to become a better scientist. I am also profoundly grateful to my mentor, Oskar Paris, for his unwavering support that continued from master's thesis into this current work. His guidance was vital in both our experimental work and data analysis, as well as in enriching our Porous Materials Group discussions.

I would also like to acknowledge my fabulous colleague, Nikolaos Kostoglou, who has set an outstanding example with his scientific rigor and work ethics. More than just a colleague, Nikolaos has been a good friend and a cornerstone of support, making this phase of my life both challenging and enjoyable.

I extend my gratitude to my colleagues at the Chair of Functional Materials and Materials Systems, whose invaluable support made this thesis possible and brought joy to my work. Special thanks to Fabian Konstantiniuk, Velislava Terziyska, Anna Hofer-Roblyek, Karl-Heinz Pichler, Aydan Cicek, Lukas Kölbl, Christian Saringer, Michael Tkadletz, Stefan Zeiler, Alexander Blocher, Nafsika Mouti, and Serena Naicker. I am also grateful to Maximilian Koravitsch and Alessandro Togni for their pioneering work in the early stages of this dissertation. My thanks extend to Christine Bandl and Thomas Grießer from the Department of Polymer Engineering and Science for their support. Furthermore, I am profoundly thankful to collaborate with Dominik Gutnik and Barbara Putz from both the Chair of Structural and Functional Ceramics and EMPA, whose expertise has been invaluable.

I would also like to extend my appreciation to my cooperation partners at other universities, highlighting the valuable contributions and collaborations towards this work. Special thanks to Steven Hinder and Mark Baker at the University of Surrey, Etienne Bousser and Ludvik Martinu at Polytechnique Montréal, Claus Rebholz at the University of Cyprus, Prathamesh Patil and Christian M. Pichler at the CEST Centre for Electrochemistry and Surface Technology GmbH, Tijmen Vermeij from Empa, Afshin Tarat from Loginns GmbH, and Ram K. Gupta at Pittsburg State University, and to my colleagues at the University of West Bohemia in Plzeň. Finally, I appreciate the fierce scientific debates with Jochen Schneider and his team at the RWTH Aachen, which have been immensely stimulating and rewarding.

Lastly, my sincere thanks go to my family and my girlfriend's family for their unwavering support, and a big shoutout to my friends for always being there. Most importantly, to my girlfriend Alexandra, whose endless love has been my anchor. You are the best partner I could ever wish for, making this journey not just possible but meaningful.

"Plus one minus one equals zero. That's a defeatist attitude."

Jack White. Musician. Potential mental coach. Not a scientist.

Abstract

Materials science has always been on the forefront of human progress, with a current focus on developing functional materials. These materials are designed to perform sophisticated tasks beyond mere structural applications. This necessitates advanced synthesis strategies that synergistically combine the properties of various constituent phases into high-performance nanocomposite material systems.

This thesis explores three distinct physical surface modification methods to develop advanced material systems: dielectric barrier discharge plasma treatment on a mixture of few-layer graphene and cobalt powder, conventional magnetron sputtering on nanoporous carbon cloth, and magnetron sputter inert gas condensation for nanoparticle deposition on silicon substrates. The first method produces a cobalt-graphene nanocomposite with enhanced electrochemical performance, with potential scalability to three-dimensional substrates when employing an additional binder phase. The second method creates a nanocomposite of activated carbon cloth with palladium islands, showcasing successful functionalization of flexible three-dimensional substrates with potential applications as energy materials and sensing. The third approach enhances process control and deposition rates for nanoparticle depositions via magnetron sputter inert gas condensation. Initially, quadrupole mass spectrometry is employed for in situ measurements to advance process control. Subsequently, applying a substrate bias voltage significantly increases the output of nanoparticles from the source, thus incrementally improving this method for future research and applications.

To summarize, this thesis presents significant advancements in three physical surface modification methods, highlighting their respective capabilities in functionalizing surfaces and showing pathways towards the functionalization of three-dimensional substrates, marking an important step forward towards the industrial application of advanced high-performance nanocomposite materials.

Kurzfassung

Die Materialwissenschaft stand schon immer an vorderster Front des menschlichen Fortschritts, mit einem aktuellen Forschungsschwerpunkt auf der Entwicklung funktionaler Materialien. Diese Materialien sind darauf ausgelegt, anspruchsvolle Aufgaben jenseits bloßer struktureller Verwendung hinaus zu erfüllen. Das erfordert fortschrittliche Synthesestrategien, die die Eigenschaften verschiedener Materialen synergetisch in leistungsfähigen Nanokompositmaterialien kombinieren.

Diese Dissertation erforscht drei unterschiedliche Verfahren der physikalischen Oberflächenmodifikation zur Entwicklung solcher fortschrittlicher Materialsysteme: Dielektrische Barriereentladungs-Plasmabehandlung einer Mischung aus Graphen und Kobaltpulver, konventionelles Magnetronsputtern auf Aktivkohle-Fasergewebe und Magnetronsputter-Inertgas-Kondensation für die Nanopartikelabscheidung auf Siliziumsubstraten. Das erste Verfahren produziert einen Kobalt-Graphen-Nanokomposit mit verbesserter elektrochemischer Leistung und mit potenzieller Skalierbarkeit auf dreidimensionale Substrate unter Verwendung einer zusätzlichen Binderphase. Das zweite Verfahren erzeugt einen Nanokomposit aus Aktivkohle-Fasergewebe mit Palladium-Inseln. Damit wird die erfolgreiche Funktionalisierung flexibler dreidimensionaler Substrate demonstriert, mit potenziellen Anwendungen als Energiematerialien und für Sensorik. Das dritte Verfahren verbessert die Prozesskontrolle und die Abscheidungsraten für Nanopartikelabscheidungen durch Magnetronsputter-Inertgas-Kondensation. Zunächst wird die Quadrupol-Massenspektrometrie für *in-situ*-Messungen zur Verbesserung der Prozesskontrolle eingesetzt. Anschließend führt das Anlegen einer Substratspannung zu einer signifikanten Erhöhung der Nanopartikelausbeute aus der Quelle, was diese Methode schrittweise für zukünftige Forschung und Anwendungen verbessert.

Zusammenfassend demonstriert diese Dissertation bedeutende Fortschritte in drei Methoden der physikalischen Oberflächenmodifikation, hebt ihre jeweiligen Fähigkeiten zur Funktionalisierung von Oberflächen hervor und zeigt Wege zur Funktionalisierung dreidimensionaler Substrate. Damit stellt sie einen wichtigen Schritt in Richtung der industriellen Anwendung fortschrittlicher Hochleistungs-Nanokompositmaterialien dar.

Content

1 Introduction

Materials science has always been on the forefront of human progress, giving rise to the name of eras such as the Stone Age, the Bronze Age, the Steel Age, the Polymer Age, and the current era, often referred to as the Silicon Age. Further progress in materials science is conducted by creating advanced nanocomposite materials, combining the beneficial properties of two or more materials, resulting in functional materials which serve roles beyond structural support. This advancement has led to the practice of functionalization, that is the modification of the surface of a given material with the goal of fulfilling a certain functionality [1]. Such applications are found in energy storage [2], adhesive materials as found in geckos [3] and frogs [4], superconductors [5], and perhaps most importantly, semiconductors [6].

Surface properties can be tailored by directly changing its physical properties or by applying additional materials, such as thin films, to significantly enhance the material system's capabilities. Such surface modifications can be performed by a wide variety of physical and chemical methods. Among the various physical methods explored in this thesis, plasma treatment stands out for its ability to create pore structures and dope surfaces with specific elements. Two examples of physical vapor deposition techniques, conventional magnetron sputtering (MS) and the more sophisticated magnetron sputter inert gas condensation (MS-IGC), allow for functionalization of a given substrate surface under vacuum conditions, obtaining a unique microstructure of the material with high purity. Simultaneously the pitfalls associated with chemical methods are avoided, such as the need for wet chemistry steps and possible sample contamination through chemical remnants. This thesis explores multiple physical functionalization pathways, stretching from powder to three-dimensional substrates, to unlock new applications and understandings in materials science.

The thesis is organized into the following chapters. Chapter 2 presents a variety of substrate materials used for surface functionalization investigations. Chapter 3 introduces the physical methods employed, including (a) plasma modification, (b) conventional MS, and (c) MS-IGC. Chapter 4 explores the most important characterization methods employed within the four publications. Chapter 5 discusses the findings in the context of the wider field, and Chapter 6 offers an outlook on future research directions, transcending the scope of the individual publications included.

Chapter 8 compiles the four constituting publications developed over the course of this thesis, each contributing uniquely to the field of surface functionalization. Publication I deals with the functionalization of a powder-like cobalt-carbon nanocomposite used for advanced electrochemical applications. Publication II investigates magnetron sputtering on

short time scales, achieving small palladium islands on the surface of the three-dimensional nanoporous carbon substrate with an outlook highlighting its potential applications. Publication III provides insights into the first steps of nanoparticle (NP) deposition on conventional two-dimensional silicon substrates, highlighting a newly developed method capable of determining *in situ* the NP size distribution and NP flux using specific MS-IGC synthesis parameters. This enables future researchers to conduct depositions with increased confidence on the quantity and properties of deposited NPs. Publication IV builds upon the fundamentals developed in Publication III, demonstrating that the output of NPs from the NP source is increased by applying a substrate bias voltage, thereby enhancing process efficiency and taking a step towards a breakthrough in large-scale surface modification via MS-IGC.

Together, these publications represent a significant advance in surface functionalization techniques, offering novel insights and methodologies that contribute to the field. This thesis enhances the current scientific understanding of physical surface functionalization methods and successfully highlights pathways towards the functionalization of three-dimensional substrates.

2 Substrates

The term *substrate* refers to the base material on which processing is conducted [7]. The substrate, and in particular the substrate surface, has a strong influence on the thin film deposited on top. For instance, a hard coating applied to a soft underlying material may not perform effectively if it fractures due to the deformation of the substrate when subjected to stress. The type of substrate that can be functionalized by a given technology strongly affects possible large-scale industrial applications. Physical vapor deposition processes are line-of-sight processes and thus are primarily used for covering two-dimensional substrates. However, this issue can be partially remedied by rotating substrates along multiple axes for a more uniform three-dimensional coating [7]. Given this significant influence, the choice of substrate—be it powders, conventional 2D substrates, or nanoporous 3D substrates—plays a crucial role in the technology's application and scalability.

2.1 Powders

A powder is a dry, bulk solid composed of many very fine particles that may flow freely when shaken or tilted. Powders are particularly relevant for activated carbon (AC), a class of carbon materials characterized by very large specific surface areas up to 3000 m^2/g [8]. It is commonly synthesized by means of physical or chemical activation of a wide variety of precursor materials [9]. While AC is commonly synthesized as a powder, this is a rather unfavorable morphology for multiple practical applications. Thus powders can be transformed into more practical shapes such as granules [10], pellets [11], and monoliths [12] by a variety of different techniques, typically involving the addition of a binder. Furthermore, extruded activated carbon is synthesized in the shape of cylinders, also using an additional binder phase [13]. Few-layer graphene, a variant of graphene, is based on two-dimensional individual graphene layers. Macroscopically such materials commonly exist as powders [14].

Publication I investigates a mixture of a nanoporous few-layer graphene with cobalt particles, with a macroscopic powder appearance. While the characterization of the material system was carried out as a powder, one can easily imagine a process inspired by nanoporous activated carbon to create three-dimensional functionalized materials of a desired shape.

2.2 Conventional 2D Substrates

The most commonly used substrate in thin film depositions on the laboratory scale are single crystal silicon wafers. Silicon is synthesized from a molten state into single crystals on industrial scale with an outstanding chemical purity required for integrated circuits. To produce the silicon substrate, the single crystals are cut into slices using a diamond saw and then finely polished to create wafers with minimal surface roughness. Wafers are commonly

cut into small pieces in the laboratory scale [7]. The native SiO_2 top layer may be removed by additional chemical cleaning or plasma etching steps prior to surface functionalization.

Beyond the conventional silicon substrates, a large variety of substrates was reported for depositing NPs by means of MS-IGC. Examples include highly ordered pyrolytic graphite [15–17], glass substrates [18], glassy carbon [16], and unspecified graphite [19]. Furthermore, quasi-2D textile substrates such as nonwoven viscose fabric [20] and carbon cloth [20] were reported.

In Publications 3 and 4 conventional silicon substrates are used.

2.3 Nanoporous 3D Substrates

Materials with a highly developed pore structure, such as AC, embody three-dimensional substrates because their extensive porosity effectively turns their entire volume into active surface area. Graphene, another prominent carbon allotrope heavily investigated since its initial discovery in 2004 [21], yields a theoretical specific surface area of 2630 m^2/g [22], assuming a single infinitely long sheet. This number can be further enhanced by adding holes into the sheet structure. Furthermore, such materials, much like real-life paper, can be crumbled; thus yielding a three-dimensional structure out of a two-dimensional state [23]. The apparent specific surface area is typically presented based on calculations following the Brunauer–Emmett–Teller (BET) method [24], which tends to overestimate the specific surface area for materials with a strongly developed pore structure.

Pores are small openings in a solid substance. If their sizes reach below 100 nm, they are referred to as nanopores. According to the standard by the International Union of Pure and Applied Chemistry (IUPAC), nanopores can be further subdivided according to their size or width into (1) macropores (> 50 nm), (2) mesopores (2 – 50 nm), and (3) micropores (< 2 nm), with another subdivision available for the smallest category into (a) super-micropores (0.7 – 2 nm) and (b) ultra-micropores (< 0.7 nm) [25]. Furthermore, pores can be classified according to their accessibility (e.g. open, closed) and their shape (e.g. slit-shaped, cylindrical). If all pore sizes are present, the material may be described as hierarchically porous [26]. Pore structures can be characterized using gas sorption analysis (see chapter 0).

Carbon fibers can be arranged in a textile-like manner, forming woven or non-woven carbon cloth materials, with SEM micrographs of the later depicted in Figure 1. Such flexible 3D carbon cloth materials are highly relevant due to their combination of unique properties such as a high electric conductivity, good flexibility, a self-standing structure that can be handled much more easily compared to powders, as well as strong mechanical properties [27]. Carbon fiber cloths with an internal pore structure are a highly hierarchical material, bridging

multiple length scales from a macroscopic level down to ultra-micropores in the sub-nanometer regime. Recent research examples of such materials include the application of flexible 3D carbon cloth as high-performing electrode for energy storage and conversion [28] as well as a versatile material for hydrogen adsorption, selective gas separation and electrochemical energy storage [29]. Commercial carbon cloth was suggested as a substrate material for lithium metal batteries [27].

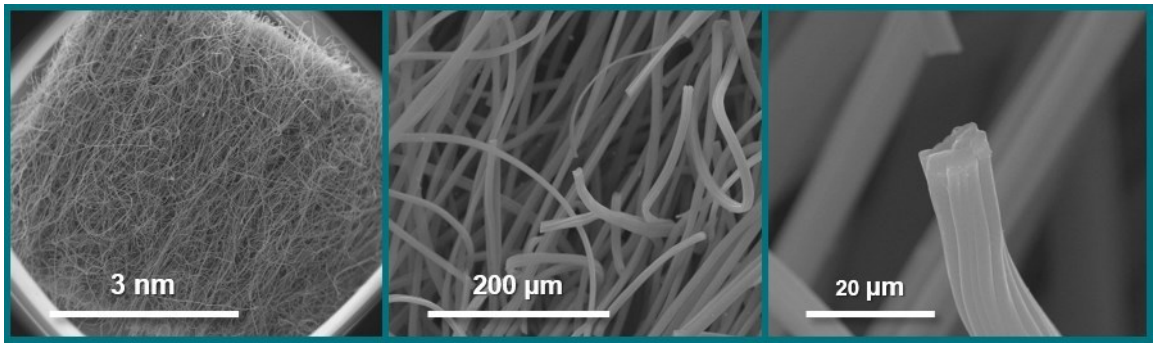

Figure 1: Collection of exemplary SEM micrographs of non-woven activated carbon cloth, unpublished results.

In Publication II a flexible activated carbon cloth substrate is functionalized on its surface using short-time magnetron sputtering, thus creating a three-dimensional carbon-palladium nanocomposite material with the potential for large-scale industrial applications.

3 Physical Surface Modification Methods

A multitude of physical surface modification methods is currently used in both academia and industry. This includes plasma treatments [14], spark discharge [30], as well as various physical vapor deposition (PVD) methods [7] such as cathodic arc evaporation, electron beam evaporation, and magnetron sputtering, MS-IGC, and atomic layer deposition [31]. In addition to physical techniques, NP synthesis also utilizes chemical methods, including chemical vapor deposition [32], sol-gel methods [33], electrodeposition [34], and thermal decomposition [35].

PVD techniques involve the evaporation of material atoms or molecules from a solid or liquid source. These vaporized particles then travel through a vacuum or a low-pressure gas environment before condensing on a substrate, forming a thin film, which is defined as having a thickness below 1000 nm. Beyond this threshold the deposited material is often referred to as a coating [7]. PVD methods are versatile, allowing for the deposition of elemental, alloy, and compound materials, as well as selected polymeric materials. These methods are able to deposit a wide range of inorganic and some organic materials through environmentally friendly processes. The resulting coatings can be single-layered, composed of graded layers, multilayered thin films, or even thick coatings, showcasing the method's adaptability for various applications [36]. The most important PVD process as of now is magnetron sputtering, an atomistic deposition process carried out in a vacuum chamber with outstanding versatility. The material is deposited atom-by-atom. A more detailed description of magnetron sputtering is given in chapter 3.2. MS-IGC represents an additional development step based on magnetron sputtering, in which NPs are created within the gas phase of a vacuum chamber. The NPs are guided onto a substrate and deposited on the surface, possibly forming a thin film depending on deposition conditions, one nanoparticle at a time. A detailed description of MS-IGC is given in chapter 3.3.

3.1 Plasma Treatments

A plasma is a quasi-neutral gas consisting of a mixture of positively or negatively charged ions, negatively charged electrons, as well as neutral species. The presence of charged species makes a plasma electrically conductive. Plasma treatments are employed for various types of surface modifications, including surface activation [37], surface modification [38], surface doping [39], surface etching [40], and cleaning surfaces of adventitious carbon and other organic compounds [41].

A common plasma treatment method for surface functionalization is called dielectric barrier discharge, representing an electric discharge between two electrodes separated by an

insulating dielectric barrier, first reported in 1857 by Ernst Werner von Siemens [42]. Recently this method was employed for creating highly dispersed catalysts, defect-rich catalysts and heteroatom-doped catalysts [43]. Such processes can be easily used for surface modifications on the large industrial scale, as they combine the ease of atmospheric pressure operation and the advantageous properties of non-equilibrium plasma with outstanding scalability [44].

In an earlier study performed by the group at Montanuniversität Leoben [14] and within Publication I of this thesis, powders are subjected to both an argon and an oxygen plasma treatment step for enhancing material surface properties in a dielectric barrier discharge reactor. Furthermore, plasma cleaning steps were performed for Publications III and IV to ensure surface cleanliness prior to depositions within a vacuum chamber and prior to measurements such as scanning electron microscopy and X-ray photoelectron spectroscopy to minimize the influence of adventitious carbon on characterization results [45,46].

3.2 Magnetron Sputtering

Sputtering describes a process in which a target is bombarded by energetic ions generated in a glow discharge plasma, situated in front of the target. The bombardment causes the ejection of individual target atoms into the gas phase, which then condense onto the substrate in a thin film. Sputtering can be most effectively achieved through the exposure of a cathode target to a gas discharge, which could be either a direct current (DC) discharge or a magnetron sputtering discharge [47]. The sputtered neutrals and ions (typically only a small fraction of the ejected particles are ionized — on the order of 1 percent) can travel ballistically from the target in straight lines and impact energetically on the substrates or vacuum chamber, forming a thin film. Sputter deposition usually uses noble gases, as those will not react with the target material. Ar is particularly common, as it is easily available and comparatively cheap while allowing a high sputter yield due to an efficient momentum transfer during collision processes. In reactive magnetron sputtering, a mixture of noble gases and reactive gases such as O_2 or N_2 are used for creating oxide and nitride thin films [48].

Within Publication II, magnetron sputtering is used on short time scales of a few seconds to functionalize the surface of a flexible activated carbon cloth substrate.

3.2.1 Direct Current Glow Discharge

Historically, the DC glow discharge has been significant for analyzing plasma properties and for its use in applications that require a weakly ionized plasma. Due to its straightforward geometry, the DC glow discharge method has been frequently utilized in generating plasma for basic research and serves as the first example before moving on to the more complex magnetron sputtering process [47]. A glow discharge occurs when electric current flows

through a gas, creating a plasma. This is typically achieved by applying a voltage across two electrodes within a glass tube filled with gas at low pressure. Once the applied voltage surpasses the so-called striking voltage, the ionization of the gas maintains itself, causing the tube to emit a colored glow. The specific color of the light emitted is determined by the type of gas present. Such a system is depicted in Figure 2, showing a DC glow discharge within a 0.5 m long tube filled with Ne gas at a pressure of 133 Pa [47]. It consists of multiple light-emitting regions (cathode layers, negative glow, positive column, anode glow) and multiple dark spaces (abbreviated with "DS" within the diagram) without light emission.

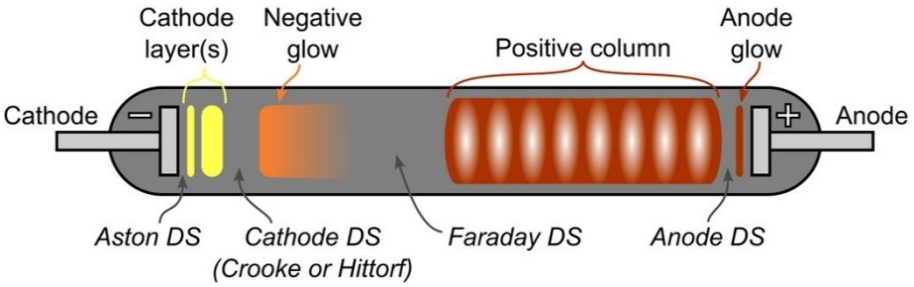

Figure 2: A schematic illustrating the DC glow discharge reveals various distinct zones located between the cathode and the anode, with the coloration of these areas representing a Ne discharge. The dark regions lack emissions of visible light and are denoted as "DS" for Dark Space. Reprinted from [47].

The dimensions, brightness, and color of the regions mentioned previously are influenced by the type of gas used, the pressure of the gas, and the voltage applied. Additionally, certain features might not be present across specific ranges of these parameters. The electric field, the electric potential, electron and ion densities, and other parameters are not equally distributed between cathode and anode, with more detailed descriptions available in the literature [47].

Fundamental work on the glow discharge was carried out by Paschen already in 1889 [49]. Paschen's law describes an equation linking the breakdown voltage V_B — the required voltage to initiate a discharge or electric arc — between two electrodes in a gas, with the product of the pressure p and the distance L between the electrodes. The breakdown voltage as a function of pL follows a "U" shaped curve (Paschen curve), with a minimum breakdown voltage at intermediate pL values [48].

The DC glow discharge can be operated as a sputter source, referred to as DC glow discharge sputter deposition. The shortcomings encompass a reduced sputtering and consequently deposition rate, contamination of the target by reactive substances, heating of the substrate caused by electrons being accelerated away from the cathode target, and the

limitation that only materials with sufficient electrical conductivity can serve as sputter targets [47].

3.2.2 Fundamentals of Magnetron Sputtering

The fundamental principal of magnetron sputtering was first proposed by Penning in 1936 with the goal of extending the lifetime of the electrons escaping from the cathode, and trapping them in the vicinity of the cathode target [50]. The addition of a magnetic field increases ionization, resulting in enhanced deposition rates and enabling operation at comparatively low working gas pressures.

A schematic drawing of a state-of-the-art conventional magnetron sputter head is given in Figure 3. In the planar circular setup, the magnetron sputtering discharge is enhanced by the inclusion of two concentric cylindrical magnets located directly behind the cathode target, which is kept at a negative potential typically between -300 and -700 V, and cooling water is employed to avoid overheating of the target material and the magnets. Surface erosion caused by the impinging Ar^+ ions occurs preferentially at regions with the magnetic field parallel to the target surface due to the enhanced electron density in this region. This causes the development of a “race track” along the target surface, which in turn affects the sputter yield and thus the deposition rate. The plasma density in the vicinity of the target is significantly higher compared to the glow discharge [51].

Different types of gases can be introduced beyond noble gases, e.g. N_2 and O_2 in the case of reactive magnetron sputtering, allowing to synthesize nitride and oxide thin films [48]. The target is surrounded by a grounded ring serving as the anode. In the case of conventional magnetron sputtering, the sputter target is kept at a constant negative potential. The working pressure is typically kept in a range of 0.1 to 1.5 Pa, allowing for a sputter deposition process largely free of collisions, in which the deposition rate is restricted by the target power [47]. Consequently, the atoms sputtered from the target largely retain their initial energy of a few eV received during the sputtering event. The sputtered material exhibits a very low degree of ionization, frequently around 0.1 % or even less [52].

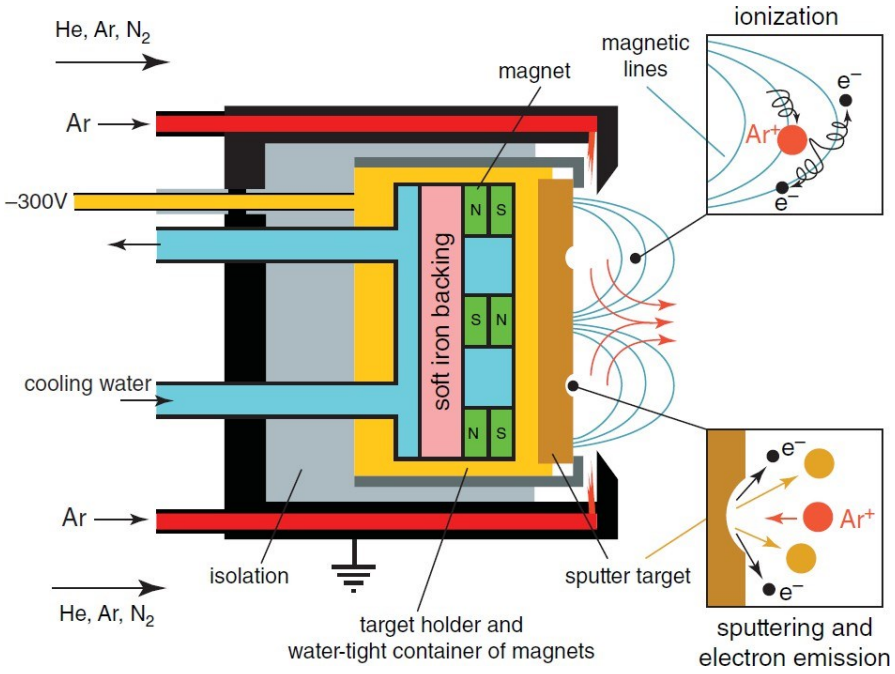

Figure 3: Cross-sectional schematics of a conventional magnetron sputter head, illustrating the setup for sputter deposition. The sputter target is bombarded with Ar^+ ions, causing the ejection of individual target atoms along with secondary electrons. These electrons are trapped by the magnetic field lines, depicted here running parallel to the target surface, contributing to the formation of a "race track" erosion pattern due to increased atom removal. Reprinted from [51].

Multiple different magnetron sputter processes were developed based on conventional direct current magnetron sputtering. Radio-frequency magnetron sputtering greatly reduces the build-up of electrical charges and features a wider race track and thus larger target utilization [7]. Reactive magnetron sputtering allows to deposit compound thin films by incorporating the reactive gas atoms into the thin film structure [53]. High-power impulse magnetron sputtering (HiPIMS) utilizes high power pulses with low duty cycles to create a dense plasma and a high degree of ionization of the sputtered material, thus creates thin films with exceptional density [53].

3.2.3 Thin Film Growth and Development

Thin film growth and development is a topic of ongoing research in the thin film scientific community. Mechanisms were already investigated in the 1920s. Many observations within the thin film community resulted in three basic growth models: (1) island growth (Volmer-Weber) growth, (2) layer (Frank-Van der Merwe) growth, and (3) mixed layer and island (Stranski-Krastanov) growth, which are summarized in Figure 4 [48].

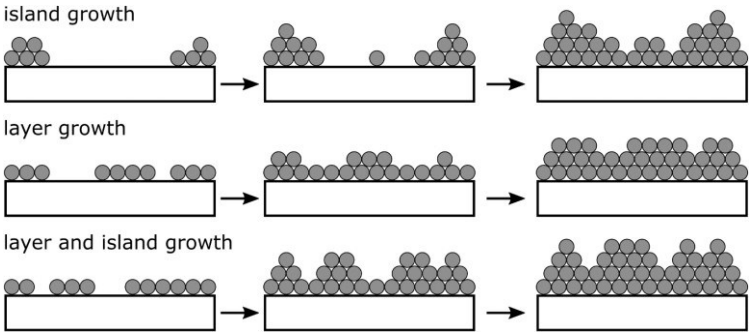

Figure 4: Basic growth mechanisms in thin films. (1) island (Volmer-Weber) growth, (2) layer (Frank-Van der Merwe) growth, and (3) mixed layer and island (Stranski-Krastanov) growth. Reprinted from [54] *and redrawn from* [48].

In island growth small clusters form which preferentially grow in three dimensions. This occurs when the deposited atoms are more strongly bound to each other compared to the substrate. Layer growth describes the opposite scenario, in which the deposited atoms preferentially bond with the substrate, thus forming a sheet structure on the surface and terminating with a quick monolayer formation. This typically occurs for homoepitaxy. The mixed layer and island growth mechanism is an intermediate step, with initial growth occurring in layers, and after completed monolayer formation commences with island mode growth characteristics [48].

The growth mode depends on a wide variety of factors, in particular the substrate material, the substrate temperature, as well as the deposition rate [48]. To provide a coherent framework for the diverse experimental observations, structure zone models have been proposed [55]. Various theoretical models were developed for describing the nucleation and growth processes. Cluster coalescence was attributed to various mechanisms, such as Oswald ripening, sintering, and cluster migration [48]. Further important factors are surface diffusion and bulk diffusion [56].

3.3 Magnetron Sputter Inert Gas Condensation

Magnetron sputter inert gas condensation (MS-IGC) is a process that uses the high sputter rate of magnetron sputtering to generate NPs via atom-by-atom condensation facilitated by collisions with inert gas. Within this unique method, collisions between sputtered atoms and inert gas molecules occur much more frequently compared to conventional MS due to a higher pressure (typically tens of Pa) and thus smaller mean free path of sputtered atoms. This promotes effective cooling and thus facilitates the coalescence into nanoclusters and subsequent growth into NPs [51]. In the next subchapters, the basic operating principle of a state-of-the-art MS-IGC deposition system is given, followed by a description of NP formation and growth mechanisms described in the literature.

In Publication III, MS-IGC is employed for the first time at Montanuniversität Leoben, successfully establishing an *in situ* methodology for measuring the NP flux, NP size distribution, and total NP output of a given MS-IGC process based on quadrupole mass spectrometry. In Publication IV, this developed methodology is employed to successfully enhance the output of NPs from the NP source using an applied substrate bias voltage. In both cases, Cu NPs on silicon substrates are utilized, the most commonly reported material system within this research community.

3.3.1 Fundamentals of Magnetron Sputter Inert Gas Condensation

The first MS-IGC source was reported by Haberland et al. in 1991 [57]. It sparked increased interest in this research topic, as it offers an increased deposition rate compared to earlier inert gas condensation methods employed for the gas phase synthesis of NPs.

Figure 5 shows a state-of-the-art MS-IGC system as reported by Johnson et al. [16], with a comparable system used for the research within this thesis [58]. It consists of a main deposition chamber, a load-lock for rapid sample exchange, as well as an NP source, which is attached on the left-hand side of the main deposition chamber. The system achieves base pressures in the ultra-high vacuum region. The NP source itself consists of a magnetron head situated within an aggregation region, in which NP formation occurs. A more detailed description of processes occurring within the aggregation region is given in chapter 3.3.2. The NPs leave the high-pressure aggregation region (pressure range of 10 – 200 Pa) through an orifice into a differentially pumped expansion zone. NP formation is assumed to stop after leaving the aggregation region, with NPs experiencing an adiabatic cooling. Many modern NP deposition systems contain a quadrupole mass spectrometer situated within the expansion zone that allows size filtration of NPs according to their mass-to-charge ratio. The NPs leaving the quadrupole filter are focused on the substrate using Einzel lenses. Substrates may be rotated and heated throughout the deposition process. Furthermore, an electric substrate bias may be applied to accelerate NPs onto the substrate. The magnetron sputter head in the presented system contains three cylindrical targets, allowing for simultaneous sputtering of three different metals.

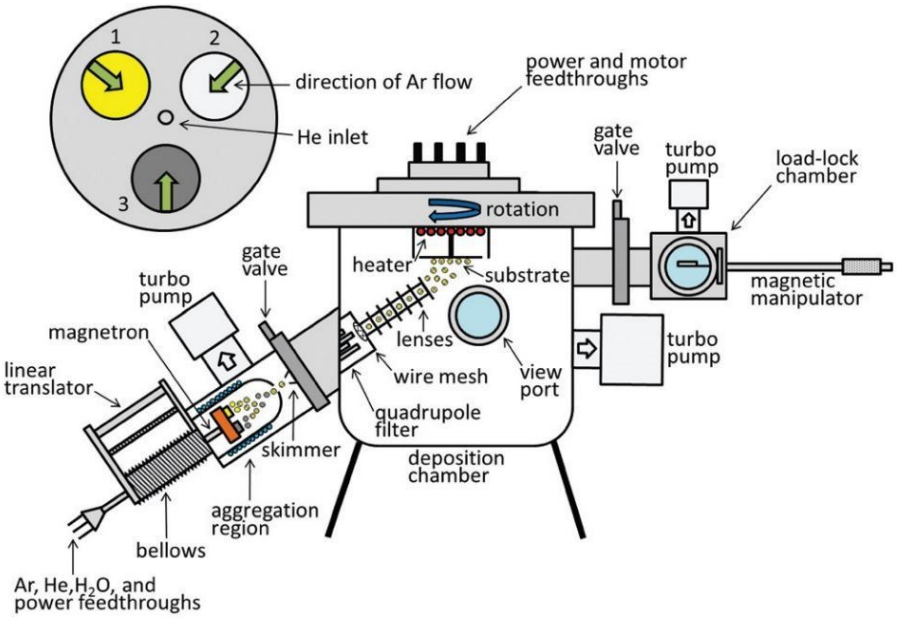

Figure 5: State-of-the-art magnetron sputter inert gas condensation system, illustrating the main deposition chamber with a load-lock mechanism for sample introduction. The nanoparticle source is attached on the left side of the deposition chamber and contains three targets within the aggregation region. Nanoparticles can be size-selected using a quadrupole mass spectrometer/filter. The QMS signal is detected at the wire mesh. Reprinted from [16].

Quite significant fractions of the sputtered material are lost, and only a small fraction reaches the substrate. Losses may be attributed to multiple effects, such as re-deposition onto the target [59], loss of material onto the aggregation chamber walls [60], as well as rejection within the quadrupole mass filter [51]. The gas flow within the aggregation chamber was investigated as a culprit of NP losses as well. Beyond that, *in situ* small-angle X-ray scattering experiments were applied to determine the growth mechanisms [61].

Multiple studies were carried out in order to understand all relevant process parameters affecting the MS-IGC deposition process. The most typically studied synthesis parameters include the sputter power/sputter current, the gas flow, the gas composition, and the aggregation length, with many studies available on different material systems. More sophisticated process parameters studied within literature include the orifice diameter [62], NP velocities of charged NPs were investigated [63], the speed of all nanoparticles including neutrals was assessed by a rotating mechanical time-of-flight filter [64], race track formation affecting both the total NP output, as well as the NP size distribution obtained by the MS-IGC process [65]. Furthermore, additional sputter techniques beyond conventional direct current MS-IGC was employed, including radio-frequency MS-IGC [66] and reactive MS-IGC [67]. Some studies investigated the influence of the addition of bimolecular or larger molecules to the gas flow, reporting on increased deposition rates. Polonskyi et al. reported that flushing the

aggregation chamber with an Ar/O_2 gas mixture significantly enhanced the deposition rate for Al NPs [68]. Marek et al. reported on a significant influence even of small additions of O_2 to the gas stream for depositing Cu NPs and Ti NPs [69].

Multiple studies investigated multi-elemental nanoparticle formation within MS-IGC systems, employing sputtering from multiple targets simultaneously or sputtering compound targets. Pérez-Tijerina et al. sputtered a compound target for achieving AuPd NPs [70], and Shelemin et al. reported on sputtering a complex compound target In_2O_3/SnO_2 target to achieve indium tin oxide NPs [71]. Johnson et al. reported on bimetallic PtRu NPs [72], and Yang et al. reported on bimetallic AuCu NPs [73], both obtained from simultaneously sputtering separate metal targets. Mattei et al. reported on trimetallic Au-Pd-Pt NPs by sputtering three metal targets simultaneously [74]. Furthermore, in-flight modification of nanoparticles was conducted by placing a conventional magnetron within the flight path of the NP beam. Kretková et al. successfully demonstrated such an attempt on Ni NPs covered with Cu [75]. Another direction of research consists of embedding NPs into a thin film. Kylián et al. reported on Cu/polymer nanocomposites obtained by combining MS-IGC with radio-frequency sputtering of a given polymer [18], and Vaidulych et al. reported on a nanocomposite consisting of Cu NPs and a thin film deposited using plasma enhanced chemical vapor deposition [20].

The charge state of the nanoparticle beam is a subject to ongoing research, as it consists of a mixture of positively charged, negatively charged, and neutral particles. Haberland et al. reported that 80 % or more of all nanoparticles leave the NP source in a charged state [57]. Polonskyi et al. reported on the relative fractions of positively charged, negatively charged, and neutral fractions within the NP beam [68,76]. Popok et al. reported that most nanoparticles synthesized by MS-IGC carry a single electric charge [77], which was later confirmed by an additional study by Zamboni et al. [78].

Different landing conditions of nanoparticles were investigated in the literature. The Haberland et al. paper already applied a substrate bias voltage to accelerate NPs onto the substrate and referred to this as energetic cluster impact as a new method for thin film formation [79]. Multiple studies were carried out on the effect of substrate bias voltage on the thin film deposition process [80–82]. Popok et al. classified the deposition conditions based on the kinetic energy per atom, differentiating between soft landing (< 0.1 eV/atom), an intermediate region, as well as nanoparticle pinning [83], with strong implications on thin film morphology and adhesion obtainable by means of MS-IGC.

Quantification of the NP beam was carried out with various techniques. Quartz crystal microbalances were used on multiple occasions to directly assess the mass flux [61,84]. As

most nanoparticles are electrically charged, they are subject to manipulation through electric fields. This allows to affect the NP beam by means of quadrupole mass spectrometers [85,86] and time-of-flight mass spectrometers [87,88], both of which are capable of determining the NP mass distribution as well as acting as a filter, allowing only selected NPs of a given mass to pass through.

3.3.2 Nanoparticle Formation and Growth

Nucleation in MS-IGC occurs in a system mainly containing buffer gas (inert gas) with an admixture of a metal vapor. If the partial pressure of the atomic metal vapor exceeds the saturated vapor pressure at the given temperature, nucleation and growth of clusters is possible [89].

Recent research has increasingly concentrated on the influence of diatomic moles, referred to as dimers [90]. The start of NP growth was thought to be caused by a three-body collision $M + M + Ar \rightarrow M_2 + Ar$, between metal atoms (M) and Ar, with a corresponding reaction rate $d[M_2]/dt = k_n [M]^2[Ar]$, in which k_n corresponds to the rate constant of the reaction [51]. However, it is argued here that a much more effective scenario is the initial formation of the molecular ion Ar_2^+.This ion has a much larger binding energy than the neutral Ar_2 and plays an important role in gas discharges [91]. As the density of argon atoms is much higher than that of the sputtered metal atoms, the condensation process probably starts by $Ar^+ + Ar + Ar \rightarrow Ar_2^+ + Ar$ with a corresponding rate constant $d[Ar_2^+]/dt = k_i [Ar]^2[Ar^+]$, and the ratio $k_i/k_n \sim 100$, which makes the second process much faster than the first one [51]. To summarize, diatomic molecules are very helpful to start the clustering process. It has been covered in multiple experiments, that the addition of diatomic (or larger) molecules increases the NP yield for a given process [92].

Following the initial nucleation step, four mechanisms of NP growth are reported in the literature and are presented in Figure 6, consisting of (a) attachment of atoms, (b) coagulation, (c) coalescence (also known as Oswald ripening), and (d) aggregation. Attachment of atoms refers to the conversion of an atomic vapor into clusters. Coagulation describes the merging of two clusters into a single one. Coalescence or Oswald ripening describes the growth of larger particles on the expanse of smaller ones. Aggregation refers to particles that are joined together, yet retain at least parts of their initial physical shape [89].

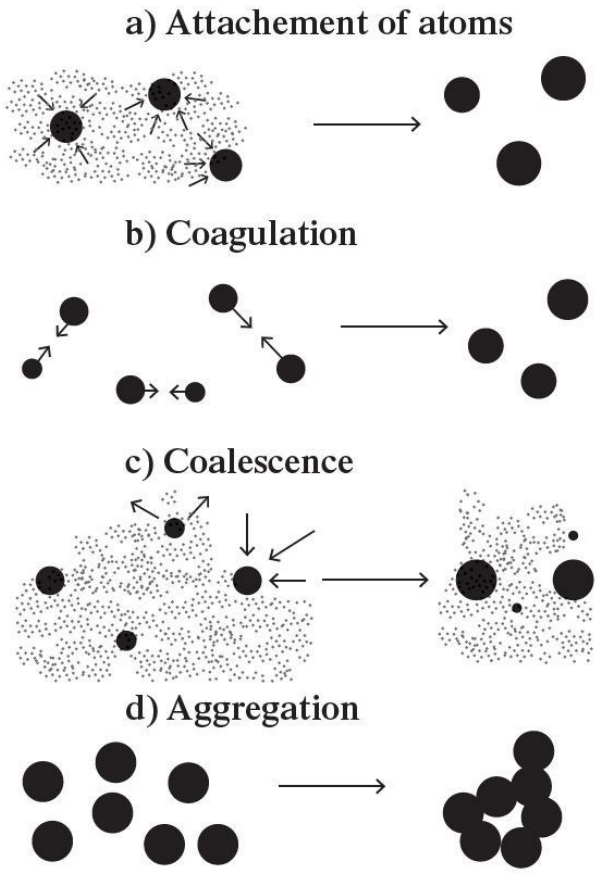

Figure 6: The growth mechanisms in clusters and nanoparticles. a) conversion of an atomic vapor in a gas of clusters; b) coagulation; c) coalescence (Ostwald ripening); d) aggregation. Reprinted from [89].

4 Selected Characterization Techniques

Within this thesis multiple characterization techniques were employed to study the properties of the synthesized materials. Characterization techniques employed in the thin film community are well-established. For MS-IGC, a detailed literature review consisting of 116 scientific publications published between 1991 and 2024 revealed popular characterization techniques employed to investigate NP depositions. The results are depicted in Figure 7. Characterization techniques marked in green are particularly relevant for the publications within this thesis and are therefore treated in more detail in subsequent chapters, along with gas sorption analysis, which is particularly relevant for nanoporous materials.

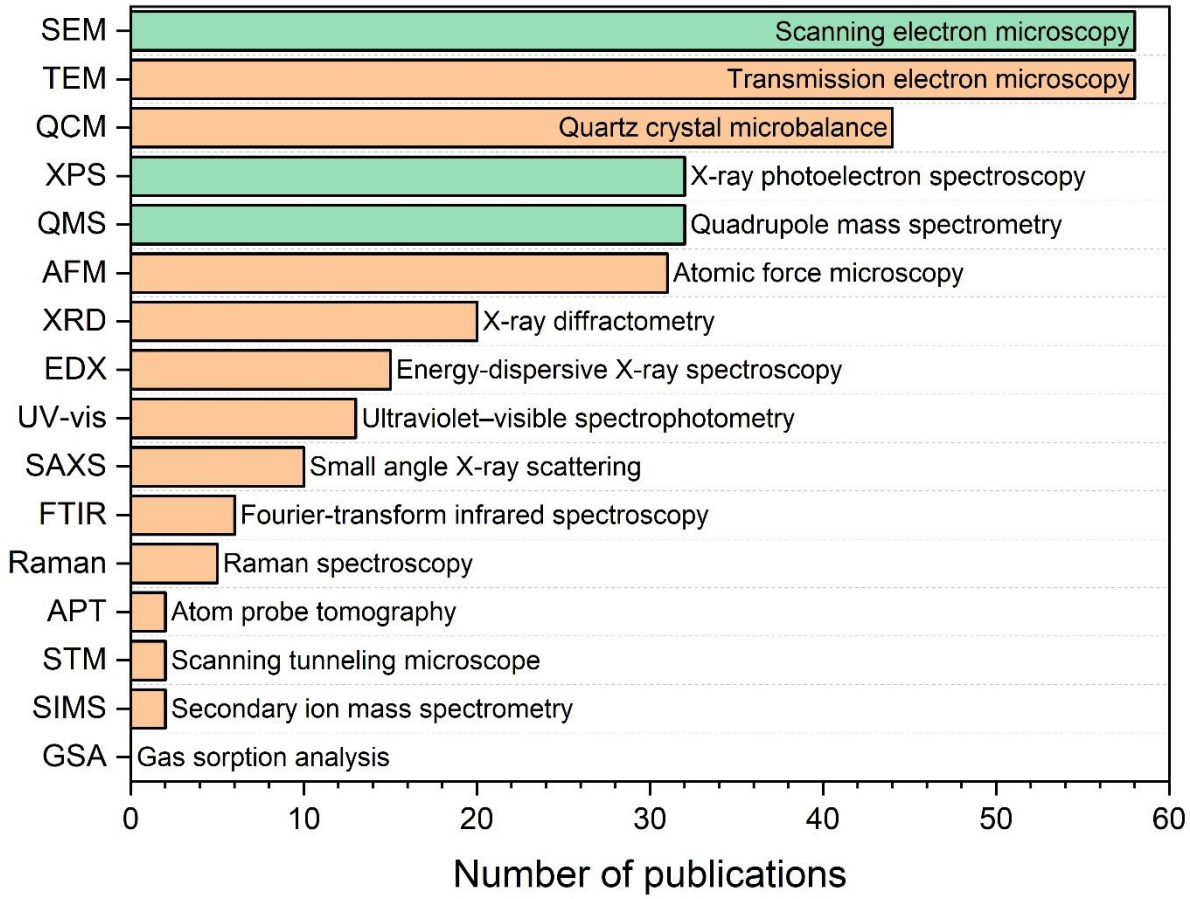

Figure 7: Systematic investigation of characterization techniques used in conjunction with materials synthesized by MS-IGC. Selected techniques investigated in subsequent chapters are marked in green color.

Electron microscopy techniques were the most popular choice, with scanning electron microscopy and transmission electron microscopy in the shared top spot. This can be easily understood; as high-quality micrographs are the cornerstone of any high-impact publication in materials science. The quartz crystal microbalance (QCM) technique and QMS were commonly used as well, with both methods within the top 5. QCM and QMS appear to be

particularly obvious choices for researchers, as they are applied *in situ* and thus are used for real-time analysis, while all other methods are typically employed *ex situ*, thus yielding results that are subjected to environmental influences on the substrate, such as adventitious carbon. The lack of any MS-IGC publications involving gas sorption analysis stands as a testament to the difficulties associated with applying this technique to complex substrates.

4.1 Scanning Electron Microscopy

Scanning electron microscopy is an imaging technique that works by scanning a focused electron beam over the surface of a given sample. The electron interaction with the material surface yields multiple signals, in particular secondary electrons and backscattered electrons, which may be used to create micrographs using topography contrast and chemical contrast, respectively. Detection of secondary and backscattered electrons is performed using different specialized detectors. The energy level of the electrons within the beam, denoted as E_0, is generally chosen to fall between 0.1 and 30 keV [93].

High quality SEM micrographs depend on a multitude of factors, including SEM hardware, SEM operating parameters, operator experience, operator motivation, vacuum quality, sample preparation, and sample cleanliness. More details on this well-established 93characterization technique are given in an outstanding textbook by Goldstein et al. [93], and an illustrative collection of SEM micrographs taken from Publication II is presented in Figure 8.

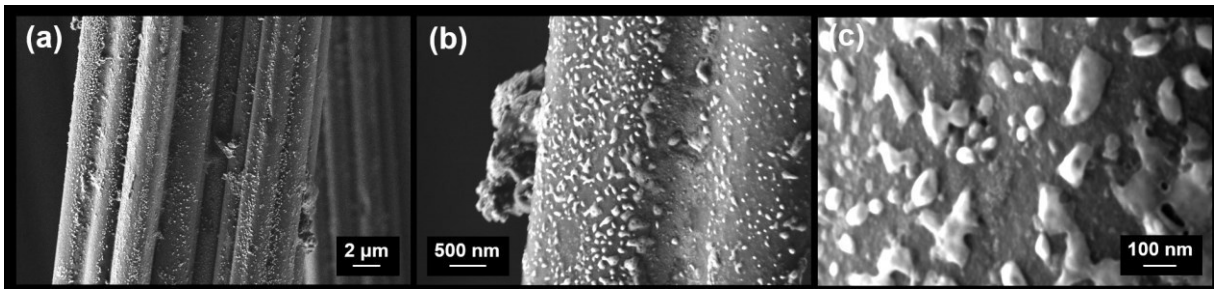

Figure 8: Collection of SEM micrographs of a palladium-doped activated carbon cloth (topography contrast) in different magnifications, showing bright palladium islands sprinkled on the dark carbon cloth surface. Reprinted from [94].

Furthermore, a scanning electron microscope is capable of measuring the elemental composition of a given sample by energy-dispersive X-ray spectroscopy (EDX). The interaction of the electron beam with the specimen yields two distinct types of X-rays, (1) a continuous X-ray background occurring for all X-ray energies below or equal to the incident beam energy E_0 and (2) characteristic X-rays with their specific energies associated to individual elements. The characteristic X-rays can always be used in a qualitative way to identify the elements present in the sample, and under certain conditions a quantification of the chemical

composition is possible. Most elements can be detected (exceptions: H, He), but reliability is low when light and heavy elements are measured simultaneously (e.g. metal-doped carbon materials) [93].

4.2 X-ray Photoelectron Spectroscopy

X-ray photoelectron spectroscopy (XPS) is a quantitative spectroscopic method sensitive to surface characteristics, utilizing the photoelectric effect to determine the elemental composition and assess bonding states of a given element. The fundamental operating principle of XPS is connected to the photoelectric effect, famously reported in 1905 by Albert Einstein [95], suggesting that light must be quantized – now referred to as photon. Einstein reported that photoelectron emission from a solid can only take place when a photon with sufficient energy strikes a material. This is referred to as the work function. Otherwise, no electron is able to escape independently of the applied light intensity.

A summary of XPS is given in Figure 9. Key elements of a state-of-the-art XPS system are the X-ray source, the monochromator, the sample, and the electron energy analyzer. The latter is relevant for the obtainable signal-to-noise ratio and the detected intensities, with both parameters related to the pass energy of the measurement. Particularly important topics for experimental work with XPS are chemical shifts, sample charging, and adventitious carbon [45].

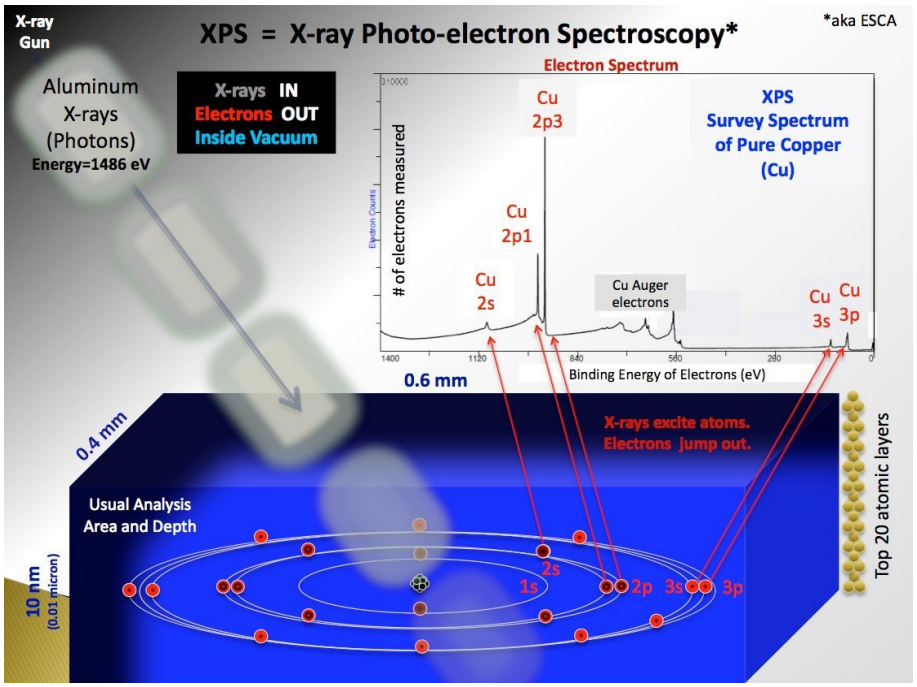

Figure 9: Summary of XPS, showcasing the approximate probed volume, as well as an XPS spectrum associated with copper, showcasing contributions from different atomic shells. Reprinted from [96].

Analyzing surfaces using XPS entails exposing a solid material in a vacuum to monochromatic soft X-rays (typically Mg Kα at 1253.6 eV or Al Kα at 1486.6 eV) and examining the energy of the electrons that are emitted. These processes are summarized in Figure 10. In more colloquial terms, XPS employs the inverse measurement principle of EDX, for which the material is irritated with electrons, and the resulting X-ray spectrum is measured. The resulting spectrum in XPS is presented as a graph, displaying the count of electrons detected within each energy interval against their kinetic energy. This process reveals a unique spectral fingerprint for each element [97]. It is customary to plot an XPS spectra with the binding energy decreasing from the left to the right.

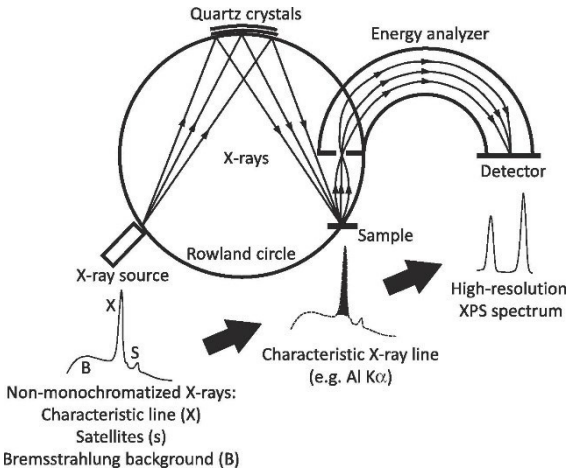

Figure 10: A schematic depiction illustrates the concept of X-ray monochromatization as used for XPS, where an X-ray source, a monochromator crystal, and a sample are positioned along the circumference of the Rowland circle. Reprinted from [45], with original inspiration from [98].

The mean free path of electrons in solids being quite short means that the electrons detected come exclusively from the uppermost atomic layers, rendering XPS an exceptionally surface-sensitive method for chemical analysis. Quantitative information can be derived from the heights or areas of peaks, while the identification of chemical states is frequently achieved through precise measurements of peak positions and their separations, in addition to specific spectral characteristics [97]. The basic equation governing XPS measurements is referred to as Einstein relation. It is given as:

$$E_{binding} = h\upsilon - E_{kin} \quad (1)$$

With $E_{binding}$ as the core-level binding energy, which can be calculated based on the incident energy of the photons (calculated as product from the Planck constant *h* and the X-ray frequency *v*) and subtracting the measured kinetic energy E_{kin} of the detected photoelectrons [45]. This simplified equation is only valid for gas-phase measurements.

The notation used for identifying core-level signals follows the format "$X\ nl_j$", where X represents the element. The principal quantum number is given by n (where n can be 1, 2, 3, …), and l indicates the angular quantum number, which is labeled as s, p, d, f for values of l = 0, 1, 2…, n−1, respectively. The j refers to the total angular momentum quantum number, which is the sum of the angular quantum number and the spin projection quantum number (s = ±1/2), thus $j = l + s$ [45].

In elemental analysis, a wide range spectrum, often referred to as a survey spectrum, is commonly captured, covering a binding energy (BE) range from 0 to greater than 1000 eV using a high pass energy. This approach ensures the detection of signatures from all species existing within the sample. After conducting the initial survey, a detailed analysis of the fundamental core-level signals of the targeted elements can be performed. This detailed analysis involves performing scans with high energy resolution across specific narrow binding energy areas, where a low pass energy is utilized. In doing so, a trade-off between the full width at half maximum and the overall duration of data acquisition has to be performed [45].

Quantitative analysis of the chemical composition of a sample surface can be performed by analyzing the measured areas under the main core-level lines of all elements presented within the sample. This requires an additional factor referred to as the relative sensitivity factor, which is an experimentally determined value specific for each core-level. The molar concentration x of an element i out of n elements present in the sample is calculated according to the following empirical equation

$$x_i = \frac{A_i/s_i}{\sum_{j=1}^{n} (A_j/s_j)}, \qquad (2)$$

with A_i as the integrated area under the corresponding core-level spectrum and s_i as the relative sensitivity factor [45]. Practically attainable detection limits are in the range of 0.1 to 1 at%. The molar concentration of a given element is strongly affected by the chosen background type. A particularly common choice is the Shirley background [45].

4.3 Quadrupole Mass Spectrometry

In the landscape of mass spectrometry, the quadrupole mass spectrometer, first presented by Paul and Steinwedel in 1953 and advanced in additional publications in 1955 and 1958 [99–101], stands as a testament to precision analysis of ions by their mass-to-charge (m/Q) ratio. It consists of an arrangement of four parallel rods as depicted in Figure 11, with charged species of a specific m/Q ratio allowed to pass through. The introduction of an ionization step prior to the rod arrangement extends the analytical capability to neutral species, allowing for a comprehensive analysis of a sample's ionic constituents. Following the rod arrangement, a detector converts the flux of ions or NPs into an electric signal.

Quadrupole mass spectrometers may be operated either in filter mode or scan mode. The former employs a constant set of the operating parameters, that is direct current voltage *U*, alternating current voltage *V*, and a frequency *f* with the corresponding angular frequency $\omega = 2\pi f$. Another important parameter is the inscribed radius between the four rods r_0, as depicted in Figure 11a. For scan mode, the voltages are kept constant while the frequency is swept through the desired range, thus ensuring a constant mass resolution throughout the whole scan range. This setup creates a dynamic electric field, which selectively stabilizes or destabilizes the paths of ions passing through based on their *m*/*Q* ratios. Only ions with specific *m*/*Q* values, determined by the applied voltages and frequency, are allowed to reach the detector, enabling the precise separation and analysis of ions within a sample. Historical use of quadrupole mass spectrometers focused on the detection of lighter species; however, technological advances have extended its capabilities, enabling the characterization of NPs [102]. Guided by the comprehensive textbook on quadrupole mass spectrometry by Dawson [103], the following section outlines the theoretical background of quadrupole operation.

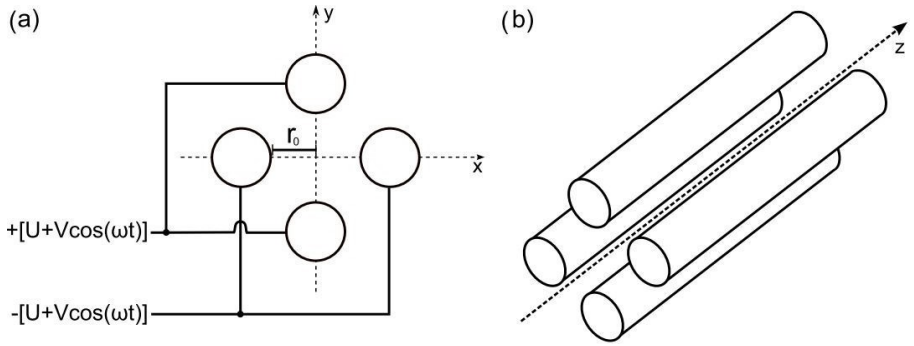

Figure 11: Quadrupole mass spectrometer with (a) a front view of the four parallel rods and the applied electric potentials and (b) 3D view of four parallel rod arrangement. Ions and NPs that match the quadrupole's filtering conditions based on their mass-to-charge ratio progress along the z-axis, while those that do not are expelled radially. Reprinted from [104].

The applied electric field within the quadrupole rods affects the charged species traversing through it. Newton's second law of motion, $F = m \times a$, with force *F*, mass *m*, and acceleration *a*, can be used to express the motion of charged species within the quadrupole field as follows:

$$\frac{d^2x}{dt^2} + \frac{e\,x}{m\,r_0^2}[U + V\cos(\omega\,t)] = 0 \qquad (3)$$

$$\frac{d^2y}{dt^2} - \frac{e\,y}{m\,r_0^2}[U + V\cos(\omega\,t)] = 0 \qquad (4)$$

$$\frac{d^2z}{dt^2} = 0 \qquad (5)$$

This indicates that charged species are subject to forces acting upon them in x and y direction, without causing acceleration along the transverse z direction. The complex equation presented above depends on multiple variables, but may be simplified into two equations by introducing the parameters *a* and *q* [100]:

$$a_u = a_x = -a_y = \frac{4eU}{m\,\omega^2 r_0^2} \quad (6)$$

$$q_u = q_x = -q_y = \frac{2eV}{m\,\omega^2 r_0^2} \quad (7)$$

In this case *u* represents either x or y directions. A further simplification is achieved by substituting $\xi = \omega t/2$, thus arriving at the Mathieu equation in its canonical form with well-established mathematical properties [99,103]:

$$\frac{d^2u}{d\xi^2} + (a_u - 2q_u \cos(2\xi))\,u = 0 \quad (8)$$

The ion trajectories within a quadrupole mass filter, governed by the Mathieu equation parameters *a* and *q*, are independent of initial conditions. These trajectories can result in stable, confined paths, or unstable ones leading to ejection of charged species from the system [103]. Whether a set of given parameters is stable, is graphically depicted in the *a*-*q* stability diagram presented in Figure 12. Multiple stability regions are possible, however, only the first region is of practical importance [105].

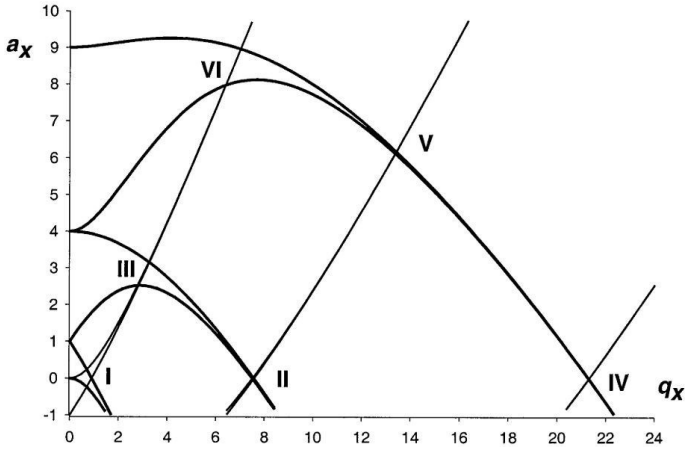

Figure 12: A comprehensive stability diagram illustrates the behavior of ion motion within the quadrupole field. Stability regions where motion in x- and y-direction are concurrently stable, are labelled with roman numerals from I to VI. Region I represents the commonly used operating regime. Reprinted from [105].

Figure 13 illustrates the first stability region of a quadrupole mass filter, characterized by its triangular shape. Within this diagram, ions with a specific mass-to-charge ratio correspond to a unique point defined by the (*a*, *q*) coordinates, which are in turn determined by the fixed values of r_0, ω, *U*, and *V*. The relationship between *a* and *q* is directly proportional

to the *U*/*V* ratio and no other parameters, allowing the construction of a mass scan line or operating line from the origin to the operating point in the stability diagram.

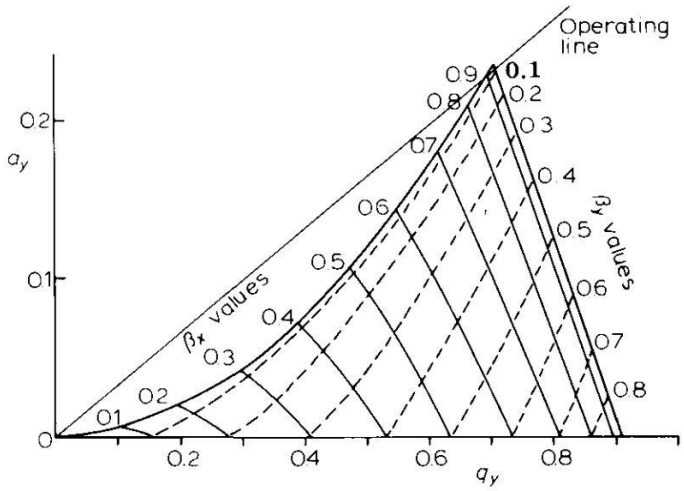

Figure 13: The stability region I commonly utilized in mass filter operations. Due to symmetry reasons only the upper half of the stability diagram is presented. Reprinted from [103].

Notably, when this line intersects the top of the triangle (*a* = 0.23699 and *q* = 0.70600), the system is theoretically capable of discriminating ions with infinite resolution. At this point, the mass of ions *m* passing through the filter can be calculated from the quadrupole's operational parameters *V*, *f*, and r_0 as [83]:

$$m = \frac{V}{7.219\, f^2\, r_0^2} \qquad (9)$$

All presented calculations implicitly assume an infinitely long quadrupole mass spectrometer [100]. Further uncertainties are introduced by the simultaneous presence of multiple charged species within the quadrupole mass spectrometer, as well as collisions with uncharged inert gas molecules. Publication III heavily utilizes quadrupole mass spectrometry for *in situ* characterization of NPs synthesized by MS-IGC, and Publication IV continuous the developed approach.

4.4 Gas Sorption Analysis

Gas sorption analysis is a characterization technique used to measure the specific surface area and the pore size distribution of a given material. The term *adsorption* refers to the enrichment of molecules, atoms or ions in the vicinity of an interface and outside of the solid structure. If the uptake takes place into the volume of the material, it is referred to as *absorption*. As both effects cannot always be strictly distinguished, *sorption* is used, describing both processes simultaneously [25].

In the process of adsorption, the substance that gets attached to the surface is referred to as the adsorbate, whereas in its fluid phase form, it is called the adsorptive. The solid material capable of performing adsorption is referred to as adsorbent. Adsorption occurs through two primary mechanisms: physical adsorption, known as physisorption, which involves weak van der Waals forces, and chemical adsorption, or chemisorption, which entails the formation of a chemical bond between the adsorbate and the surface [25].

Experimental work is performed either using the manometric method or the gravimetric method. In both cases, a sample is subjected to vacuum within a confined volume of space. In the manometric method, a known amount of pure gas is introduced to the volume. Gas molecules start to adsorb to the surface, thus lowering the pressure inside the confined volume. Once an equilibrium pressure is established, the amount adsorbed on the sample surface can be calculated based on the drop in pressure. Conversely, in the gravimetric method the mass change of the sample caused by the gas adsorption is measured directly using a vacuum microbalance [25]. This process is incremental, beginning with measurements at low pressures and gradually increasing to the maximum pressure. Figure 14 illustrates the progression of gas adsorption on a surface. Initially, adsorption occurs at energetically favorable sites. As pressure rises, a complete monolayer covers the surface. For further pressure increases, multilayer coverage is achieved.

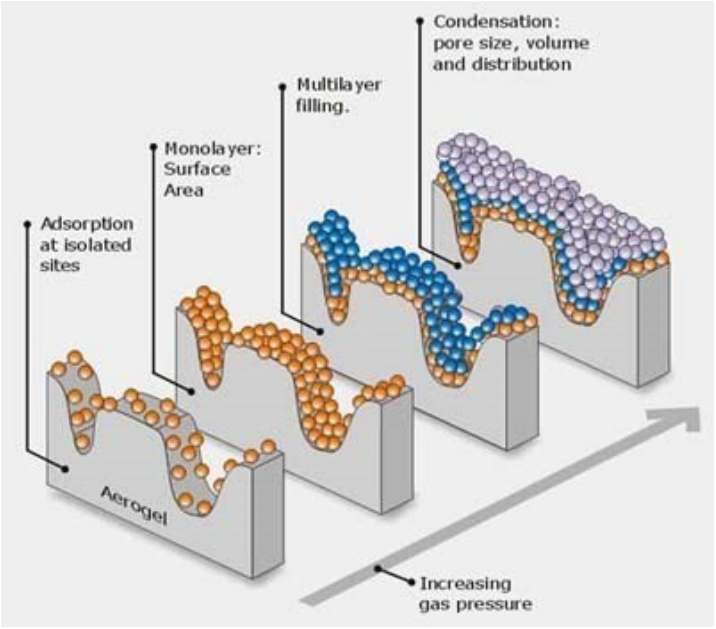

Figure 14: Stages of physisorption during gas sorption analysis as a function of pressure. Reprinted from [106].

Experimental data is typically presented as adsorption-desorption isotherms, which depict the volume of gas adsorbed by a material as a function of relative pressure P/P_0 or absolute pressure P under equilibrium conditions. The adsorption branch of the isotherm is

measured under increasing pressure, while the desorption branch is measured under decreasing pressure. A mismatch between these branches is known as adsorption hysteresis and is associated with a phenomenon referred to as capillary condensation. The choice of pressure scale – relative or absolute – depends on the adsorption conditions. When the adsorption temperature is below the critical point, the relative pressure P/P_0 is typically used, with P representing the equilibrium pressure and P_0 denoting the saturation vapor pressure at the adsorption temperature. Conversely, at adsorption temperatures exceeding the critical point, where condensation does not occur and a saturation vapor pressure P_0 is not defined, the equilibrium pressure P must be employed [25]. The shape of the adsorption isotherm is strongly related to the pore structure of the given sample, with a summary of different adsorption types given in Figure 15. Type I(a) isotherms are found for microporous materials, exhibiting a strong increase in adsorbed gas at low pressures. Type I(b) isotherms describe materials with a broader pore size range, incorporating both micro and mesopores. Type II isotherms are observed in nonporous or macroporous materials, with point B marking the completion of monolayer formation. Type III isotherms lack a defined monolayer formation point. Type IV isotherms are indicative of mesoporous materials. Type IV(a) isotherms show a distinct hysteresis behavior associated with capillary condensation. Type IV(b) isotherms occur for materials with mesopores featuring a sharp pore size distribution. Type V isotherms are obtained by weak adsorbent-adsorbate interactions. Type VI isotherms represent a layer-by-layer adsorption on highly uniform non-porous surfaces [25].

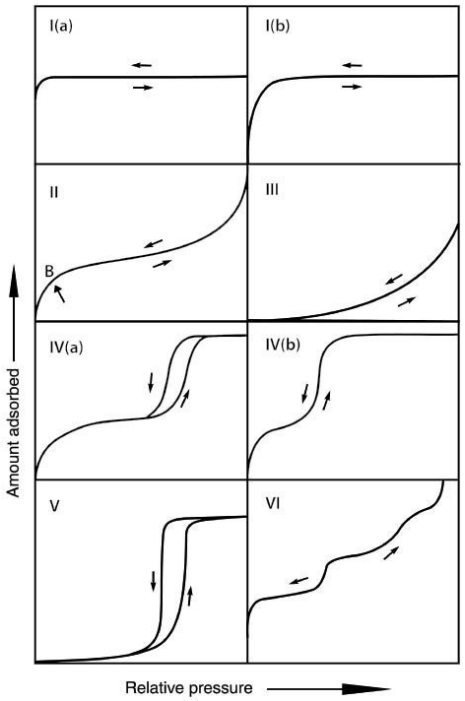

Figure 15: Classification of physisorption isotherms based on their respective isotherm shape. Reprinted from [25].

Specific surface area is commonly reported based on the BET method [24]. The micropore volume is sometimes assessed using the Gurvich rule [107]. Density functional theory and molecular simulations such as Monte Carlo simulations are employed for conducting micropore size analysis [25,108]. Within Publication I and Publication II, nanoporous materials are investigated using gas sorption analysis, and the BET method as well as quenched-solid density functional theory are employed.

5 Discussion

Publication I introduces a cobalt-doped nanoporous graphene nanocomposite, synthesized via a plasma treatment process from a few-layer graphene substrate originally derived from natural graphite. Structural analysis showed a reduction in specific surface area from 780 m^2/g to 480 m^2/g while simultaneously retaining the overall pore structure, and no detectable influences on the microstructure, including the defect density and the number of layers present within the carbon phase. Electrochemical assessments focused on supercapacitor performance and the oxygen evolution reaction in water splitting, revealing enhanced supercapacitor performance at high scanning rates and current densities. The oxygen evolution reaction performance was quantified by a Tafel slope of 110 mV/dec and an overpotential of 290 mV at a current density of 10 mA/cm^2 [109]. Despite not reaching the peak performance of similar material systems, this publication confirms that cobalt-doped nanoporous graphene nanocomposites can be effectively produced through physical synthesis methods alone, yielding a competitive electrochemical performance.

Within Publication II a novel approach for synthesizing Pd-decorated activated carbon cloth is presented. The nanocomposite is created by sputtering of a Pd target in a conventional magnetron sputter system for a short period of time in the length scale of seconds. Pd islands of various sizes and shapes were obtained, distributed around the fiber diameter, while retaining the nanoporous structure of the underlying substrate, with a moderate decrease from 1365 to 1202 m^2/g [94]. The study highlights the feasibility of functionalizing three-dimensional nanoporous substrates through a straightforward magnetron sputtering technique. It underscores the potential scalability of this approach for industrial applications, particularly through the use of large-area sputtering [110] and roll-to-roll deposition methods [111].

Publication III showcases the successful development of a method capable of determining the NP size distribution and total mass of deposited NPs for a given material system using MS-IGC in conjunction with quadrupole mass spectrometry. The methodology advances the operating principle of the quadrupole mass spectrometer to convert the measured grid current signal into an NP flux. The spatial distribution of the deposited NPs is measured using scanning electron microscopy and X-ray photoelectron spectroscopy, revealing a Gaussian distribution of the deposited Cu NPs [58].

Building upon the *in situ* methodology developed in the preceding publication, Publication IV identifies a notable increase in the quadrupole mass spectrometry signal, when a positive substrate bias voltage is applied in the MS-IGC system. The observed signal increase suggests that applying a substrate bias voltage increases the NP output from the NP source.

This hypothesis is successfully proven, showing that the *in situ* QMS signal correlates well with the surface coverage of Cu NPs on the silicon substrate. Beyond increased NP output, the publication reports a significant morphological evolution in the deposited thin films, attributed to the additional kinetic energy charged NPs acquire from the electric field. While these two effects cannot be obtained independently of each other, I conclude that the increased extraction of NPs from the NP source represents a meaningful step towards enhanced process efficiency for MS-IGC.

Within this thesis multiple pathways for successfully functionalizing substrates of various types such as powders, conventional two-dimensional substrates, as well as advanced nanoporous three-dimensional substrates, were highlighted. Challenges persist in uniformly functionalizing three-dimensional substrates, and the available technologies have to be well-suited for the specific task. As of now, the highly sophisticated magnetron sputter inert gas condensation is an excellent tool for performing fundamental research on high-purity NPs and the developed methodology allows for improved assessment of process stability and output. Yet, with current available systems, complex three-dimensional substrates cannot be successfully functionalized with a homogenous three-dimensional distribution. Conventional magnetron sputtering has shown promise, particularly with flexible carbon cloth substrates, hinting at the possibility of scaling up through roll-to-roll deposition techniques for broader application. The potential of plasma treatment methods remains largely untapped, presenting a fertile ground for future research and development towards innovative functionalization techniques.

6 Conclusions

This thesis underscores the critical role of synthesis methods in determining the range of substrates that can be effectively functionalized owing to limitations within the current techniques. Particularly MS-IGC is hindered by its inability to perform large-scale depositions along with poor process control and reproducibility, as well as its inappropriateness to penetrate complex materials like activated carbon cloth – a challenge highlighted by both the MS-IGC community's lack of gas sorption analysis investigations and unpublished findings by the group at Montanuniversität Leoben. Given these limitations, MS-IGC's application in functionalizing three-dimensional substrates appears constrained to very low functionalization depths and/or substrate thicknesses. The current state of MS-IGC suggests a strategic orientation towards utilizing this technology for fundamental NP formation research and the analysis of simple material systems on a lab scale, leaving wet chemistry methods as the predominant option for industrial-scale applications of functionalized nanomaterials. Nonetheless, the dielectric barrier discharge plasma treatment and the short-time magnetron sputtering process, as detailed in Publications I and II, demonstrate promising methods for functionalizing powders and woven materials through clean, wet-free vacuum processes, setting the stage for their potential scale-up and broader industrial adoption.

The journey of scientific discovery is both ongoing and never-ending. This thesis lays a foundation for future advancements, underscoring the importance of relentless pursuit and creativity in venturing into unexplored scientific territories where no one has gone before.

7 References

[1] K. Wieszczycka, K. Staszak, M.J. Woźniak-Budych, J. Litowczenko, B.M. Maciejewska, S. Jurga, Surface functionalization – The way for advanced applications of smart materials, Coord. Chem. Rev. 436 (2021) 213846. https://doi.org/10.1016/j.ccr.2021.213846.

[2] C. Liu, F. Li, L.-P. Ma, H.-M. Cheng, Advanced Materials for Energy Storage, Adv. Mater. 22 (2010) E28–E62. https://doi.org/10.1002/adma.200903328.

[3] K. Autumn, A.M. Peattie, Mechanisms of Adhesion in Geckos, Integr. Comp. Biol. 42 (2002) 1081–1090. https://doi.org/10.1093/icb/42.6.1081.

[4] Y. Zhang, X. Wan, X. Xu, P. Teng, S. Wang, Recent progress of tree frog toe pads inspired wet adhesive materials, Biosurface and Biotribology. 8 (2022) 279–289. https://doi.org/10.1049/bsb2.12049.

[5] M. Sato, Y. Ando, Topological superconductors: a review, Reports Prog. Phys. 80 (2017) 076501. https://doi.org/10.1088/1361-6633/aa6ac7.

[6] A. Chaves, J.G. Azadani, H. Alsalman, D.R. da Costa, R. Frisenda, A.J. Chaves, S.H. Song, Y.D. Kim, D. He, J. Zhou, A. Castellanos-Gomez, F.M. Peeters, Z. Liu, C.L. Hinkle, S.-H. Oh, P.D. Ye, S.J. Koester, Y.H. Lee, P. Avouris, X. Wang, T. Low, Bandgap engineering of two-dimensional semiconductor materials, Npj 2D Mater. Appl. 4 (2020) 29. https://doi.org/10.1038/s41699-020-00162-4.

[7] D.M. Mattox, Handbook of physical vapor deposition (PVD) processing, second ed., Elsevier, Amsterdam, 2010.

[8] E.H.L. Falcao, F. Wudl, Carbon allotropes: beyond graphite and diamond, J. Chem. Technol. Biotechnol. 82 (2007) 524–531. https://doi.org/10.1002/jctb.1693.

[9] Z. Heidarinejad, M.H. Dehghani, M. Heidari, G. Javedan, I. Ali, M. Sillanpää, Methods for preparation and activation of activated carbon: a review, Environ. Chem. Lett. 18 (2020) 393–415. https://doi.org/10.1007/s10311-019-00955-0.

[10] J. Jjagwe, P.W. Olupot, E. Menya, H.M. Kalibbala, Synthesis and Application of Granular Activated Carbon from Biomass Waste Materials for Water Treatment: A Review, J. Bioresour. Bioprod. 6 (2021) 292–322. https://doi.org/10.1016/j.jobab.2021.03.003.

[11] S.H. Tang, M.A. Ahmad Zaini, Development of activated carbon pellets using a facile low-cost binder for effective malachite green dye removal, J. Clean. Prod. 253 (2020) 119970. https://doi.org/10.1016/j.jclepro.2020.119970.

[12] N. Saeidi, M.N. Lotfollahi, A procedure to form powder activated carbon into activated carbon monolith, Int. J. Adv. Manuf. Technol. 81 (2015) 1281–1288. https://doi.org/10.1007/s00170-015-7311-z.

[13] R. Llamas-Unzueta, M.A. Montes-Morán, L.A. Ramírez-Montoya, A. Concheso, J.A. Menéndez, Whey as a sustainable binder for the production of extruded activated carbon, J. Environ. Chem. Eng. 10 (2022) 107590. https://doi.org/10.1016/j.jece.2022.107590.

[14] N. Kostoglou, A. Tarat, I. Walters, V. Ryzhkov, C. Tampaxis, G. Charalambopoulou, T. Steriotis, C. Mitterer, C. Rebholz, Few-layer graphene-like flakes derived by plasma treatment: A potential material for hydrogen adsorption and storage, Microporous Mesoporous Mater. 225 (2016) 482–487.

https://doi.org/10.1016/j.micromeso.2016.01.027.

[15] R.M. Nielsen, S. Murphy, C. Strebel, M. Johansson, I. Chorkendorff, J.H. Nielsen, The morphology of mass selected ruthenium nanoparticles from a magnetron-sputter gas-aggregation source, J. Nanoparticle Res. 12 (2010) 1249–1262. https://doi.org/10.1007/s11051-009-9830-8.

[16] G.E. Johnson, R. Colby, J. Laskin, Soft landing of bare nanoparticles with controlled size, composition, and morphology, Nanoscale. 7 (2015) 3491–3503. https://doi.org/10.1039/c4nr06758d.

[17] I. Musa, N. Qamhieh, S.T. Mahmoud, Ag Nanocluster Production through DC Magnetron Sputtering and Inert Gas Condensation: A Study of Structural, Kelvin Probe Force Microscopy, and Optical Properties, Nanomaterials. 13 (2023) 2758. https://doi.org/10.3390/nano13202758.

[18] O. Kylián, J. Kratochvíl, J. Hanuš, O. Polonskyi, P. Solař, H. Biederman, Fabrication of Cu nanoclusters and their use for production of Cu/plasma polymer nanocomposite thin films, Thin Solid Films. 550 (2014) 46–52. https://doi.org/10.1016/j.tsf.2013.10.029.

[19] S.J. Carroll, S.G. Hall, R.E. Palmer, R. Smith, Energetic Impact of Size-Selected Metal Cluster Ions on Graphite, Phys. Rev. Lett. 81 (1998) 3715–3718. https://doi.org/10.1103/PhysRevLett.81.3715.

[20] M. Vaidulych, A. Shelemin, J. Hanuš, I. Khalakhan, I. Krakovsky, P. Kočová, H. Mašková, J. Kratochvíl, P. Pleskunov, J. Štěrba, O. Kylián, A. Choukourov, H. Biederman, Superwettable antibacterial textiles for versatile oil/water separation, Plasma Process. Polym. 16 (2019) 1900003. https://doi.org/10.1002/ppap.201900003.

[21] K.S. Novoselov, A.K. Geim, S. V Morozov, D. Jiang, Y. Zhang, S. V Dubonos, I. V Grigorieva, A.A. Firsov, Electric Field Effect in Atomically Thin Carbon Films, Science (80-.). 306 (2004) 666–669. https://doi.org/10.1126/science.1102896.

[22] M.J. McAllister, J.-L. Li, D.H. Adamson, H.C. Schniepp, A.A. Abdala, J. Liu, M. Herrera-Alonso, D.L. Milius, R. Car, R.K. Prud'homme, I.A. Aksay, Single Sheet Functionalized Graphene by Oxidation and Thermal Expansion of Graphite, Chem. Mater. 19 (2007) 4396–4404. https://doi.org/10.1021/cm0630800.

[23] S. Deng, V. Berry, Wrinkled, rippled and crumpled graphene: an overview of formation mechanism, electronic properties, and applications, Mater. Today. 19 (2016) 197–212. https://doi.org/10.1016/j.mattod.2015.10.002.

[24] S. Brunauer, P.H. Emmett, E. Teller, Adsorption of Gases in Multimolecular Layers, J. Am. Chem. Soc. 60 (1938) 309–319. https://doi.org/10.1021/ja01269a023.

[25] M. Thommes, K. Kaneko, A. V Neimark, J.P. Olivier, F. Rodriguez-Reinoso, J. Rouquerol, K.S.W. Sing, Physisorption of gases, with special reference to the evaluation of surface area and pore size distribution (IUPAC Technical Report), Pure Appl. Chem. 87 (2015) 1051–1069. https://doi.org/10.1515/pac-2014-1117.

[26] X.-Y. Yang, L.-H. Chen, Y. Li, J.C. Rooke, C. Sanchez, B.-L. Su, Hierarchically porous materials: synthesis strategies and structure design, Chem. Soc. Rev. 46 (2017) 481–558. https://doi.org/10.1039/C6CS00829A.

[27] S. Zhang, S. Xiao, D. Li, J. Liao, F. Ji, H. Liu, L. Ci, Commercial carbon cloth: An emerging substrate for practical lithium metal batteries, Energy Storage Mater. 48 (2022) 172–190.

https://doi.org/10.1016/j.ensm.2022.03.014.

[28] H. Shi, G. Wen, Y. Nie, G. Zhang, H. Duan, Flexible 3D carbon cloth as a high-performing electrode for energy storage and conversion, Nanoscale. 12 (2020) 5261–5285. https://doi.org/10.1039/C9NR09785F.

[29] N. Kostoglou, C. Koczwara, C. Prehal, V. Terziyska, B. Babic, B. Matovic, G. Constantinides, C. Tampaxis, G. Charalambopoulou, T. Steriotis, S. Hinder, M. Baker, K. Polychronopoulou, C. Doumanidis, O. Paris, C. Mitterer, C. Rebholz, Nanoporous activated carbon cloth as a versatile material for hydrogen adsorption, selective gas separation and electrochemical energy storage, Nano Energy. 40 (2017) 49–64. https://doi.org/10.1016/j.nanoen.2017.07.056.

[30] T. V. Pfeiffer, J. Feng, A. Schmidt-Ott, New developments in spark production of nanoparticles, Adv. Powder Technol. 25 (2014) 56–70. https://doi.org/10.1016/j.apt.2013.12.005.

[31] A. Tamm, A. Tarre, V. Verchenko, H. Seemen, R. Stern, Atomic Layer Deposition of Superconducting CuO Thin Films on Three-Dimensional Substrates, Crystals. 10 (2020) 650. https://doi.org/10.3390/cryst10080650.

[32] M. Adachi, S. Tsukui, K. Okuyama, Nanoparticle Synthesis by Ionizing Source Gas in Chemical Vapor Deposition, Jpn. J. Appl. Phys. 42 (2003) L77–L79. https://doi.org/10.1143/JJAP.42.L77.

[33] M. Parashar, V.K. Shukla, R. Singh, Metal oxides nanoparticles via sol–gel method: a review on synthesis, characterization and applications, J. Mater. Sci. Mater. Electron. 31 (2020) 3729–3749. https://doi.org/10.1007/s10854-020-02994-8.

[34] U.S. Mohanty, Electrodeposition: a versatile and inexpensive tool for the synthesis of nanoparticles, nanorods, nanowires, and nanoclusters of metals, J. Appl. Electrochem. 41 (2011) 257–270. https://doi.org/10.1007/s10800-010-0234-3.

[35] M. Salavati-Niasari, F. Davar, N. Mir, Synthesis and characterization of metallic copper nanoparticles via thermal decomposition, Polyhedron. 27 (2008) 3514–3518. https://doi.org/10.1016/j.poly.2008.08.020.

[36] D.M. Mattox, Physical vapor deposition (PVD) processes, Met. Finish. 100 (2002) 394–408. https://doi.org/10.1016/S0026-0576(02)82043-8.

[37] T. Suni, K. Henttinen, I. Suni, J. Mäkinen, Effects of Plasma Activation on Hydrophilic Bonding of Si and SiO2, J. Electrochem. Soc. 149 (2002) G348–G351. https://doi.org/10.1149/1.1477209.

[38] E.M. Liston, L. Martinu, M.R. Wertheimer, Plasma surface modification of polymers for improved adhesion: a critical review, J. Adhes. Sci. Technol. 7 (1993) 1091–1127. https://doi.org/10.1163/156856193X00600.

[39] M. Rybin, A. Pereyaslavtsev, T. Vasilieva, V. Myasnikov, I. Sokolov, A. Pavlova, E. Obraztsova, A. Khomich, V. Ralchenko, E. Obraztsova, Efficient nitrogen doping of graphene by plasma treatment, Carbon. 96 (2016) 196–202. https://doi.org/10.1016/j.carbon.2015.09.056.

[40] V.M. Donnelly, A. Kornblit, Plasma etching: Yesterday, today, and tomorrow, J. Vac. Sci. Technol. A Vacuum, Surfaces, Film. 31 (2013) 050825. https://doi.org/10.1116/1.4819316.

[41] D.F. O'Kane, K.L. Mittal, Plasma cleaning of metal surfaces, J. Vac. Sci. Technol. 11 (1974) 567–569. https://doi.org/10.1116/1.1318069.

[42] W. Siemens, Ueber die elektrostatische Induction und die Verzögerung des Stroms in Flaschendrähten,

Ann. Phys. 178 (1857) 66–122. https://doi.org/10.1002/andp.18571780905.

[43] J. Li, C. Ma, S. Zhu, F. Yu, B. Dai, D. Yang, A Review of Recent Advances of Dielectric Barrier Discharge Plasma in Catalysis, Nanomaterials. 9 (2019) 1428. https://doi.org/10.3390/nano9101428.

[44] U. Kogelschatz, Dielectric-Barrier Discharges: Their History, Discharge Physics, and Industrial Applications, Plasma Chem. Plasma Process. 23 (2003) 1–46. https://doi.org/10.1023/A:1022470901385.

[45] G. Greczynski, L. Hultman, X-ray photoelectron spectroscopy: Towards reliable binding energy referencing, Prog. Mater. Sci. 107 (2020) 100591. https://doi.org/10.1016/j.pmatsci.2019.100591.

[46] G. Greczynski, L. Hultman, Impact of sample storage type on adventitious carbon and native oxide growth: X-ray photoelectron spectroscopy study, Vacuum. 205 (2022) 111463. https://doi.org/10.1016/j.vacuum.2022.111463.

[47] D. Lundin, T. Minea, J.T. Gudmundsson, T. Minea, High power impulse magnetron sputtering: Fundamentals, technologies, challenges and applications, first ed., Elsevier, Amsterdam, 2019. https://doi.org/10.1016/C2016-0-02463-4.

[48] M. Ohring, Materials science of thin films: deposition and structure, second ed., Academic Press, San Diego, 2002.

[49] F. Paschen, Ueber die zum Funkenübergang in Luft, Wasserstoff und Kohlensäure bei verschiedenen Drucken erforderliche Potentialdifferenz, Ann. Phys. 273 (1889) 69–96. https://doi.org/10.1002/andp.18892730505.

[50] F.M. Penning, Die Glimmentladung bei niedrigem Druck zwischen koaxialen Zylindern in einem axialen Magnetfeld, Physica. 3 (1936) 873–894. https://doi.org/10.1016/S0031-8914(36)80313-9.

[51] Y. Huttel, Gas-phase synthesis of nanoparticles, first ed., John Wiley & Sons, Weinheim, 2017.

[52] I. Petrov, A. Myers, J.E. Greene, J.R. Abelson, Mass and energy resolved detection of ions and neutral sputtered species incident at the substrate during reactive magnetron sputtering of Ti in mixed Ar+N2 mixtures, J. Vac. Sci. Technol. A. 12 (1994) 2846–2854. https://doi.org/10.1116/1.578955.

[53] J.T. Gudmundsson, Physics and technology of magnetron sputtering discharges, Plasma Sources Sci. Technol. 29 (2020) 113001. https://doi.org/10.1088/1361-6595/abb7bd.

[54] F. Frank, ZrN-based hard coatings deposited by chemical and physical vapor deposition, Montanuniversität Leoben, 2022.

[55] P.B. Barna, M. Adamik, Fundamental structure forming phenomena of polycrystalline films and the structure zone models, Thin Solid Films. 317 (1998) 27–33. https://doi.org/10.1016/S0040-6090(97)00503-8.

[56] I. Petrov, P.B. Barna, L. Hultman, J.E. Greene, Microstructural evolution during film growth, J. Vac. Sci. Technol. A. 21 (2003) S117–S128. https://doi.org/10.1116/1.1601610.

[57] H. Haberland, M. Karrais, M. Mall, A new type of cluster and cluster ion source, Zeitschrift Für Phys. D Atoms, Mol. Clust. 20 (1991) 413–415. https://doi.org/10.1007/BF01544025.

[58] F. Knabl, C. Bandl, T. Griesser, C. Mitterer, In situ and ex situ quantification of nanoparticle fluxes in magnetron sputter inert gas condensation: A Cu nanoparticle case study, J. Vac. Sci. Technol. A. 42 (2024) 023201. https://doi.org/10.1116/6.0003283.

[59] D. Nikitin, J. Hanuš, S. Ali-Ogly, O. Polonskyi, J. Drewes, F. Faupel, H. Biederman, A. Choukourov, The evolution of Ag nanoparticles inside a gas aggregation cluster source, Plasma Process. Polym. 16 (2019) 1900079. https://doi.org/10.1002/ppap.201900079.

[60] B.M. Smirnov, I. Shyjumon, R. Hippler, Flow of nanosize cluster-containing plasma in a magnetron discharge, Phys. Rev. E. 75 (2007) 66402. https://doi.org/10.1103/PhysRevE.75.066402.

[61] A. Shelemin, P. Pleskunov, J. Kousal, J. Drewes, J. Hanuš, S. Ali-Ogly, D. Nikitin, P. Solař, J. Kratochvíl, M. Vaidulych, M. Schwartzkopf, O. Kylián, O. Polonskyi, T. Strunskus, F. Faupel, S. V. Roth, H. Biederman, A. Choukourov, Nucleation and Growth of Magnetron-Sputtered Ag Nanoparticles as Witnessed by Time-Resolved Small Angle X-Ray Scattering, Part. Part. Syst. Charact. 37 (2020) 1900436. https://doi.org/10.1002/ppsc.201900436.

[62] Batková, T. Kozák, S. Haviar, P. Mareš, J. Čapek, Effect of exit-orifice diameter on Cu nanoparticles produced by gas-aggregation source, Surf. Coat. Technol. 417 (2021) 127196. https://doi.org/10.1016/j.surfcoat.2021.127196.

[63] M. Khojasteh, V. V. Kresin, Influence of source parameters on the growth of metal nanoparticles by sputter-gas-aggregation, Appl. Nanosci. 7 (2017) 875–883. https://doi.org/10.1007/s13204-017-0627-2.

[64] P. Solař, J. Kousal, J. Hanuš, K. Škorvánková, A. Kuzminova, O. Kylián, Mechanical time-of-flight filter based on slotted disks and helical rotor for measurement of velocities of nanoparticles, Sci. Rep. 11 (2021) 6415. https://doi.org/10.1038/s41598-021-85533-7.

[65] M. Ganeva, A. V. Pipa, R. Hippler, The influence of target erosion on the mass spectra of clusters formed in the planar DC magnetron sputtering source, Surf. Coat. Technol. 213 (2012) 41–47. https://doi.org/10.1016/j.surfcoat.2012.10.012.

[66] S. Pratontep, S.J. Carroll, C. Xirouchaki, M. Streun, R.E. Palmer, Size-selected cluster beam source based on radio frequency magnetron plasma sputtering and gas condensation, Rev. Sci. Instrum. 76 (2005) 45103. https://doi.org/10.1063/1.1869332.

[67] A. Marek, J. Valter, S. Kadlec, J. Vyskočil, Gas aggregation nanocluster source — Reactive sputter deposition of copper and titanium nanoclusters, Surf. Coat. Technol. 205 (2011) S573–S576. https://doi.org/10.1016/j.surfcoat.2010.12.027.

[68] O. Polonskyi, O. Kylián, M. Drábik, J. Kousal, P. Solař, A. Artemenko, J. Čechvala, A. Choukourov, D. Slavínská, H. Biederman, Deposition of Al nanoparticles and their nanocomposites using a gas aggregation cluster source, J. Mater. Sci. 49 (2014) 3352–3360. https://doi.org/10.1007/s10853-014-8042-5.

[69] A. Banerjee, B. Das, An ultrahigh vacuum complementary metal oxide silicon compatible nonlithographic system to fabricate nanoparticle-based devices, Rev. Sci. Instrum. 79 (2008) 033910. https://doi.org/10.1063/1.2885042.

[70] E. Pérez-Tijerina, M.G. Pinilla, S. Mejía-Rosales, U. Ortiz-Méndez, A. Torres, M. José-Yacamán, Highly size-controlled synthesis of Au/Pd nanoparticles by inert-gas condensation, Faraday Discuss. 138 (2008) 353–362. https://doi.org/10.1039/b705913m.

[71] A. Shelemin, Z. Krtous, B. Baloukas, O. Zabeida, J. Klemberg-Sapieha, L. Martinu, Fabrication of Plasmonic

Indium Tin Oxide Nanoparticles by Means of a Gas Aggregation Cluster Source, ACS Omega. 8 (2023) 6052–6058. https://doi.org/10.1021/acsomega.2c08070.

[72] G.E. Johnson, R. Colby, M. Engelhard, D. Moon, J. Laskin, Soft landing of bare PtRu nanoparticles for electrochemical reduction of oxygen, Nanoscale. 7 (2015) 12379. https://doi.org/10.1039/c5nr03154k.

[73] Q. Yang, M. Danaie, N. Young, V. Broadley, D.E. Joyce, T.L. Martin, E. Marceau, M.P. Moody, P.A.J. Bagot, Atom Probe Tomography of Au-Cu Bimetallic Nanoparticles Synthesized by Inert Gas Condensation, J. Phys. Chem. C. 123 (2019) 26481–26489. https://doi.org/10.1021/acs.jpcc.9b09340.

[74] J.-G. Mattei, P. Grammatikopoulos, J. Zhao, V. Singh, J. Vernieres, S. Steinhauer, A. Porkovich, E. Danielson, K. Nordlund, F. Djurabekova, M. Sowwan, Gas-Phase Synthesis of Trimetallic Nanoparticles, Chem. Mater. 31 (2019) 2151–2163. https://doi.org/10.1021/acs.chemmater.9b00129.

[75] T. Kretková, J. Hanuš, O. Kylián, P. Solař, M. Dopita, M. Cieslar, I. Khalakhan, A. Choukourov, H. Biederman, In-flight modification of Ni nanoparticles by tubular magnetron sputtering, J. Phys. D. Appl. Phys. 51 (2019) 205302. https://doi.org/10.1088/1361-6463/ab00d0.

[76] O. Polonskyi, P. Solař, O. Kylián, M. Drábik, A. Artemenko, J. Kousal, J. Hanuš, J. Pešička, I. Matolínová, E. Kolíbalová, D. Slavínská, H. Biederman, Nanocomposite metal/plasma polymer films prepared by means of gas aggregation cluster source, Thin Solid Films. 520 (2012) 4155–4162. https://doi.org/10.1016/j.tsf.2011.04.100.

[77] V.N. Popok, L. Gurevich, Charge states of size-selected silver nanoparticles produced by magnetron sputtering, J. Nanoparticle Res. 21 (2019) 171. https://doi.org/10.1007/s11051-019-4615-1.

[78] F. Zamboni, A. Makarevičiūtė, V.N. Popok, Long-Term Plasmonic Stability of Copper Nanoparticles Produced by Gas-Phase Aggregation Method Followed by UV-Ozone Treatment, Appl. Nano. 3 (2022) 102–111. https://doi.org/10.3390/applnano3020007.

[79] H. Haberland, M. Moseler, Y. Qiang, O. Rattunde, T. Reiners, Y. Thurner, Energetic cluster impact (ECI): A new method for thin-film formation, Surf. Rev. Lett. 3 (1996) 887–890.

[80] O. Rattunde, M. Moseler, A. Häfele, J. Kraft, D. Rieser, H. Haberland, Surface smoothing by energetic cluster impact, J. Appl. Phys. 90 (2001) 3226–3231. https://doi.org/10.1063/1.1398067.

[81] I. Michelakaki, N. Boukos, D.A. Dragatogiannis, S. Stathopoulos, C.A. Charitidis, D. Tsoukalas, Synthesis of hafnium nanoparticles and hafnium nanoparticle films by gas condensation and energetic deposition, Beilstein J. Nanotechnol. 9 (2018) 1868–1880. https://doi.org/10.3762/bjnano.9.179.

[82] I. Shyjumon, M. Gopinadhan, O. Ivanova, M. Quaas, H. Wulff, C.A. Helm, R. Hippler, Structural deformation, melting point and lattice parameter studies of size selected silver clusters, Eur. Phys. J. D. 37 (2006) 409–415. https://doi.org/10.1140/epjd/e2005-00319-x.

[83] V.N. Popok, I. Barke, E.E.B. Campbell, K.H. Meiwes-Broer, Cluster–surface interaction: From soft landing to implantation, Surf. Sci. Rep. 66 (2011) 347–377. https://doi.org/10.1016/j.surfrep.2011.05.002.

[84] A. Kusior, K. Kollbek, K. Kowalski, M. Borysiewicz, T. Wojciechowski, A. Adamczyk, A. Trenczek-Zajac, M. Radecka, K. Zakrzewska, Sn and Cu oxide nanoparticles deposited on TiO2 nanoflower 3D substrates by Inert Gas Condensation technique, Appl. Surf. Sci. 380 (2016) 193–202. https://doi.org/10.1016/j.apsusc.2016.01.204.

[85] M. Gracia-Pinilla, E. Martínez, G.S. Vidaurri, E. Pérez-Tijerina, Deposition of Size-Selected Cu Nanoparticles by Inert Gas Condensation, Nanoscale Res. Lett. 5 (2009) 180–188. https://doi.org/10.1007/s11671-009-9462-z.

[86] W. Chamorro-Coral, A. Caillard, P. Brault, P. Andreazza, C. Coutanceau, S. Baranton, The role of oxygen on the growth of palladium clusters synthesized by gas aggregation source, Plasma Process. Polym. 16 (2019) e1900006. https://doi.org/10.1002/ppap.201900006.

[87] H. Haberland, M. Karrais, M. Mall, Y. Thurner, Thin films from energetic cluster impact: A feasibility study, J. Vac. Sci. Technol. A. 10 (1992) 3266–3271. https://doi.org/10.1116/1.577853.

[88] S.R. Plant, L. Cao, R.E. Palmer, Atomic Structure Control of Size-Selected Gold Nanoclusters during Formation, J. Am. Chem. Soc. 136 (2014) 7559–7562. https://doi.org/10.1021/ja502769v.

[89] B.M. Smirnov, Nanoclusters and microparticles in gases and vapors, first ed., Walter de Gruyter, Berlin, 2012.

[90] P. Curda, R. Hippler, M. Cada, O. Kylián, V. Stranak, Z. Hubicka, The role of dimers in the efficient growth of nanoparticles, Surf. Coat. Technol. 473 (2023) 130045. https://doi.org/10.1016/j.surfcoat.2023.130045.

[91] M. Grössl, M. Langenwalter, H. Helm, T.D. Märk, Molecular ion formation in decaying plasmas produced in pure argon and krypton, J. Chem. Phys. 74 (1981) 1728–1735. https://doi.org/10.1063/1.441261.

[92] G. Krishnan, S. de Graaf, G.H. ten Brink, P.O.Å. Persson, B.J. Kooi, G. Palasantzas, Strategies to initiate and control the nucleation behavior of bimetallic nanoparticles, Nanoscale. 9 (2017) 8149–8156. https://doi.org/10.1039/C7NR00916J.

[93] J.I. Goldstein, D.E. Newbury, J.R. Michael, N.W.M. Ritchie, J.H.J. Scott, D.C. Joy, Scanning electron microscopy and X-ray microanalysis, fourth ed., Springer, New York, 2017.

[94] F. Knabl, N. Kostoglou, V. Terziyska, S. Hinder, M. Baker, E. Bousser, C. Rebholz, C. Mitterer, Short-Time Magnetron Sputtering for the Development of Carbon–Palladium Nanocomposites, Nanomaterials. 14 (2024) 164. https://doi.org/10.3390/nano14020164.

[95] A. Einstein, Über einen die Erzeugung und Verwandlung des Lichtes betreffenden heuristischen Gesichtspunkt, Ann. Phys. 322 (1905) 132–148. https://doi.org/10.1002/andp.19053220607.

[96] Wikimedia Commons, X-Ray Photoelectron Spectroscopy, (2010). https://commons.wikimedia.org/wiki/File:XPS_PHYSICS.png (accessed April 7, 2014).

[97] J. Chastain, R.C. King Jr, Handbook of X-ray photoelectron spectroscopy, first ed., Perkin-Elmer, Eden Prairie, USA, 1992.

[98] S. Hofmann, Auger-and X-ray Photoelectron Spectroscopy in Materials Science, First ed., Springer, Berlin, 2012.

[99] W. Paul, H. Steinwedel, Ein neues Massenspektrometer ohne Magnetfeld, Zeitschrift Für Naturforsch. A. 8 (1953) 448–450. https://doi.org/10.1515/zna-1953-0710.

[100] W. Paul, M. Raether, Das elektrische Massenfilter, Zeitschrift Für Phys. 140 (1955) 262–273. https://doi.org/10.1007/BF01328923.

[101] W. Paul, H.P. Reinhard, U. von Zahn, Das elektrische Massenfilter als Massenspektrometer und

Isotopentrenner, Zeitschrift Für Phys. 152 (1958) 143–182. https://doi.org/10.1007/BF01327353.

[102] P. Labastie, M. Doy, A high mass range quadrupole spectrometer for cluster studies, Int. J. Mass Spectrom. Ion Process. 91 (1989) 105–112. https://doi.org/10.1016/0168-1176(89)83001-0.

[103] P.H. Dawson, Quadrupole mass spectrometry and its applications, first ed., Elsevier, Amsterdam, 1976.

[104] J. Benedikt, A. Hecimovic, D. Ellerweg, A. Von Keudell, Quadrupole mass spectrometry of reactive plasmas, J. Phys. D. Appl. Phys. 45 (2012) 403001. https://doi.org/10.1088/0022-3727/45/40/403001.

[105] N. V Konenkov, M. Sudakov, D.J. Douglas, Matrix methods for the calculation of stability diagrams in quadrupole mass spectrometry, J. Am. Soc. Mass Spectrom. 13 (2002) 597–613. https://doi.org/10.1016/S1044-0305(02)00365-3.

[106] College Union, Accelerated Surface Area and Porosimetry System, (n.d.). https://muse.union.edu/aerogels/aerogel-lab-at-union/accelerated-surface-area-and-porosimetry-system/ (accessed March 19, 2024).

[107] J. Rouquerol, F. Rouquerol, P. Llewellyn, G. Maurin, K. Sing, Adsorption by powders and porous solids: principles, methodology and applications, second ed., Elsevier, Amsterdam, 2014.

[108] P.A. Monson, Understanding adsorption/desorption hysteresis for fluids in mesoporous materials using simple molecular models and classical density functional theory, Microporous Mesoporous Mater. 160 (2012) 47–66. https://doi.org/10.1016/j.micromeso.2012.04.043.

[109] F. Knabl, N. Kostoglou, R.K. Gupta, A. Tarat, S. Hinder, M. Baker, C. Rebholz, C. Mitterer, Plasma-Treated Cobalt-Doped Nanoporous Graphene for Advanced Electrochemical Applications, C. 10 (2024) 31. https://doi.org/10.3390/c10020031.

[110] G. Bräuer, B. Szyszka, M. Vergöhl, R. Bandorf, Magnetron sputtering – Milestones of 30 years, Vacuum. 84 (2010) 1354–1359. https://doi.org/10.1016/j.vacuum.2009.12.014.

[111] R. Ludwig, R. Kukla, E. Josephson, Vacuum Web Coating - State of the Art and Potential for Electronics, Proc. IEEE. 93 (2005) 1483–1490. https://doi.org/10.1109/JPROC.2005.851489.

8 Publications

8.1 List of Included Publications

I. **Plasma-Treated Cobalt-Doped Nanoporous Graphene for Advanced Electrochemical Applications**
Florian Knabl, Nikolaos Kostoglou, Ram K. Gupta, Afshin Tarat, Steven Hinder, Mark Baker, Claus Rebholz, Christian Mitterer
C, 10(2) (2024) 31

II. **Short-Time Magnetron Sputtering for the Development of Carbon–Palladium Nanocomposites**
Florian Knabl, Nikolaos Kostoglou, Velislava Terziyska, Steven Hinder, Mark Baker, Etienne Bousser, Claus Rebholz, Christian Mitterer
Nanomaterials, 14 (2024) 164

III. ***In Situ*** **and** ***Ex Situ*** **Quantification of Nanoparticle Fluxes in Magnetron Sputter Inert Gas Condensation: A Cu Nanoparticle Case Study**
Florian Knabl, Christine Bandl, Thomas Griesser, Christian Mitterer
Journal of Vacuum Science and Technology A, 42(2) (2024) 023201

IV. **Enhancement of Copper Nanoparticle Yield in Magnetron Sputter Inert Gas Condensation by Applying Substrate Bias Voltage and its Influence on Thin Film Morphology**
Florian Knabl, Dominik Gutnik, Prathamesh Patil, Christine Bandl, Tijmen Vermeij, Christian M. Pichler, Barbara Putz, Christian Mitterer
Submitted for publication

8.2 My Contribution to the Included Publications

	Conception and planning[1]	Experiments	Analysis and interpretation	Manuscript preparation[1]
Publication I	20 %	0 %	70 %	100 %
Publication II	20 %	0 %	70 %	80 %
Publication III	100 %	80 %	100 %	100 %
Publication IV	80 %	50 %	70 %	80 %

[1] Supervision not included

8.3 Publication I

Plasma-Treated Cobalt-Doped Nanoporous Graphene for Advanced Electrochemical Applications

Florian Knabl, Nikolaos Kostoglou, Ram K. Gupta, Afshin Tarat, Steven Hinder, Mark Baker, Claus Rebholz, Christian Mitterer

C, 10(2) (2024) 31

Plasma-Treated Cobalt-Doped Nanoporous Graphene for Advanced Electrochemical Applications

Florian Knabl[1], Nikolaos Kostoglou[1], Ram K. Gupta[2], Afshin Tarat[3], Steven Hinder[4], Mark Baker[4], Claus Rebholz[1,5], Christian Mitterer[1]

[1] Department of Materials Science, Montanuniversität Leoben, 8700 Leoben, Austria

[2] Department of Chemistry, Pittsburg State University, Pittsburg, KS 66762, USA

[3] Loginns GmbH, 9020 Klagenfurt, Austria

[4] Department of Mechanical Engineering Sciences, University of Surrey, Guildford GU2 7XH, UK

[5] Department of Mechanical and Manufacturing Engineering, University of Cyprus, Nicosia 1678, Cyprus

Keywords: graphene; plasma; cobalt; nanocomposites; nanoporous powders; water splitting; oxygen evolution reaction; supercapacitor;

Abstract

Metal–carbon nanocomposites are identified as key contenders for enhancing water splitting through the oxygen evolution reaction and boosting supercapacitor energy storage capacitances. This study utilizes plasma treatment to transform natural graphite into nanoporous few-layer graphene, followed by additional milling and plasma steps to synthesize a cobalt–graphene nanocomposite. Comprehensive structural characterization was conducted using scanning and transmission electron microscopy, X-ray diffraction, Raman spectroscopy, gas sorption analysis and X-ray photoelectron spectroscopy. Electrochemical evaluations further assessed the materials' oxygen evolution reaction and supercapacitor performance. Although the specific surface area of the nanoporous carbon decreases from 780 to 480 m2/g in the transition to the resulting nanocomposite, it maintains its nanoporous structure and delivers a competitive electrochemical performance, as evidenced by an overpotential of 290 mV and a Tafel slope of 110 mV/dec. This demonstrates the efficacy of plasma treatment in the surface functionalization of carbon-based materials, highlighting its potential for large-scale chemical-free application due to its environmental friendliness and scalability, paving the way toward future applications.

1. Introduction

The ever-increasing global demand for energy, coupled with the climate crisis from emissions of carbon dioxide and other greenhouse gases, underscores the urgent need for solutions to ensure a more sustainable future. Significant efforts are underway to develop materials that facilitate efficient and environmentally friendly energy conversion and storage. Hydrogen, as a clean energy carrier synthesized ideally through water electrolysis, holds promise for a sustainable future. Electrolytic water splitting, encompassing both the hydrogen evolution reaction (HER) and the oxygen evolution reaction (OER) [1], requires an effective catalyst to enhance kinetics and cost-effectiveness. Meanwhile, supercapacitors are considered to be another important cornerstone of advanced clean energy technologies. They offer substantial power densities for energy storage and rapid charging and discharging, utilizing the formation of electric double layers and electrochemical pseudocapacitance [2].

Carbon-based nanoporous materials are prime candidates for both OER [3] and supercapacitor applications [4,5] due to their superior properties, such as high chemical and mechanical stability, excellent electrical conductivity and expansive specific surface areas with adjustable pore size distributions. Enhancing these intrinsic properties through surface functionalization is a key area of current research [6], offering the potential for even more optimized performance in energy-related applications. Cobalt nanoparticles [7] and cobalt oxides [8] have been used for the OER in previous studies, with multiple reports on bimetallic and mixed oxide systems containing cobalt listed in [9]. Multiple studies investigated cobalt-based materials for supercapacitor applications [10].

Nanocomposites that integrate carbon with cobalt present an attractive approach toward harnessing the beneficial properties of both constituents and potentially achieving synergistic effects. Multiple cobalt-doped graphitic materials were investigated with respect to their OER performance, including cobalt-embedded nitrogen-doped carbon nanotubes [11,12], as well as composites containing porous carbons [13,14]. Supercapacitor applications of cobalt oxide with graphene nanosheets were presented by Naveen et al. [15] and Lakra et al. [16]. Furthermore, Liu et al. [17] designed a composite using mesoporous carbon nanospheres decorated with cobalt-based nanoparticles that showed enhanced supercapacitor performance, demonstrating ongoing research in those topics.

The graphene-based materials discussed in the literature are synthesized using a variety of methods, such as the mechanical exfoliation of graphite [18], the reduction of graphene oxide [19] and chemical-vapor-deposition-based synthesis [20], among others [21,22]. However, purely physical techniques like plasma-assisted exfoliation of natural graphite are rarely employed. Our previous work pioneered this approach, transforming

natural graphite into nanoporous few-layer graphene (FLG) with a markedly high specific surface area that was used for hydrogen storage [23], followed by a study on water purification and supercapacitor performance [24]. Hence, this method not only highlights the potential for a more efficient synthesis process but also suggests improved performance characteristics for energy-related applications.

In this work, we introduce an innovative approach by implementing an additional plasma processing step after mixing FLG with cobalt powder, yielding cobalt-enriched few-layer graphene (Co-FLG). This composite is compared to its pure FLG counterpart through a series of structural and electrochemical characterization methods, including scanning electron microscopy (SEM), energy-dispersive X-ray spectroscopy (EDX), transmission electron microscopy (TEM), X-ray diffraction (XRD), Raman spectroscopy, gas sorption analysis (GSA) and X-ray photoelectron spectroscopy (XPS). The electrochemical analyses specifically assess the oxygen evolution reaction and supercapacitor performances. This study marks the first demonstration that a purely physical method can effectively create carbon–cobalt composite materials exhibiting enhanced electrochemical performance compared to the pure nanoporous graphene. The method stands out for its dry/chemical-free, cost-efficient and environmentally friendly character, presenting a scalable solution for industry. The findings of this study not only advance the understanding of metal–carbon composites but also open new avenues for the development of green energy technologies based on these novel materials.

2. Materials and Methods

2.1. Material Synthesis

The FLG material was synthesized by subjecting natural flake graphite (Asbury Carbons, Ashbury, NJ) to plasma treatment using a multi-electrode dielectric barrier discharge plasma reactor, operating under the conditions outlined in [23]. The graphite was subjected to an argon flow of 600 sccm (corresponding to a pressure of 0.1 mbar) with a power of 6 kW for 60 min. Following this, the resultant FLG powder underwent a further 30 min oxygen plasma treatment to add oxygen-containing functional groups aimed at decreasing particle agglomeration.

A total of 100 g of the FLG material was then mixed with 5 g of cobalt powder (Thermo Scientific Chemicals, Waltham, MA, USA) of 99.8% purity and a 1.6 µm average particle size, using mechanical stirring for 5 min to ensure uniformity. This mixture was then subjected to an additional argon plasma treatment step for 60 min within the same reactor using the same gas flow and power values as above. These specific conditions/process parameters were determined in preliminary studies and were chosen to promote the uniform distribution of

cobalt particles within the FLG matrix and to optimize the composite's physical and electrochemical characteristics.

2.2. Structural and Morphological Characterization

The SEM micrographs were collected by an FEI Quanta 200 microscope (Hillsboro, OR, USA) using a 20 kV acceleration voltage and a working distance of 10 mm. EDX elemental maps were collected with an EDVAC Genesis X-ray analysis probe mounted on the SEM instrument using the same 20 kV acceleration voltage.

The TEM micrographs were recorded by employing a Philips CM-20 (Eindhoven, Netherlands) transmission electron microscope with high-resolution capabilities equipped with a LaB_6 filament and operated at 200 kV acceleration voltage. The powders were first ultra-sonicated in ethanol and then placed onto holey carbon-only support films mounted on copper grids.

The XRD investigations were performed on a Bruker-AXS D8 Advance diffractometer (Karlsruhe, Germany) in a Bragg–Brentano configuration. The diffractograms were recorded using Cu Kα radiation with a wavelength of ~0.154 nm operating with a voltage of 40 kV and a current of 40 mA. The scans were recorded from diffraction angles of 15°–60° in a continuous scan mode with a step size of 0.02° and a time of 1.2 s per step. Bragg's law was used to calculate the interplanar spacing d between the individual graphene layers from the (002) reflection. Scherrer's equation was used to calculate the crystallite size L_c from the (002) reflection [25]. The number of graphene layers n was estimated by dividing the L_c value by the d value ($n = L_c/d$).

Micro-Raman spectroscopy was conducted utilizing an inVia Reflex spectrometer (Renishaw, Wotton-under-Edge, UK), equipped with a 514.5 nm solid-state laser for excitation. The laser beam, focused to a 4.5 mm diameter spot, was directed through an objective lens featuring ×20 magnification and a numerical aperture of 0.14. A power density of 0.02 W/μm^2, following guidelines from a prior study [26], was applied.

The GSA studies were performed on an Autosorb iQ^3 gas sorption analyzer (Anton Paar QuantaTec, Boynton Beach, FL, USA) using high-purity (99.999%) N_2 and He gases for the adsorption measurements and void volume calculations, respectively, with liquid N_2 at 77 K as a cryogen. The samples (~ 50 mg) were degassed at 250 °C under vacuum for 24 h prior to performing the GSA measurements. To determine the specific surface area, the multi-point Brunauer–Emmett–Teller (BET) method [27] was utilized, adhering to the BET consistency criteria outlined in ISO 9277:2022. This calculation was based on adsorption data at relative pressures (P/P_0) ranging from 0.01 to 0.05. The values for the micropore surface area and

micropore volume were calculated using the t-plot method for carbon black in the relative pressure (P/P_0) interval from 0.2 to 0.5. The pore size distributions were estimated using the quenched solid density functional theory (QSDFT). This method employed the N_2–carbon adsorption branch kernel at 77 K for analyzing mixed slit and cylindrical pores.

The XPS analysis was conducted on a Theta Probe system (Thermo Scientific, Waltham, MA, USA) featuring a monochromated Al Kα X-ray source with 1486.6 eV photon energy. The X-ray spot was focused to approximately 400 µm in diameter. The wide-scan survey spectra were collected at a pass energy of 200 eV, and the high-resolution core level spectra for various elements were obtained with a pass energy of 50 eV.

2.3. Electrochemical Characterization

The electrochemical properties were assessed using a three-electrode configuration in a 1 M KOH solution (pH value 13.89–14.06 [28]) for a catalytic activity analysis (using OER) and a 3 M KOH solution (pH value 14.56–14.74 [28]) for the energy storage studies (using supercapacitors). The setup consisted of a saturated calomel electrode as the reference, a platinum wire as the counter and custom-made electrodes as the working electrodes. These electrodes were fabricated by blending 80 wt.% FLG or Co-FLG with 10 wt.% acetylene black and 10 wt.% polyvinylidene difluoride in N-methyl pyrrolidinone, applied onto nickel foam substrates with a total working electrode area of 0.25 cm^2. For the OER studies, linear sweep voltammetry (LSV) and a Tafel slope analysis were employed to assess the kinetics and efficiency of the catalytic process. For evaluating the supercapacitive behavior, cyclic voltammetry (CV) and long-term durability tests, extending over 5000 cycles, were performed to assess the charge storage efficiency and electrode stability. These tests were conducted using a VersaSTAT 4-500 electrochemical workstation (Princeton Applied Research, Oak Ridge, TN, USA), allowing for a comprehensive analysis of both the catalytic activity and energy storage capabilities.

3. Results and Discussion

3.1. Structural and Morphological Investigations

The field-emission SEM micrographs of both the FLG and Co-FLG samples reveal a mix of individual spherical particle agglomerates, with sizes typically below 1 µm in diameter, at lower magnifications (Figure 1a,d). At higher magnifications (Figure 1b,e), a platelet-like structure is visible. The high-resolution TEM micrographs of the FLG (Figure 1c) reveal individual thin flakes with various structural defects. In contrast, the Co-FLG TEM micrographs (Figure 1f) display a mixture of carbon flakes and spherical particles, the latter appearing

darker and indicating cobalt's presence. The EDX analysis of the FLG identifies a high oxygen content alongside carbon, indicative of successful functionalization. For the Co-FLG sample, EDX confirms the presence of cobalt. The EDX mappings of the spherical agglomerates were conducted for carbon (Figure 1g), oxygen (Figure 1h) and cobalt (Figure 1i), revealing that carbon is uniformly distributed throughout the sample, while cobalt is significantly less predominant and concentrated along specific surface sites of the sample.

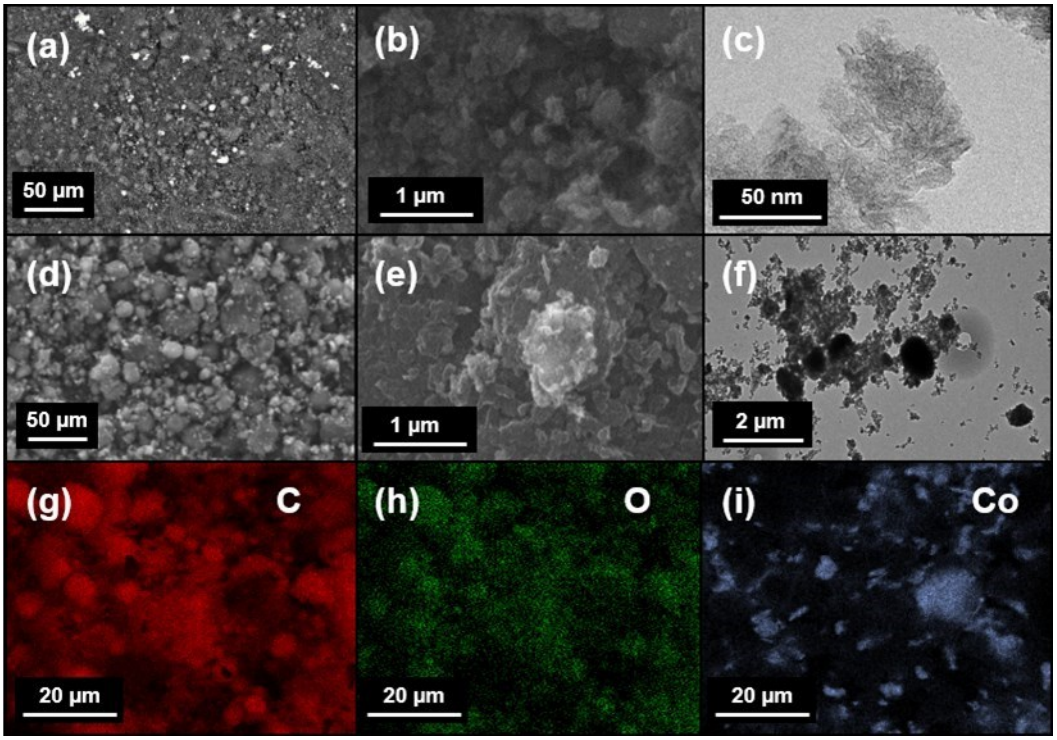

Figure 1. *(**a**,**b**) SEM and (**c**) TEM micrographs for FLG. (**d**,**e**) SEM and (**f**) TEM micrographs for Co-FLG. EDX mappings of Co-FLG for (**g**) carbon, (**h**) oxygen and (**i**) cobalt.*

XRD experiments were conducted, with the diffractograms depicted in Figure 2a. The FLG sample reveals a distinct (002) peak at a diffraction angle 2θ of 26.3° and a broad (100) peak located around 43.3°, both associated with the graphitic structure (International Centre for Diffraction Data card no. 75-1621). The Co-FLG sample reveals graphitic peaks as well as strong contributions attributed to both the face-centered cubic (fcc) and hexagonal close-packed (hcp) phases of cobalt. While the hcp phase is thermodynamically stable at room temperature, the two phases are known to coexist at room temperature [29]. Notably, there are no peaks indicating the presence of cobalt oxides (i.e., CoO and Co_3O_4) in the XRD patterns. Applying Bragg's law, the interplanar spacing d between the individual graphene layers is calculated as 0.338 nm for both samples, slightly higher than the theoretical graphite interlayer spacing of 0.335 nm [30]. Applying Scherrer's equation allows for calculating the crystallite size L_c of 5.7 and 5.4 nm and correspondingly an average number of layers of ~17 and 16 layers for the FLG and Co-FLG, respectively. The striking similarities between both

samples imply that the additional plasma treatment step does not cause significant structural changes to the carbon phase of the Co-FLG sample.

Raman spectroscopy was conducted and the results are shown in Figure 2b, revealing three distinct features known as the D, G and G'(2D) bands of carbons [31] located at 1353, 1576 and 2695 cm^{-1}, respectively. All the peak positions and integrated peak areas are virtually identical for both samples, with the presence of a strong D band suggesting a high defect density in the carbon structure. The shape and position of the G'(2D) band indicates a graphene-based structure with a few layers, rather than graphite [32]. The extensive similarities between both Raman spectra suggest that the incorporation of cobalt does not alter the carbon structure. The anticipated peaks for the cobalt oxides, which would typically appear at 690 cm^{-1} for Co_3O_4 [33] and a broad band around 1060 cm^{-1} for CoO [34,35], are absent, supporting the findings from the XRD. The defect density is calculated for both samples as ~1.88×10^{11} cm^{-2} following a procedure outlined by Cançado et al. [36]. The results of this investigation show that no significant structural evolution of the nanoporous graphene phase was found after conducting the second plasma treatment step.

The results of the gas sorption analysis are depicted in Figure 2c,d. Figure 2c shows the gas adsorption (filled symbols) and desorption (empty symbols) isotherms using N_2 at 77 K. The sharp increase at low relative pressures can be attributed to microporosity (i.e., pore widths below 2 nm). The isotherms are similar in shape, with the FLG sample displaying a significantly higher N_2 adsorption amount throughout the full pressure range. For the concluding point of the adsorption isotherms (P/P_0 ~0.99), the Co-FLG exhibits a reduced N_2 adsorption of roughly 37% compared to the FLG. The desorption branch for both samples shows a small hysteresis, indicating the presence of mesopores (i.e., pore widths between 2 and 50 nm). The adsorption isotherms do not end with a plateau; thus, the Gurvich rule cannot be applied to determine the total pore volume [37]. The isotherms are classified as a mixed Type I and Type IV(a) according to the classification of the International Union of Pure and Applied Chemistry, as both a contribution from the micropores in the low pressure range and the mesopores in the intermediate pressure range is visible [38]. A small step-down in the desorption branch in the P/P_0 range between 0.5 and 0.4 is visible for both samples. This is commonly reported in the literature and is attributed to cavitation-induced N_2 evaporation from the mesopores [37,39]. Thus, the adsorption branch is used for extracting the pore size distribution depicted in Figure 2d. Using the desorption branch would yield an artifact in the pore size distribution in the range between 3 and 4 nm, associated with the cavitation-induced evaporation mechanism [39]. The pore size distribution for both samples is virtually identical, exhibiting a bimodal distribution with peaks at 0.93 and 4.22 nm, thus revealing super-micropores (i.e., pore widths between 0.7 and 2 nm) and small mesopores, respectively. It

seems that there are no pores in the size range of 2 to 2.8 nm present within the investigated samples. The inset in Figure 2d reveals the cumulative pore size distribution for both samples. The BET method reveals apparent surface areas of 780 m^2/g for the FLG and 484 m^2/g for the Co-FLG, which corresponds to a reduction of roughly 38% upon cobalt addition. The t-plot method was employed to extract the micropore surface area and the micropore volume of the given samples. The overall contribution of the micropores is roughly 35% for both samples. The remaining surface area S_{ext} consists of contributions from mesopores, macropores and the external surface. However, a more precise quantification cannot be performed, as the isotherm lacks a plateau in the high-pressure range. Consequently, no mean pore width value can be reported. The results of the GSA are summarized in Table 1. To conclude, both samples show a virtually identical pore size distribution, while Co-FLG displayed a decrease of roughly 38% with respect to both the specific surface area and the micropore volume. This effect is attributed to pore blocking, as previously described in literature [26].

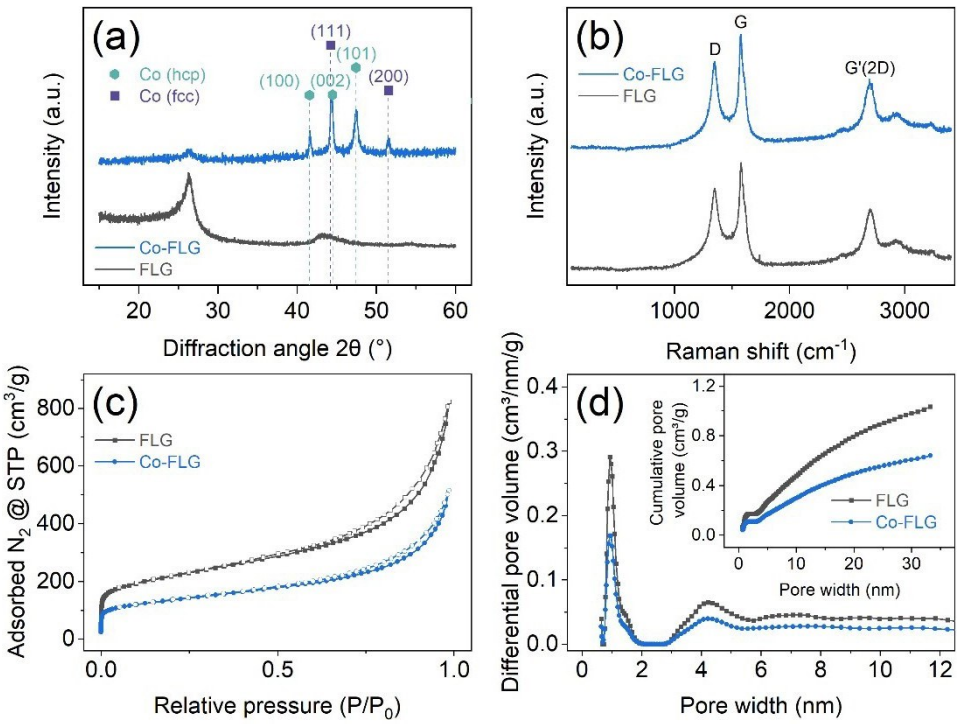

Figure 2. *Results of structural characterization of FLG (black) and Co-FLG (blue): (**a**) X-ray diffractograms with the positions of the main diffraction peaks of the allotropic fcc and hcp phases of cobalt and (**b**) Raman spectra with indications for the D, G and G'(2D) bands. (**c**) Gas adsorption/desorption isotherms for N_2 at 77 K and corresponding (**d**) QSDFT-derived pore size distributions with an inset showing the cumulative pore volume.*

Table 1. *Results of the gas sorption analysis conducted using N_2 at 77 K.*

Material	S_{BET} [m^2/g]	S_{micro} [m^2/g]	S_{ext} [m^2/g]	V_{micro} [cm^3/g]
FLG	780	279	501	0.123
Co-FLG	484	175	309	0.077
Change	−37.9%	−37.3%	−38.4%	−37.4%

S_{BET}: Brunauer–Emmett–Teller (BET) specific surface area. **S_{micro}**: Specific surface area calculated by the statistical thickness t-plot method. **S_{ext}**: Specific surface area contributed by mesopores, macropores and external surfaces, calculated as difference between S_{BET} and S_{micro}. **V_{micro}**: Specific micropore volume calculated by the t-plot method.

XPS measurements were performed to analyze the elemental composition of the samples. Figure 3a presents the wide-scan survey spectra, showing carbon and oxygen in both samples and additionally cobalt in the Co-FLG. A quantitative analysis from the survey scans determines the chemical compositions to be 94.1 and 91.9 at.% of carbon, 5.6 and 6.7 at.% of oxygen, small quantities of nitrogen (0.3 and 0.6 at.%) for the FLG and Co-FLG, respectively, and 0.8 at.% of cobalt for the Co-FLG. This translates to 3.3 wt.% of cobalt, which is slightly lower than the anticipated 4.8 wt.% based on the synthesis procedure.

Figure 3b displays the high-resolution spectra of carbon, where the peak deconvolution reveals the presence of sp^1, sp^2, sp^3, C-O and C=O bonds, along with a π-π* satellite peak in the 290–292 eV region [40]. The spectra are predominantly characterized by sp^2-hybridized carbon bonds associated with the peak position at 284.5 eV, which represent the largest fraction of the carbon content, accounting for ~56% in both examined samples. Contributions from sp^3-hybridized carbon are also significant, comprising ~21% and ~16% for the FLG and Co-FLG samples, respectively, with small contributions from the remaining carbon bonds.

High-resolution oxygen spectra are depicted in Figure 3c, with a peak shape indicative of the presence of OH^- species and adsorbed H_2O. The additional peak at low binding energies corresponds to cobalt oxide formation [41]. Figure 3d confirms cobalt's presence in the Co-FLG, in good agreement with the EDX-derived elemental map for cobalt (see Figure 1i). The Co $2p_{3/2}$ peak occurs at a binding energy of 779.8 eV. This binding energy together with only a weak satellite structure at around 790 eV between the $2p_{3/2}$ and $2p_{1/2}$ peaks is characteristic of Co_3O_4, [41–43], as expected for the native oxide [41]. Based on the theoretical work, cobalt and cobalt oxides are expected to transform into CoOOH under the conditions present during an OER [44].

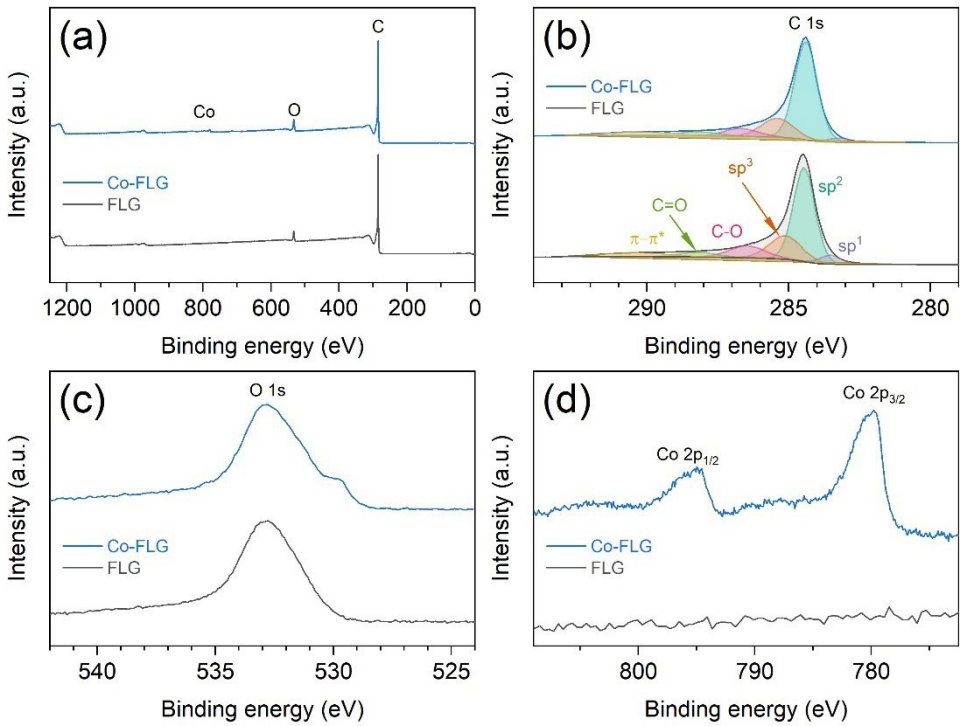

Figure 3. *Results of XPS investigations on FLG (black) and Co-FLG (blue) consisting of a (**a**) survey scan and high-resolution spectra for the elements (**b**) carbon, (**c**) oxygen and (**d**) cobalt.*

The incorporation of cobalt into the FLG, as indicated by Figures 1i, 2a and 3d, leaves the carbon structure unaltered, as evidenced by the Raman spectroscopy and gas sorption analyses. The TEM observations reveal mostly spherical cobalt particles, with their presence further validated by EDX mapping, XRD and XPS. The overall pore size distribution remains consistent despite the cobalt addition. However, a notable reduction in the specific surface area by 38% is observed. The incorporation of cobalt might enable tuning the material's functionality. In the next step, the electrochemical performance differences between FLG and Co-FLG were investigated by means of OER and supercapacitor energy storage applications.

3.2. Electrochemical Characterization

The electrochemical performance of FLG and Co-FLG in terms of the OER was analyzed using LSV, as shown in Figure 4a. As the potential increases, the current density for both materials also increases, which is typical for catalytic processes, as the overpotential provides additional driving force for the reactions. Notably, the Co-FLG exhibits a higher current density than the FLG at potentials beyond approximately 1.55 V, suggesting that cobalt doping enhances the electrocatalytic activity of the graphene material. At a benchmark current density of 10 mA/cm^2, overpotentials of 280 mV for FLG and 290 mV for Co-FLG are observed, comparable to the 300 mV/cm^2 reported by Dou et al. [13] for a porous carbon doped with cobalt nanoparticles in 0.1 M KOH media and mirroring the 290 mV/cm^2 reported by Jia et

al. [45] for cobalt nanoparticles embedded in nitrogen-doped carbon on carbon cloth in a 1 M KOH solution.

A further analysis of the OER kinetics reveals that Co-FLG has a lower Tafel slope (110 mV/dec) compared to FLG (117 mV/dec), as seen in Figure 4b. This suggests that Co-FLG requires a smaller increase in potential to achieve a tenfold increase in current density compared to FLG, which indicates that Co-FLG has a better catalytic efficiency for the OER. The lower Tafel slope of the Co-FLG sample indicates a higher electrocatalytic surface area. The Tafel slope of 117 mV/dec for the FLG sample implies that an electrochemical step is determining the rate-limiting step rather than chemical reactions based on the theoretical works [46,47]. For the case of Co-FLG, the reported Tafel slope of 110 mV/dec is not directly covered by the theoretical calculations in the literature, which also applies for subsequent experimentally derived Tafel slope values. Jia et al. reported various Tafel slopes of 73 and 88 mV/dec for two different types of N-doped carbon cloth materials also doped with cobalt and 253 mV/dec for the N-doped carbon cloth without cobalt addition under a 1 M KOH solution. The synthesis procedure consisted of electrochemically deposited Co_3O_4 nanosheets on the carbon cloth surface [45]. Dou et al. reported a significantly lower Tafel slope of 96.9 mV/dec for a cobalt nanoparticle-doped porous carbon and a lower Tafel slope of 73 mV/dec for a more advanced material system incorporating carbon nanotubes [13], however with no reasons given for the differences in the Tafel slopes. It has to be noted that the cobalt nanoparticles were significantly smaller compared to this work and a 0.1 M KOH solution was used. Mao et al. reported on 3D crumpled graphene–cobalt oxide nanohybrids with an overpotential of 340 mV at 10 mA/cm^2 and Tafel slopes of 71 and 75 mV/dec for N-doped and non-doped versions of the material system [48]. Su et al. reported Tafel slopes between 61.4 and 116.1 mV/dec for cobalt nanoparticles embedded in N-doped carbon with values depending on different synthesis parameters of the material system [49].

The current density was studied as a function of the scan rate (see Figure 4c). Co-FLG is characterized by consistently higher current densities compared to FLG, culminating in a 22% higher current density at the highest tested scan rate of 30 mV/s. This enhancement in electrochemical activity underscores Co-FLG's potential for high-current-density applications.

To summarize, the presented material system is capable of achieving a competitive overpotential at 10 mA/cm^2 while only obtaining intermediate Tafel slopes. The material system could be further enhanced by N-doping the few-layer graphene [3]. This could be performed within the plasma reactor using an additional plasma treatment step with nitrogen gas.

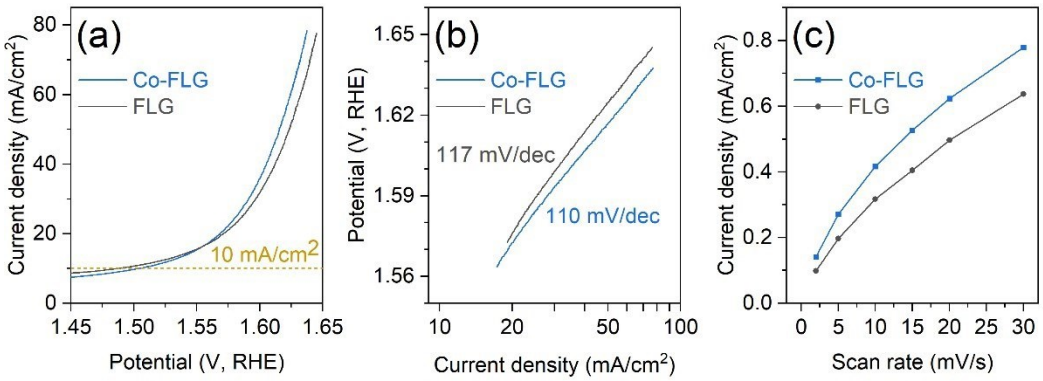

Figure 4. *Characterization of OER performance. (**a**) LSV curves, (**b**) corresponding Tafel slopes and (**c**) current density as a function of the scan rate.*

Figure 5a presents a comparative evaluation of the specific capacitance as a function of the current density for FLG and Co-FLG in supercapacitor applications. Both curves exhibit a decrease in specific capacitance with increasing current density. At a current density of 0.5 A/g, FLG achieves a significantly higher specific capacitance (125.8 F/g) compared to Co-FLG (99.6 F/g), marking a 26% increase. The specific capacitance of FLG decreases significantly with the current density, achieving roughly equal values of 62 F/g at 3 A/g compared to Co-FLG and terminating with 3.6 F/g at the highest measured current density of 20 A/g. In contrast, Co-FLG retains a significantly higher specific capacitance at elevated current densities, i.e., 24.6 F/g at 20 A/g, thus outperforming the conventional FLG by a factor of 6.8. The results for the specific capacitance as a function of the scan rate are depicted in Figure 5b. In a similar fashion to Figure 5a, Co-FLG starts at a lower specific capacitance at low scan rates and outperforms the FLG at higher scan rates, despite a less pronounced difference of 27%. This indicates that Co-FLG might be particularly useful for applications requiring rapid charge–discharge cycles, where maintaining the energy storage capacity is crucial. Benchmarking the performance of supercapacitors is complex, as standardized benchmarks, similar to those for the OER, are absent. Lu et al. addressed this complexity in their recent review, showcasing a range of cobalt-based graphene materials [50]. The Co_3O_4/graphene nanosheets composite prepared by Naveen et al. performed significantly better with 175 F/g at 10 A/g in a 1 M KOH solution (compared to 37.9 F/g for Co-FLG) and with 650 F/g at 5 mV/s (compared to 283 F/g for Co-FLG) in a 1 M KOH solution [15]. Dong et al. reported on a 3D graphene foam–cobalt oxide nanowire electrode achieving 768 F/g at a current density of 10 A/g (compared to 38 F/g for Co-FLG) combined with outstanding cycling stability [51]. Yan et al. reported on a similar nanocomposite synthesized using a plasma-assisted process, achieving 243 F/g at 5 mV/s (compared to 236.7 F/g for Co-FLG) in a 6 M KOH aqueous solution [52].

When the specific capacitance is normalized by the BET specific surface area, yielding values in F/m^2, Co-FLG consistently outperforms FLG. At a current density of 0.5 A/g, Co-FLG

achieves a notable specific capacitance of ~0.21 F/m^2, compared to ~0.16 F/m^2 for FLG. This performance gap widens with increasing current densities; at the highest tested current density of 20 A/g, Co-FLG exceeds FLG by a factor of 11, demonstrating specific capacitances of ~0.051 and ~0.005 F/m^2, respectively. This underlines the enhanced electrochemical performance achieved by the addition of cobalt despite the reduction in the available surface area.

The cycling stability tests (Figure 5c) reveal a gradual decline in capacitance retention for both Co-FLG and FLG over 5000 cycles. FLG performs more favorably, retaining 76% of its original capacitance, while Co-FLG retains 68% after 5000 cycles. The lower capacitance retention of Co-FLG indicates more pronounced degradation from cycling, potentially due to microstructural changes, or the instability of cobalt dopants. Yan et al. reported a slight increase in cyclic capacitance for their nanocomposite within the first 250 cycles and a subsequent decrease to 95% after a total of 2000 cycles, compared to 84% for Co-FLG and 87% for FLG [52]. Vilian et al. reported a retention of 80.5% after 5000 cycles for hexagonal Co_3O_4-anchored reduced graphene oxide sheets [53]. Liu et al. reported an excellent cycling retention of 96% after 5500 cycles for a material system consisting of hierarchical porous carbon frameworks containing ultrafine metallic cobalt nanoparticles [17]. Naveen et al. reported a cycling retention of 92% after 1000 cycles, matching the performance of Co-FLG [15]. Assessing cycling stability suffers from non-uniform testing conditions and the reasons for degradation are rarely discussed within the literature.

To summarize, Co-FLG enhances the supercapacitor performance of the given FLG material and delivers reasonable performance while falling short of matching the best currently available materials. Further optimization of the sample morphology and the length scale of the cobalt phase is suggested to further enhance supercapacitor performance [50]. It has to be noted that the presented performance was achieved by means of physical methods only, thus allowing for a wet-free synthesis procedure, with no comparable results yet published to the best of the authors' knowledge.

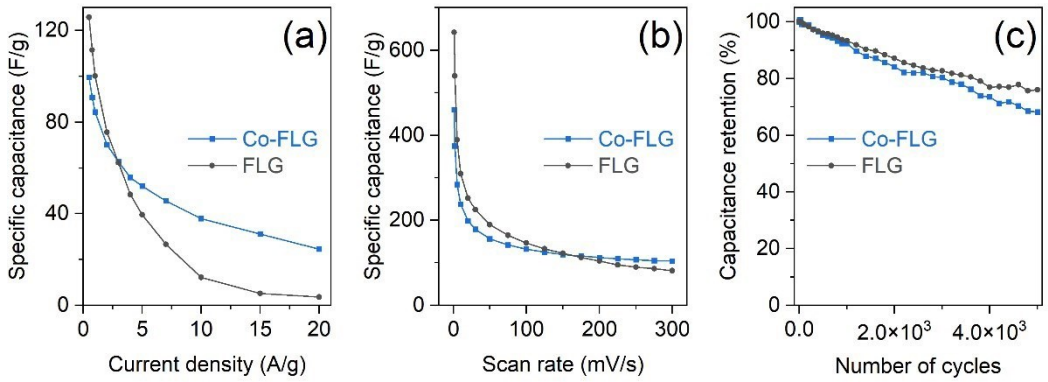

Figure 5. *Supercapacitor performance. (**a**) Specific capacitance as a function of the current, (**b**) specific capacitance as a function of the scan rate and (**c**) capacitance retention over 5000 cycles.*

4. Conclusions

Within this work, we pioneered the synthesis of a nanocomposite of cobalt and nanoporous graphene synthesized by purely physical plasma treatment methods without the need for chemicals and cobalt precursors. We demonstrated for the first time that such processes can be successfully employed to obtain innovative material systems with a competitive oxygen evolution reaction and supercapacitor performance while retaining the advantageous properties of nanoporous graphene. However, the presented method does not yet allow for achieving an electrochemical performance on the same level as the best cobalt–carbon nanocomposites available in the literature. Looking forward, the incorporation of nitrogen into the carbon structure via plasma treatment processes emerges as a potential area for further research, promising to further optimize electrochemical performance.

Acknowledgements

The authors are grateful to Konstantinos Giannakopoulos from NCSR Demokritos (Greece) for the TEM investigations, Georgios Constantinides from the Cyprus University of Technology (Cyprus) for the SEM/EDX investigations and Athanassios G. Kontos from the National Technical University of Athens (Greece) for the Raman spectroscopy investigations.

References

1. Jiao, Y.; Zheng, Y.; Jaroniec, M.; Qiao, S.Z. Design of electrocatalysts for oxygen- and hydrogen-involving energy conversion reactions. *Chem. Soc. Rev.* **2015**, *44*, 2060–2086. https://doi.org/10.1039/C4CS00470A.

2. Bueno, P.R. Nanoscale origins of super-capacitance phenomena. *J. Power Sources* **2019**, *414*, 420–434. https://doi.org/10.1016/j.jpowsour.2019.01.010.
3. Zhang, L.; Xiao, J.; Wang, H.; Shao, M. Carbon-Based Electrocatalysts for Hydrogen and Oxygen Evolution Reactions. *ACS Catal.* **2017**, *7*, 7855–7865. https://doi.org/10.1021/acscatal.7b02718.
4. Pandolfo, A.G.; Hollenkamp, A.F. Carbon properties and their role in supercapacitors. *J. Power Sources* **2006**, *157*, 11–27. https://doi.org/10.1016/j.jpowsour.2006.02.065.
5. Zhai, Z.; Zhang, L.; Du, T.; Ren, B.; Xu, Y.; Wang, S.; Miao, J.; Liu, Z. A review of carbon materials for supercapacitors. *Mater. Des.* **2022**, *221*, 111017. https://doi.org/10.1016/j.matdes.2022.111017.
6. Wen, Z.; Wang, X.; Mao, S.; Bo, Z.; Kim, H.; Cui, S.; Lu, G.; Feng, X.; Chen, J. Crumpled Nitrogen-Doped Graphene Nanosheets with Ultrahigh Pore Volume for High-Performance Supercapacitor. *Adv. Mater.* **2012**, *24*, 5610–5616. https://doi.org/10.1002/adma.201201920.
7. Wu, L.; Li, Q.; Wu, C.H.; Zhu, H.; Mendoza-Garcia, A.; Shen, B.; Guo, J.; Sun, S. Stable Cobalt Nanoparticles and Their Monolayer Array as an Efficient Electrocatalyst for Oxygen Evolution Reaction. *J. Am. Chem. Soc.* **2015**, *137*, 7071–7074. https://doi.org/10.1021/jacs.5b04142.
8. Zhang, Y.; Ouyang, B.; Xu, J.; Jia, G.; Chen, S.; Rawat, R.S.; Fan, H.J. Rapid Synthesis of Cobalt Nitride Nanowires: Highly Efficient and Low-Cost Catalysts for Oxygen Evolution. *Angew. Chem. Int. Ed.* **2016**, *55*, 8670–8674. https://doi.org/10.1002/anie.201604372.
9. Tahir, M.; Pan, L.; Idrees, F.; Zhang, X.; Wang, L.; Zou, J.-J.; Wang, Z.L. Electrocatalytic oxygen evolution reaction for energy conversion and storage: A comprehensive review. *Nano Energy* **2017**, *37*, 136–157. https://doi.org/10.1016/j.nanoen.2017.05.022.
10. Hu, X.; Wang, Y.; Wu, Q.; Li, J. Review of cobalt-based nanocomposites as electrode for supercapacitor application. *Ionics* **2022**, *28*, 989–1015. https://doi.org/10.1007/s11581-021-04319-z.
11. Qiao, X.; Liao, S.; Zheng, R.; Deng, Y.; Song, H.; Du, L. Cobalt and Nitrogen Codoped Graphene with Inserted Carbon Nanospheres as an Efficient Bifunctional Electrocatalyst for Oxygen Reduction and Evolution. *ACS Sustain. Chem. Eng.* **2016**, *4*, 4131–4136. https://doi.org/10.1021/acssuschemeng.6b00451.
12. Wang, Z.; Xiao, S.; Zhu, Z.; Long, X.; Zheng, X.; Lu, X.; Yang, S. Cobalt-Embedded Nitrogen Doped Carbon Nanotubes: A Bifunctional Catalyst for Oxygen Electrode Reactions in a Wide pH Range. *ACS Appl. Mater. Interfaces* **2015**, *7*, 4048–4055. https://doi.org/10.1021/am507744y.
13. Dou, S.; Li, X.; Tao, L.; Huo, J.; Wang, S. Cobalt nanoparticle-embedded carbon nanotube/porous carbon hybrid derived from MOF-encapsulated Co_3O_4 for oxygen electrocatalysis. *Chem. Commun.* **2016**, *52*, 9727–9730. https://doi.org/10.1039/C6CC05244D.
14. Li, X.; Zeng, C.; Jiang, J.; Ai, L. Magnetic cobalt nanoparticles embedded in hierarchically porous nitrogen-doped carbon frameworks for highly efficient and well-recyclable catalysis. *J. Mater. Chem. A* **2016**, *4*, 7476–7482. https://doi.org/10.1039/C6TA01054G.
15. Naveen, A.N.; Manimaran, P.; Selladurai, S. Cobalt oxide (Co_3O_4)/graphene nanosheets (GNS) composite prepared by novel route for supercapacitor application. *J. Mater. Sci. Mater. Electron.* **2015**, *26*, 8988–9000. https://doi.org/10.1007/s10854-015-3582-2.

16. Lakra, R.; Kumar, R.; Sahoo, P.K.; Sharma, D.; Thatoi, D.; Soam, A. Facile synthesis of cobalt oxide and graphene nanosheets nanocomposite for aqueous supercapacitor application. *Carbon Trends* **2022**, *7*, 100144. https://doi.org/10.1016/j.cartre.2021.100144.
17. Liu, B.; Jin, L.; Zheng, H.; Yao, H.; Wu, Y.; Lopes, A.; He, J. Ultrafine Co-based Nanoparticle@Mesoporous Carbon Nanospheres toward High-Performance Supercapacitors. *ACS Appl. Mater. Interfaces* **2017**, *9*, 1746–1758. https://doi.org/10.1021/acsami.6b11958.
18. Yi, M.; Shen, Z. A review on mechanical exfoliation for the scalable production of graphene. *J. Mater. Chem. A* **2015**, *3*, 11700–11715. https://doi.org/10.1039/C5TA00252D.
19. Pei, S.; Cheng, H.-M. The reduction of graphene oxide. *Carbon* **2012**, *50*, 3210–3228. https://doi.org/10.1016/j.carbon.2011.11.010.
20. Tetlow, H.; Posthuma de Boer, J.; Ford, I.J.; Vvedensky, D.D.; Coraux, J.; Kantorovich, L. Growth of epitaxial graphene: Theory and experiment. *Phys. Rep.* **2014**, *542*, 195–295. https://doi.org/10.1016/j.physrep.2014.03.003.
21. Mohan, V.B.; Lau, K.; Hui, D.; Bhattacharyya, D. Graphene-based materials and their composites: A review on production, applications and product limitations. *Compos. Part B Eng.* **2018**, *142*, 200–220. https://doi.org/10.1016/j.compositesb.2018.01.013.
22. Mbayachi, V.B.; Ndayiragije, E.; Sammani, T.; Taj, S.; Mbuta, E.R.; Khan, A. ullah Graphene synthesis, characterization and its applications: A review. *Results Chem.* **2021**, *3*, 100163. https://doi.org/10.1016/j.rechem.2021.100163.
23. Kostoglou, N.; Tarat, A.; Walters, I.; Ryzhkov, V.; Tampaxis, C.; Charalambopoulou, G.; Steriotis, T.; Mitterer, C.; Rebholz, C. Few-layer graphene-like flakes derived by plasma treatment: A potential material for hydrogen adsorption and storage. *Microporous Mesoporous Mater.* **2016**, *225*, 482–487. https://doi.org/10.1016/j.micromeso.2016.01.027.
24. Natter, N.; Kostoglou, N.; Koczwara, C.; Tampaxis, C.; Steriotis, T.; Gupta, R.; Paris, O.; Rebholz, C.; Mitterer, C. Plasma-Derived Graphene-Based Materials for Water Purification and Energy Storage. *C* **2019**, *5*, 16. https://doi.org/10.3390/c5020016.
25. Warren, B.E. X-ray Diffraction in Random Layer Lattices. *Phys. Rev.* **1941**, *59*, 693–698. https://doi.org/10.1103/PhysRev.59.693.
26. Kostoglou, N.; Liao, C.W.; Wang, C.Y.; Kondo, J.N.; Tampaxis, C.; Steriotis, T.; Giannakopoulos, K.; Kontos, A.G.; Hinder, S.; Baker, M.; et al. Effect of Pt nanoparticle decoration on the H2 storage performance of plasma-derived nanoporous graphene. *Carbon* **2021**, *171*, 294–305. https://doi.org/10.1016/j.carbon.2020.08.061.
27. Brunauer, S.; Emmett, P.H.; Teller, E. Adsorption of Gases in Multimolecular Layers. *J. Am. Chem. Soc.* **1938**, *60*, 309–319. https://doi.org/10.1021/ja01269a023.
28. Hausmann, J.N.; Traynor, B.; Myers, R.J.; Driess, M.; Menezes, P.W. The pH of Aqueous NaOH/KOH Solutions: A Critical and Non-trivial Parameter for Electrocatalysis. *ACS Energy Lett.* **2021**, *6*, 3567–3571. https://doi.org/10.1021/acsenergylett.1c01693.

29. Lee, B.W.; Alsenz, R.; Ignatiev, A.; Van Hove, M.A. Surface structures of the two allotropic phases of cobalt. *Phys. Rev. B* **1978**, *17*, 1510–1520. https://doi.org/10.1103/PhysRevB.17.1510.
30. Delhaes, P. *Graphite and Precursors*; Delhaes, P., Ed.; Gordon & Breach Science Publishers: Langhorne, PA, USA, 2001; Volume 1; ISBN 9056992287.
31. Cuesta, A.; Dhamelincourt, P.; Laureyns, J.; Martinez-Alonso, A.; Tascón, J.M.D. Raman microprobe studies on carbon materials. *Carbon* **1994**, *32*, 1523–1532. https://doi.org/10.1016/0008-6223(94)90148-1.
32. Ferrari, A.C.; Meyer, J.C.; Scardaci, V.; Casiraghi, C.; Lazzeri, M.; Mauri, F.; Piscanec, S.; Jiang, D.; Novoselov, K.S.; Roth, S.; et al. Raman Spectrum of Graphene and Graphene Layers. *Phys. Rev. Lett.* **2006**, *97*, 187401. https://doi.org/10.1103/PhysRevLett.97.187401.
33. Hadjiev, V.G.; Iliev, M.N.; Vergilov, I. V The Raman spectra of Co_3O_4. *J. Phys. C Solid State Phys.* **1988**, *21*, L199. https://doi.org/10.1088/0022-3719/21/7/007.
34. Wdowik, U.D.; Parlinski, K. Lattice dynamics of CoO from first principles. *Phys. Rev. B* **2007**, *75*, 104306. https://doi.org/10.1103/PhysRevB.75.104306.
35. Li, Y.; Qiu, W.; Qin, F.; Fang, H.; Hadjiev, V.G.; Litvinov, D.; Bao, J. Identification of Cobalt Oxides with Raman Scattering and Fourier Transform Infrared Spectroscopy. *J. Phys. Chem. C* **2016**, *120*, 4511–4516. https://doi.org/10.1021/acs.jpcc.5b11185.
36. Cançado, L.G.; Jorio, A.; Ferreira, E.H.M.; Stavale, F.; Achete, C.A.; Capaz, R.B.; Moutinho, M.V.O.; Lombardo, A.; Kulmala, T.S.; Ferrari, A.C. Quantifying Defects in Graphene via Raman Spectroscopy at Different Excitation Energies. *Nano Lett.* **2011**, *11*, 3190–3196. https://doi.org/10.1021/nl201432g.
37. Rouquerol, J.; Rouquerol, F.; Llewellyn, P.; Maurin, G.; Sing, K. *Adsorption by Powders and Porous Solids: Principles, Methodology and Applications*; Academic Press: Cambridge, MA, USA, 2013; ISBN 0080970362.
38. Thommes, M.; Kaneko, K.; Neimark, A.V.; Olivier, J.P.; Rodriguez-Reinoso, F.; Rouquerol, J.; Sing, K.S.W. Physisorption of gases, with special reference to the evaluation of surface area and pore size distribution (IUPAC Technical Report). *Pure Appl. Chem.* **2015**, *87*, 1051–1069. https://doi.org/10.1515/pac-2014-1117.
39. Thommes, M.; Cychosz, K.A. Physical adsorption characterization of nanoporous materials: Progress and challenges. *Adsorption* **2014**, *20*, 233–250. https://doi.org/10.1007/s10450-014-9606-z.
40. Rybachuk, M.; Bell, J.M. Electronic states of trans-polyacetylene, poly(p-phenylene vinylene) and sp-hybridised carbon species in amorphous hydrogenated carbon probed by resonant Raman scattering. *Carbon* **2009**, *47*, 2481–2490. https://doi.org/10.1016/j.carbon.2009.04.049.
41. McIntyre, N.S.; Johnston, D.D.; Coatsworth, L.L.; Davidson, R.D.; Brown, J.R. X-ray photoelectron spectroscopic studies of thin film oxides of cobalt and molybdenum. *Surf. Interface Anal.* **1990**, *15*, 265–272. https://doi.org/10.1002/sia.740150406.
42. National Institute of Standards and Technology NIST X-ray Photoelectron Spectroscopy Database (SRD 20), Version 5.0 Available online: https://srdata.nist.gov/xps/ (accessed on 15 February 2024).
43. Vaz, C.A.F.; Prabhakaran, D.; Altman, E.I.; Henrich, V.E. Experimental study of the interfacial cobalt oxide in $Co_3O_4/\alpha{-}Al_2O_3(0001)$ epitaxial films. *Phys. Rev. B* **2009**, *80*, 155457. https://doi.org/10.1103/PhysRevB.80.155457.

44. Bajdich, M.; García-Mota, M.; Vojvodic, A.; Nørskov, J.K.; Bell, A.T. Theoretical Investigation of the Activity of Cobalt Oxides for the Electrochemical Oxidation of Water. *J. Am. Chem. Soc.* **2013**, *135*, 13521–13530. https://doi.org/10.1021/ja405997s.
45. Jia, Q.; Gao, Y.; Li, Y.; Fan, X.; Zhang, F.; Zhang, G.; Peng, W.; Wang, S. Cobalt nanoparticles embedded in N-doped carbon on carbon cloth as free-standing electrodes for electrochemically-assisted catalytic oxidation of phenol and overall water splitting. *Carbon* **2019**, *155*, 287–297. https://doi.org/10.1016/j.carbon.2019.08.031.
46. Fletcher, S. Tafel slopes from first principles. *J. Solid State Electrochem.* **2009**, *13*, 537–549. https://doi.org/10.1007/s10008-008-0670-8.
47. Antipin, D.; Risch, M. Calculation of the Tafel slope and reaction order of the oxygen evolution reaction between pH 12 and pH 14 for the adsorbate mechanism. *Electrochem. Sci. Adv.* **2023**, *3*, e2100213. https://doi.org/10.1002/elsa.202100213.
48. Mao, S.; Wen, Z.; Huang, T.; Hou, Y.; Chen, J. High-performance bi-functional electrocatalysts of 3D crumpled graphene–cobalt oxide nanohybrids for oxygen reduction and evolution reactions. *Energy Environ. Sci.* **2014**, *7*, 609–616. https://doi.org/10.1039/C3EE42696C.
49. Su, Y.; Zhu, Y.; Jiang, H.; Shen, J.; Yang, X.; Zou, W.; Chen, J.; Li, C. Cobalt nanoparticles embedded in N-doped carbon as an efficient bifunctional electrocatalyst for oxygen reduction and evolution reactions. *Nanoscale* **2014**, *6*, 15080–15089. https://doi.org/10.1039/C4NR04357J.
50. Lu, C.; Liu, L.; Yang, Y.; Ma, Y.; Luo, Q.; Zhu, M. Recent Progress in Co_3O_4-Based Nanomaterials for Supercapacitors. *ChemNanoMat* **2023**, *9*, e202200537. https://doi.org/10.1002/cnma.202200537.
51. Dong, X.-C.; Xu, H.; Wang, X.-W.; Huang, Y.-X.; Chan-Park, M.B.; Zhang, H.; Wang, L.-H.; Huang, W.; Chen, P. 3D Graphene–Cobalt Oxide Electrode for High-Performance Supercapacitor and Enzymeless Glucose Detection. *ACS Nano* **2012**, *6*, 3206–3213. https://doi.org/10.1021/nn300097q.
52. Yan, J.; Wei, T.; Qiao, W.; Shao, B.; Zhao, Q.; Zhang, L.; Fan, Z. Rapid microwave-assisted synthesis of graphene nanosheet/Co_3O_4 composite for supercapacitors. *Electrochim. Acta* **2010**, *55*, 6973–6978. https://doi.org/10.1016/j.electacta.2010.06.081.
53. Vilian, A.T.E.; Dinesh, B.; Rethinasabapathy, M.; Hwang, S.-K.; Jin, C.-S.; Huh, Y.S.; Han, Y.-K. Hexagonal Co_3O_4 anchored reduced graphene oxide sheets for high-performance supercapacitors and non-enzymatic glucose sensing. *J. Mater. Chem. A* **2018**, *6*, 14367–14379. https://doi.org/10.1039/C8TA04941F.

8.4 Publication II

Short-Time Magnetron Sputtering for the Development of Carbon–Palladium Nanocomposites

Florian Knabl, Nikolaos Kostoglou, Velislava Terziyska, Steven Hinder, Mark Baker, Etienne Bousser, Claus Rebholz, Christian Mitterer

Nanomaterials, 14 (2024) 164

Short-Time Magnetron Sputtering for the Development of Carbon–Palladium Nanocomposites

Florian Knabl[1], Nikolaos Kostoglou[1], Velislava Terziyska[1], Steven Hinder[2], Mark Baker[2], Etienne Bousser[3], Claus Rebholz[1,4], Christian Mitterer[1]

[1] Department of Materials Science, Montanuniversität Leoben, 8700 Leoben, Austria

[2] Department of Mechanical Engineering Sciences, University of Surrey, Guildford GU27XH, UK

[3] Centre for Characterization and Microscopy of Materials (CM)2, Polytechnique Montréal, Montréal, QC H3T 1J4, Canada

[4] Department of Mechanical and Manufacturing Engineering, University of Cyprus, 1678 Nicosia, Cyprus

Keywords: physical vapor deposition; magnetron sputtering; surface functionalization; palladium; activated carbon cloth; metal–carbon composites;

Abstract

In recent nanomaterials research, combining nanoporous carbons with metallic nanoparticles, like palladium (Pd), has emerged as a focus due to their potential in energy, environmental and biomedical fields. This study presents a novel approach for synthesizing Pd-decorated carbons using magnetron sputter deposition. This method allows for the functionalization of nanoporous carbon surfaces with Pd nano-sized islands, creating metal–carbon nanocomposites through brief deposition times of up to 15 s. The present research utilized direct current magnetron sputtering to deposit Pd islands on a flexible activated carbon cloth substrate. The surface chemistry, microstructure, morphology and pore structure were analyzed using a variety of material characterization techniques, including X-ray photoelectron spectroscopy, X-ray diffraction, Raman spectroscopy, gas sorption analysis and scanning electron microscopy. The results showed Pd islands of varying sizes distributed across the cloth's carbon fibers, achieving high-purity surface modifications without the use of chemicals. The synthesis method preserves the nanoporous structure of the carbon cloth substrate while adding functional Pd islands, which could be potentially useful in emerging fields like hydrogen storage, fuel cells and biosensors. This approach demonstrates the possibility of creating high-quality metal–carbon composites using a simple, clean and economical method, expanding the possibilities for future nanomaterial-based applications.

1. Introduction

Recent research in nanoscience and nanomaterials has increasingly focused on creating efficient and cost-effective nanoscale composites. In particular, nanocomposites composed of nanostructured and/or nanoporous carbons, such as activated carbons, templated mesoporous carbons, carbon nanotubes, few-layer graphene and others and metallic and/or inorganic nano-sized particles, clusters or thin films, have gained significant attention for emerging energy [1,2], environmental [3] and biomedical applications [4]. This is due to the attractive properties of the individual phases and also because of potential synergistic effects [5].

In this respect, palladium (Pd), a member of the platinum group metal family, has shown promising catalytic activity with a variety of uses, e.g., as an essential component in catalytic converters to reduce harmful emissions in the transport sector. Switching from bulk Pd to nanostructured Pd can offer numerous advantages, e.g., reduced use of scarce and costly resources or resulting from changes in physical and chemical properties, largely influenced by the higher surface area-to-volume ratio. Pd-based nanomaterials, like Pd nanoparticles (NPs), are used in various emerging fields, including biomedicine for antibacterial activity and anticancer therapy [6]. In energy sectors, they find roles in fuel cells [7] and hydrogen storage [8,9]. Additionally, these nanomaterials are used in electronics for sensor applications [10].

Pd NPs can be synthesized via a plethora of physical, chemical and biological methods. Physical methods include magnetron sputter inert gas condensation [11–13] and laser ablation [14], while chemical methods include electrochemical deposition and wet chemistry (e.g., sol–gel methods) [10]. In the field of biology, naturally occurring biomolecules or metabolites from different organisms are used, with a recent summary given by Joudeh et al. [10]. Growth of Pd thin films was, to the best of the authors' knowledge, already studied in 1972 by Sing and Murr [15] and the interest increased significantly with the development of magnetron sputtering [16]. A first study on the morphology of sputter-coated Cu, W and Pd was reported by Haas and Birringer in 1992 [17].

Referring to possible substrates, nanoporous carbon-based fabrics, cloths and felts composed of activated carbon fibers have been proposed as promising hosts for NPs, mainly because of their lightweight nature, increased mechanical integrity/flexibility, good thermo-chemical stability, large surface area and high porosity [1–3,18]. These types of materials offer additional benefits in terms of practicality and ease of handling compared to others (e.g., fine/volatile powders), thus being more likely to be employed as functional components in devices and systems where mechanical robustness plays an important role. In this respect,

Pd-decorated activated carbon cloths have been suggested in the literature to be employed in high-tech applications such as sorbents for hydrogen storage [19,20], cathodes for the oxygen reduction reaction [21], biosensors [22] as well as hydrogen sensing [23,24].

Within this work, it is shown for the first time that conventional magnetron sputter deposition processes may be utilized for the functionalization of nanoporous carbon cloths with Pd nano-sized islands to develop metal–carbon composite materials through brief deposition times (in a matter of seconds). Pd island-decorated carbon cloths were synthesized by varying the deposition times. Under the applied conditions and with the expected stronger interaction between Pd–Pd compared to Pd–C atoms, three-dimensional island growth can be expected to dominate (Volmer–Weber growth) [25]. Sample morphology, surface chemistry, microstructure and pore structure of the synthesized Pd-island-decorated carbon cloths were assessed using a series of materials characterization methods, including X-ray photoelectron spectroscopy (XPS), X-ray diffraction (XRD), Raman spectroscopy, gas sorption analysis (N_2@77 K), and scanning electron microscopy (SEM). These studies revealed coverage with Pd islands of varying rates and sizes “sprinkled” on the surface of the carbon fibers. The proposed approach combines the key advantages of a clean, physical synthesis procedure, free of chemical precursors with high-purity surface modifications, while avoiding the high costs and lack of accessibility associated with dedicated magnetron sputter inert gas condensation systems used for gas-phase NP synthesis. The larger NP size range synthesized by this method is not readily achieved with magnetron sputter inert gas condensation, as the latter usually yields comparatively smaller NPs (i.e., <20 nm).

2. Materials and Methods

2.1. Synthesis of Activated Carbon Cloth Substrates

For this study, a woven activated carbon cloth (ACC) was employed as the substrate material. Viscose rayon cloth (VRC) was used as the precursor material for the ACC. At first, the VRC was impregnated into a mixture of zinc chloride ($ZnCl_2$) and ammonium chloride (NH_4Cl) aqueous solution, with remnants of those chemical compounds confirmed via XPS during subsequent characterization steps. The soaked VRC sample was then air-dried and carbonized up to 630 °C under N_2 atmosphere. A final activation step using CO_2 was performed up to 930 °C. The ACC obtained after additional washing and drying steps retains the cloth structure of the VRC and is thus both flexible and mechanically stable. The ACC substrate and its possible applications were previously presented by our research group [26] and more details about the synthesis procedure can be found in earlier studies by Babic and co-

workers [27,28]. The ACC substrates used within this study were cut to square pieces with approximate dimensions of 14 mm × 14 mm, with each piece weighing around 100 mg.

2.2. Synthesis of Carbon–Palladium Nanocomposites

The deposition experiments were conducted using a custom-made laboratory-scale unbalanced direct current (DC) magnetron sputtering system, already described in detail in earlier studies [29]. This system is equipped with three 50.8 mm diameter unbalanced AJA A320-XP magnetrons focused towards a rotating substrate holder. While two of these magnetrons were not used for this work, a Pd target (99.99% purity, 6 mm in thickness), supplied by Kurt J. Lesker (Jefferson Hills, PA, USA), was employed for sputtering using the third magnetron. Prior to deposition, the vacuum chamber was evacuated to a base pressure below 2×10^{-5} mbar. Pumping was carried out using a turbomolecular pump backed by a rotary vane pump. The substrates were positioned on a rotating substrate holder within the deposition system and rotated at 50 rpm during etching and deposition. Samples were kept under vacuum for 2 h prior to etching with no additional heat being applied during both etching and deposition. Substrate etching was carried out for 60 s with a closed shutter using an etching current of 0.1 A, an asymmetrically pulsed DC voltage of −500 V with 50 kHz and an Argon (Ar) gas flow of 200 sccm (corresponding to a pressure of 3×10^{-2} mbar) in order to clean the substrate surface. Simultaneously, the Pd target underwent sputter cleaning with closed shutters. Prior to the deposition, the Pd target was pre-sputtered for 5 min to ensure a clean target surface as well as stable sputtering conditions.

The deposition process was conducted in constant-current mode set at 0.1 A, with an Ar gas flow of 30 sccm, corresponding to a pressure of 5×10^{-3} mbar, and a target-to-substrate distance of 45 mm. Process parameters were determined in preliminary, unpublished studies and chosen to ensure a low deposition rate while maintaining a stable plasma throughout the deposition. During deposition, no external heating was employed, and the substrates were maintained at a floating potential as no bias voltage was applied. The deposition time was controlled using a shutter. Three samples were prepared with varying deposition times of 5, 10 and 15 s on each side of the ACC substrates. These samples were subsequently labeled as *Pd-ACC-5s*, *Pd-ACC-10s* and *Pd-ACC-15s*, respectively, for the purpose of this work, with the pristine/uncoated reference sample labeled as *ACC*.

2.3. Characterization Methods

XPS measurements were conducted with a Thermo Scientific Theta Probe system (Waltham, MA, USA), which uses a monochromated Al Kα X-ray source (1486.6 eV photon energy) and a ~400 µm in radius X-ray spot. Wide-scan survey spectra and high-resolution core level spectra for the different components were collected with a pass energy of 300 eV and

50 eV, respectively. To compensate for potential charging effects that might occur during the measurement process, all acquired spectra were charge referenced to the C1s peak at 284.5 eV (sp^2 hybridized carbon). For the quantitative analysis of the chemical compositions, the high-resolution core level spectra were adjusted by instrument-modified Wagner sensitivity factors, upon applying a non-linear Shirley background subtraction.

XRD studies were carried out using a Bruker-AXS D8 Advance diffractometer (Billerica, MA, USA), which utilizes Cu Kα radiation (~0.154 nm wavelength), operating at a 40 kV voltage and a 40 mA current. Diffraction patterns were obtained using the Bragg–Brentano configuration with a continuous scan speed between the diffraction angles 2θ 10–90°, advancing at a 0.01° step width and a 0.5°/min scanning rate.

Raman spectra were recorded using a Jobin–Yvon LABRAM confocal spectrometer (Lille, France), which is equipped with a frequency-doubled Nd-YAG laser (532.2 nm emission wavelength) and a Peltier-cooled slow-scan charge-coupled device matrix detector. The laser beam was focused using an Olympus BX 40 microscope, fitted with a ×50 long-working distance objective lens, using a 0.1 mW/μm^2 power density and a 1.5 cm^{-1} spatial resolution. The spectroscopic data were collected in the wavenumber region of 500–2000 cm^{-1}.

Nitrogen (N_2) gas adsorption and desorption isotherms were collected at 77 K (−196 °C) with an Anton Paar QuantaTec Autosorb-iQ^3 manometric gas sorption analyzer (Boynton Beach, FL, USA) by employing ultra-pure (99.999%) N_2 gas as adsorbate, ultra-pure (99.999%) helium (He) gas for void volume calculations and liquid N_2 as cryogen. Prior to the tests, cloth samples of ~40 mg were degassed under vacuum (10^{-6} mbar) at 250 °C for 24 h to remove physisorbed surface species and make the nanopore structure more accessible. The specific surface area was calculated by applying the multi-point Brunauer-Emmett-Teller (BET) method, following the BET consistency criteria (ISO 9277:2022) in the adsorption data for relative pressures (P/P_0) between 0.01 and 0.05. The specific pore volume for pores smaller than 57 nm was estimated using the single-point Gurvich rule at P/P_0 ~0.96. The micropore surface area and micropore volume values were determined by applying the Carbon Black statistical thickness (t-plot) method in the P/P_0 range 0.2–0.5. The pore size/width distribution and mean pore size/width were deduced using the quenched solid density functional theory (QSDFT) method based on the N_2-carbon equilibrium transition kernel at 77.35 K for slit-shaped pores.

SEM investigations were performed using a Zeiss Merlin ultra-high-resolution field emission gun scanning electron microscope (Oberkochen, Germany) equipped with a Gemini II column. Secondary electron images using an InLens detector and back-scattered electron images were acquired at 4 kV acceleration voltage. The elemental maps for carbon

and palladium were collected with two parallel integrated Oxford Instruments XMAX 150 mm^2 energy dispersive X-ray spectroscopy (EDX) detectors using the same acceleration voltage.

3. Results and Discussion

3.1. Surface Chemistry and Elemental Composition

In the first step of the investigation, XPS measurements of all samples (pure and Pd-decorated) were conducted to determine the surface chemical composition. The XPS survey spectra revealed that all samples contained the elements of C, O, N, as well as small traces of Zn and Cl, with the latter stemming from the carbon cloth synthesis process (i.e., impregnation into an aqueous mixture of NH_4Cl and $ZnCl_2$ prior to carbonization). This is consistent with earlier reports on the chemical composition of the carbon cloth substrate [26]. The average Pd content was determined as 0, 0.8, 1.8 and 2.6 at % for the pure *ACC* reference and the subsequent samples ranging from 5 s to 15 s of deposition time, thus revealing maximum Pd content at 15 s. To facilitate characterization, subsequent investigations were focused on this particular Pd-rich sample. A comparison of the XPS survey spectra of pure *ACC* and *Pd-ACC-15s* samples is given in Figure 1a, revealing a distinct Pd peak for the Pd-decorated sample, among multiple other elements. High-resolution spectra in the binding energy range of Pd are depicted in Figure 1b, showing the presence of a peak doublet of the Pd 3d orbital in the *Pd-ACC-15s* sample and a lack thereof in the pure *ACC* sample. The Pd $3d_{5/2}$ spectrum in Figure 1b shows the presence of two peaks at binding energies of 335.6 eV and 337.5 eV, corresponding to Pd metal and its native oxide, respectively. These binding energies are generally in good agreement with those presented in other studies [30–32], but shifted to a slightly higher binding energy. Such positive electron binding energy shifts have been previously reported for nano-sized particles on surfaces, including Pd on amorphous carbon [33].

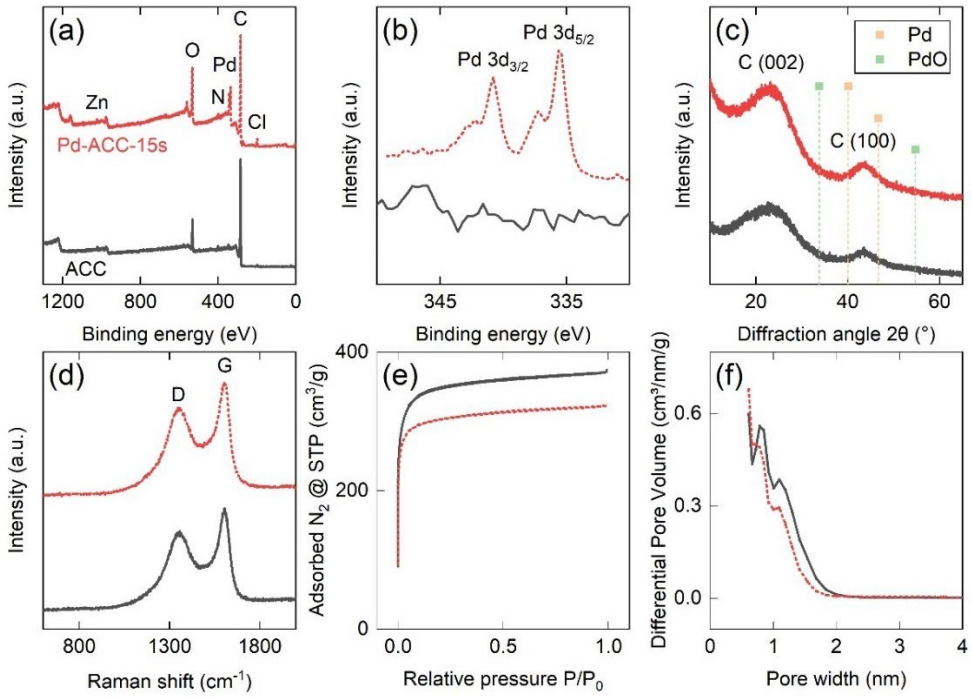

Figure 1. *(**a**) Wide-scan X-ray photoelectron survey spectra and (**b**) high-resolution Pd spectra, (**c**) X-ray diffractograms, (**d**) Raman spectra, (**e**) N_2 adsorption and desorption isotherms recorded at 77 K and (**f**) pore size distribution analysis derived by the quenched solid density functional theory method for slit-shaped pores for the pure ACC and Pd-ACC-15s samples.*

3.2. Microstructural Characterization

Subsequent structural characterization studies were carried out using XRD with the respective diffractograms shown in Figure 1c. For both samples, a broad peak roughly centered at 2θ ~23° and with a full width at half maximum of ~15° was observed. An additional peak of much lower intensity was recorded between 43° and 44°. These peaks are commonly reported in carbons with a low structural order, such as turbostratic carbons, and are related to the (002) and (100) reflections of graphite, respectively [26]. Even for the highest Pd content among the investigated samples, no obvious structural changes were visible from the X-ray diffractograms before and after Pd deposition. In addition, no other peaks were recorded at positions related to Pd or corresponding Pd oxides, being in good agreement with the obtained low Pd content determined by XPS and/or indicating amorphous growth. Furthermore, Raman spectroscopy studies (Figure 1d) revealed distinct defect-activated D and graphitic G bands of identical appearance in the exact same Raman shifts (i.e., ~1350 cm^{-1} and ~1605 cm^{-1}, respectively) and with comparable D/G intensity ratios (i.e., 0.78 vs. 0.77, respectively), thus implying that no structural changes are caused in the carbon cloth substrate due to the Pd deposition process.

3.3. Pore Structure Properties

A follow up investigation in terms of gas sorption analysis was carried out by recording N_2 adsorption and desorption isotherms at 77 K, as depicted in Figure 1e. Both materials demonstrate characteristic fully reversible Type I isotherm shapes according to the classification of the International Union of Pure and Applied Chemistry (IUPAC) [34], associated with the dominant presence of micropores (i.e., pore sizes/widths below 2 nm). Both isotherms indicate a significant and comparable uptake of N_2 already at very low relative pressures ($P/P_0 < 10^{-5}$) due to enhanced gas–solid interactions in sub-nanometer pores, followed by the formation of a clear saturation plateau due the complete filling of the accessible micropore volume [34]. The overall N_2 uptake at higher relative pressures is reduced by ~12% for the Pd-decorated sample. This might be explained by a limited pore blocking effect caused by the Pd decoration procedure, a phenomenon commonly reported in the literature [35,36]. The pore size/width distribution was extracted from the desorption branch of the isotherm, as seen in Figure 1f, and revealed a trimodal pore size distribution with the strongest contributions stemming from pores with widths of ~0.6, ~0.8 and ~1.1 nm, thus further confirming the presence of both ultra-micropores (<0.7 nm) and super-micropores (i.e., 0.7–2 nm), as classified by the IUPAC.

Table 1 highlights the changes in the pore structure features, including specific surface area, specific pore volume, micropore surface area/volume and mean pore size/width, before and after the 15 s sputtering procedure. The BET surface area of the pure *ACC* (1365 m^2/g) decreased by ~12% upon Pd deposition, while similar trends were also found for the change in the total pore volume, micropore surface area and micropore volume. The d_{50} value, corresponding to a pore width of the 50% of the QSDFT-derived pore volume, slightly shifted from 0.77 to 0.67 nm upon Pd deposition. This implies that most of the change in pore volume occurs at larger pore widths while smaller pores are not significantly affected. This is also supported by the fact that the percentage of microporosity (i.e., ratio of micropore volume to total pore volume) remains the same after deposition, i.e., ~88% for both pure *ACC* and *Pd-ACC-15s* samples. The findings of the gas sorption analysis confirm that the nanopore structure of the Pd-decorated sample is not significantly affected by the magnetron sputter deposition process, despite the small reduction of the available surface area and pore volume.

Table 1. *Comprehensive results of the gas sorption analysis deduced by N_2 adsorption/desorption data recorded at 77 K for the ACC and Pd-ACC-15s samples.*

Material	S_{BET} [m^2/g]	S_{micro} [m^2/g]	$V_{Gurvich}$ [cm^3/g]	V_{micro} [cm^3/g]	d_{50} [nm]
ACC	1365	1279	0.57	0.50	0.77
Pd-ACC-15s	1202	1131	0.50	0.44	0.67
Change	−11.9%	−11.6%	−12.3%	−12%	−12.1%

S_{BET}: Brunauer–Emmett–Teller (BET) specific surface area. **S_{micro}**: micropore specific surface area calculated by the Carbon Black statistical thickness (t-plot) method. **$V_{Gurvich}$**: total specific pore volume at P/P_0 ~0.96 for pores smaller than 57 nm in width calculated by the single-point Gurvich rule. **V_{micro}**: specific micropore volume calculated by the t-plot method. **d_{50}**: the pore width corresponding to 50% of the cumulative specific pore volume, as determined by the quenched solid functional theory (QSDFT) method for slit-shaped pores.

3.4. Surface Morphology

Finally, high-resolution SEM and EDX investigations were carried out. A representative collection of the SEM images and elemental maps for the *Pd-ACC-15s* sample is given in Figure 2. In detail, Figure 2a shows an individual carbon fiber of the cloth, showing a corrugated circumference with a width/diameter of roughly 10 µm. Higher magnifications (Figure 2b,c) reveal the development of particles appearing brighter in contrast on the dark carbon fiber surface. The morphology may be described as nano-sized islands or clusters sticking to the surface of the carbon cloth, ranging from smaller, typically spherical islands with a size of ~10 nm to larger, elongated features stretching up to 200 nm in length, with a width of ~80 nm. EDX mappings were performed in the area depicted in Figure 2d and were conducted for the elements of carbon (C) (Figure 2e) and Pd (Figure 2f). These elemental mappings confirm that the islands detected on the carbon cloth surface consist of Pd, while the non-decorated areas show a significantly increased carbon content. These results agree well with the findings of the XPS studies. However, it cannot currently be determined whether these nano-sized islands are amorphous, or their content is too small to be detected by XRD.

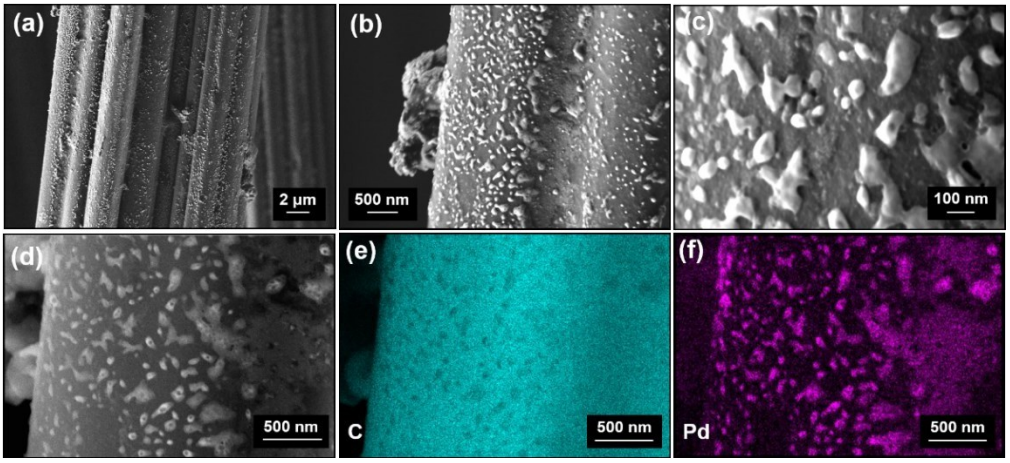

Figure 2. *(**a**–**c**) In-lens field emission scanning electron microscopy micrographs (topography contrast) in different magnifications and (**d**) backscatter electron micrograph (chemical contrast) for the Pd-ACC-15s sample. Energy dispersive X-ray spectroscopy mappings were recorded for (**e**) carbon and (**f**) palladium elements.*

3.5. Discussion on Growth Mechanisms

In contrast, the development of a continuous Pd film would require significantly longer deposition times to achieve the coalescence of the islands and nano-rods, as demonstrated in fundamental works on thin film growth [25,43]. Growth of small Pd islands consisting of, on average, 60 atoms on Au(111) surfaces was reported by Stephenson et al. using Pd evaporation under low deposition rates [44]. To the best of the authors' knowledge, no comparable surface morphology has been previously obtained for Pd deposited on carbon fibers using the DC magnetron sputtering processes. It should also be noted here that the applied DC magnetron sputtering technique offers excellent scalability to large area deposition [45], where the flexible ACC substrate even enables the high-throughput synthesis of such nanocomposites via roll-to-roll sputter deposition processes [46]. The flexible nature of the ACC substrate may even enable achieving a relatively homogeneous distribution of the Pd islands, when coating deposition is performed from both sides of the ACC substrate passing the magnetrons with varying bending radii and thus exposing shaded areas to the incoming flux of sputtered Pd atoms.

4. Conclusions

Within this work, we demonstrated for the first time that a laboratory-scale conventional direct current magnetron sputtering process could be effectively used for synthesizing Pd nano-sized islands, clusters or nanoparticles for the functionalization of

activated carbon cloths, thus obtaining a metal–carbon nanocomposite material. The advantages of this synthesis method include the high purity of the deposited material due to the high purity of the metal target and the lack of chemical precursors, as is required for wet chemistry methods. Furthermore, more expensive and complex methods such as magnetron sputter inert gas condensation can be avoided. The suggested nanocomposite material concept could be potentially employed in emerging technologies, including cathodes for the oxygen reduction reaction in fuel cells, sorbents for materials-based hydrogen storage and sensing applications as well as detectors and sensors for biomolecules. In addition, sputter deposition methods are known for their scalability, enabling the large-scale synthesis of such complex Pd–carbon nanocomposites.

Acknowledgements

The authors are grateful to Branko Matovic, Biljana Babic and Ana Kalijadis from the Vinča Institute of Nuclear Sciences (Belgrade, Serbia) for their support with the development of the ACC material.

References

1. Shi, H.; Wen, G.; Nie, Y.; Zhang, G.; Duan, H. Flexible 3D carbon cloth as a high-performing electrode for energy storage and conversion. *Nanoscale* **2020**, *12*, 5261–5285. https://doi.org/10.1039/C9NR09785F.
2. Liu, X.; Xu, W.; Zheng, D.; Li, Z.; Zeng, Y.; Lu, X. Carbon cloth as an advanced electrode material for supercapacitors: Progress and challenges. *J. Mater. Chem. A* **2020**, *8*, 17938–17950. https://doi.org/10.1039/D0TA03463K.
3. Cukierman, A.L. Development and Environmental Applications of Activated Carbon Cloths. *ISRN Chem. Eng.* **2013**, *2013*, 261523. https://doi.org/10.1155/2013/261523.
4. Teradal, N.L.; Jelinek, R. Carbon Nanomaterials in Biological Studies and Biomedicine. *Adv. Healthc. Mater.* **2017**, *6*, 1700574. https://doi.org/10.1002/adhm.201700574.
5. Omanović-Mikličanin, E.; Badnjević, A.; Kazlagić, A.; Hajlovac, M. Nanocomposites: A brief review. *Health Technol.* **2020**, *10*, 51–59. https://doi.org/10.1007/s12553-019-00380-x.
6. Phan, T.T.; Huynh, T.-C.; Manivasagan, P.; Mondal, S.; Oh, J. An Up-To-Date Review on Biomedical Applications of Palladium Nanoparticles. Nanomaterials 2020, 10, 66. https://doi.org/10.3390/nano10010066.
7. Antolini, E. Palladium in fuel cell catalysis. *Energy Environ. Sci.* **2009**, *2*, 915–931. https://doi.org/10.1039/b820837a.
8. Parambhath, V.B.; Nagar, R.; Ramaprabhu, S. Effect of Nitrogen Doping on Hydrogen Storage Capacity of Palladium Decorated Graphene. *Langmuir* **2012**, *28*, 7826–7833. https://doi.org/10.1021/la301232r.

9. Adams, B.D.; Chen, A. The role of palladium in a hydrogen economy. *Mater. Today* **2011**, *14*, 282–289. https://doi.org/10.1016/S1369-7021(11)70143-2.
10. Joudeh, N.; Saragliadis, A.; Koster, G.; Mikheenko, P.; Linke, D. Synthesis methods and applications of palladium nanoparticles: A review. *Front. Nanotechnol.* **2022**, *4*, 1062608. https://doi.org/10.3389/fnano.2022.1062608.
11. Chamorro-Coral, W.; Caillard, A.; Brault, P.; Andreazza, P.; Coutanceau, C.; Baranton, S. The role of oxygen on the growth of palladium clusters synthesized by gas aggregation source. *Plasma Process. Polym.* **2019**, *16*, e1900006. https://doi.org/10.1002/ppap.201900006.
12. Pérez-Tijerina, E.; Pinilla, M.G.; Mejía-Rosales, S.; Ortiz-Méndez, U.; Torres, A.; José-Yacamán, M.; Perez-Tijerina, E.; Gracia Pinilla, M.; Mejıá-Rosales, S.; Ortiz-Mendez, U.; et al. Highly size-controlled synthesis of Au/Pd nanoparticles by inert-gas condensation. *Faraday Discuss.* **2008**, *138*, 353–362. https://doi.org/10.1039/b705913m.
13. Mattei, J.-G.; Grammatikopoulos, P.; Zhao, J.; Singh, V.; Vernieres, J.; Steinhauer, S.; Porkovich, A.; Danielson, E.; Nordlund, K.; Djurabekova, F.; et al. Gas-Phase Synthesis of Trimetallic Nanoparticles. *Chem. Mater.* **2019**, *31*, 2151–2163. https://doi.org/10.1021/acs.chemmater.9b00129.
14. Cristoforetti, G.; Pitzalis, E.; Spiniello, R.; Ishak, R.; Giammanco, F.; Muniz-Miranda, M.; Caporali, S. Physico-chemical properties of Pd nanoparticles produced by Pulsed Laser Ablation in different organic solvents. *Appl. Surf. Sci.* **2012**, *258*, 3289–3297. https://doi.org/10.1016/j.apsusc.2011.11.084.
15. Singh, H.P.; Murr, L.E. Nucleation and growth characteristics of palladium and indium thin films. *Metall. Trans.* **1972**, *3*, 983–988. https://doi.org/10.1007/BF02647676.
16. Kelly, P.J.; Arnell, R.D. Magnetron sputtering: A review of recent developments and applications. *Vacuum* **2000**, *56*, 159–172. https://doi.org/10.1016/S0042-207X(99)00189-X.
17. Haas, V.; Birringer, R. The morphology and size of nanostructured Cu, Pd and W generated by sputtering. *Nanostruct. Mater.* **1992**, *1*, 491–504. https://doi.org/10.1016/0965-9773(92)90082-9.
18. Tenny, K.M.; Forner-Cuenca, A.; Chiang, Y.-M.; Brushett, F.R. Comparing Physical and Electrochemical Properties of Different Weave Patterns for Carbon Cloth Electrodes in Redox Flow Batteries. *J. Electrochem. Energy Convers. Storage* **2020**, *17*, 041010. https://doi.org/10.1115/1.4046661.
19. Chen, C.-H.; Chung, T.-Y.; Shen, C.-C.; Yu, M.-S.; Tsao, C.-S.; Shi, G.-N.; Huang, C.-C.; Ger, M.-D.; Lee, W.-L. Hydrogen storage performance in palladium-doped graphene/carbon composites. *Int. J. Hydrogen Energy* **2013**, *38*, 3681–3688. https://doi.org/10.1016/j.ijhydene.2013.01.070.
20. Erdogan, F.O.; Celik, C.; Turkmen, A.C.; Sadak, A.E.; Cucu, E. Hydrogen sorption studies of palladium decorated graphene nanoplatelets and carbon samples. *Int. J. Hydrogen Energy* **2023**, *48*, 21476–21486. https://doi.org/10.1016/j.ijhydene.2023.01.026.
21. Chen, A.; Ostrom, C. Palladium-Based Nanomaterials: Synthesis and Electrochemical Applications. *Chem. Rev.* **2015**, *115*, 11999–12044. https://doi.org/10.1021/acs.chemrev.5b00324.
22. Huang, J.; Liu, Y.; Hou, H.; You, T. Simultaneous electrochemical determination of dopamine, uric acid and ascorbic acid using palladium nanoparticle-loaded carbon nanofibers modified electrode. *Biosens. Bioelectron.* **2008**, *24*, 632–637. https://doi.org/10.1016/j.bios.2008.06.011.

23. Joshi, R.K.; Krishnan, S.; Yoshimura, M.; Kumar, A. Pd nanoparticles and thin films for room temperature hydrogen sensor. *Nanoscale Res. Lett.* **2009**, *4*, 1191–1196. https://doi.org/10.1007/s11671-009-9379-6pre.
24. Jiang, H.; Yu, Y.; Zhang, L.; Zhu, J.; Zhao, X.; Zhang, W. Flexible and Highly Sensitive Hydrogen Sensor Based on Organic Nanofibers Decorated by Pd Nanoparticles. *Sensors* **2019**, *19*, 1290. https://doi.org/10.3390/S19061290.
25. Pócza, J.F.; Barna, A.; Barna, P.B.; Pozsgai, I.; Radnóczi, G. In situ electron microscopy of thin film growth. *Jpn. J. Appl. Phys.* **1974**, *13*, 525. https://doi.org/10.7567/JJAPS.2S1.525.
26. Kostoglou, N.; Koczwara, C.; Prehal, C.; Terziyska, V.; Babic, B.; Matovic, B.; Constantinides, G.; Tampaxis, C.; Charalambopoulou, G.; Steriotis, T.; et al. Nanoporous activated carbon cloth as a versatile material for hydrogen adsorption, selective gas separation and electrochemical energy storage. *Nano Energy* **2017**, *40*, 49–64. https://doi.org/10.1016/j.nanoen.2017.07.056.
27. Babić, B.M.; Milonjić, S.K.; Polovina, M.J.; Kaludierović, B. V Point of zero charge and intrinsic equilibrium constants of activated carbon cloth. *Carbon* **1999**, *37*, 477–481. https://doi.org/10.1016/S0008-6223(98)00216-4.
28. Polovina, M.; Babić, B.; Kaluderović, B.; Dekanski, A. Surface characterization of oxidized activated carbon cloth. *Carbon* **1997**, *35*, 1047–1052. https://doi.org/10.1016/S0008-6223(97)00057-2.
29. Kölbl, L.; Mitterer, C.; Franz, R. Synthesis of crystalline silver niobate thin films opening pathways for future process development. *Vacuum* **2023**, *213*, 112077. https://doi.org/10.1016/j.vacuum.2023.112077.
30. Thermo Fisher Scientific Inc. Palladium X-ray Photoelectron Spectra, Palladium Electron Configuration, and Other Elemental Information. Available online: https://www.thermofisher.com/uk/en/home/materials-science/learning-center/periodic-table/transition-metal/palladium.html (accessed on 24 November 2023).
31. *Practical Surface Analysis, Auger and X-ray Photoelectron Spectroscopy (Volume 1)*, 2nd ed.; Briggs, D., Seah, M.P., Eds.; Wiley: Hoboken, NJ, USA, 1996; ISBN 978-0471920816.
32. Kibis, L.S.; Titkov, A.I.; Stadnichenko, A.I.; Koscheev, S.V.; Boronin, A.I. X-ray photoelectron spectroscopy study of Pd oxidation by RF discharge in oxygen. *Appl. Surf. Sci.* **2009**, *255*, 9248–9254. https://doi.org/10.1016/j.apsusc.2009.07.011.
33. Mason, M.G.; Gerenser, L.J.; Lee, S.-T. Electronic Structure of Catalytic Metal Clusters Studied by X-ray Photoemission Spectroscopy. *Phys. Rev. Lett.* **1977**, *39*, 288–291. https://doi.org/10.1103/PhysRevLett.39.288.
34. Thommes, M.; Kaneko, K.; Neimark, A.V.; Olivier, J.P.; Rodriguez-Reinoso, F.; Rouquerol, J.; Sing, K.S.W. Physisorption of gases, with special reference to the evaluation of surface area and pore size distribution (IUPAC Technical Report). *Pure Appl. Chem.* **2015**, *87*, 1051–1069. https://doi.org/10.1515/pac-2014-1117.
35. Kostoglou, N.; Liao, C.W.; Wang, C.Y.; Kondo, J.N.; Tampaxis, C.; Steriotis, T.; Giannakopoulos, K.; Kontos, A.G.; Hinder, S.; Baker, M.; et al. Effect of Pt nanoparticle decoration on the H2 storage performance of plasma-derived nanoporous graphene. *Carbon* **2021**, *171*, 294–305. https://doi.org/10.1016/j.carbon.2020.08.061.

36. Holec, D.; Kostoglou, N.; Tampaxis, C.; Babic, B.; Mitterer, C.; Rebholz, C. Theory-guided metal-decoration of nanoporous carbon for hydrogen storage applications. *Surf. Coat. Technol.* **2018**, *351*, 42–49. https://doi.org/10.1016/j.surfcoat.2018.07.025.
37. Arroyo-Ramírez, L.; Figueroa, Y.; Rodríguez, D.; Otaño, W.; Cabrera, C.R. Palladium Nanostructures Synthesis by Sputtering Deposition on HOPG Surfaces. *ECS Trans.* **2010**, *28*, 1. https://doi.org/10.1149/1.3491767.
38. Pantojas, V.M.; Rodríguez, D.; Morell, G.; Rivera, A.; Ortiz, C.; Santiago-Avilés, J.J.; Otaño, W. Synthesis of palladium with different nanoscale structures by sputtering deposition onto fiber templates. *J. Nanophotonics* **2008**, *2*, 021925. https://doi.org/10.1117/1.3040687.
39. Sitnikova, N.A.; Solovieva, A.O.; Permyakova, E.S.; Sheveyko, A.N.; Shtansky, D.V.; Manakhov, A.M. Silver Ions Incorporation into Nanofibers for Enhanced hMSC Viability. *Chemistry* **2022**, *4*, 931–939. https://doi.org/10.3390/chemistry4030064.
40. Wu, L.; Wu, H.; Wang, X.; Zhong, H.; Wang, Z.; Cai, G.; Jiang, C.; Ren, F. A general method for large-scale fabrication of metal nanoparticles embedded N-doped carbon fiber cloth with highly efficient hydrogen production in all pH range. *Electrochim. Acta* **2020**, *353*, 136475. https://doi.org/10.1016/j.electacta.2020.136475.
41. Mukherjee, S.; Gall, D. Structure zone model for extreme shadowing conditions. *Thin Solid Films* **2013**, *527*, 158–163. https://doi.org/10.1016/j.tsf.2012.11.007.
42. Wang, J.; Huang, H.; Kesapragada, S.V.; Gall, D. Growth of Y-Shaped Nanorods through Physical Vapor Deposition. *Nano Lett.* **2005**, *5*, 2505–2508. https://doi.org/10.1021/nl0518425.
43. Petrov, I.; Barna, P.B.; Hultman, L.; Greene, J.E. Microstructural evolution during film growth. *J. Vac. Sci. Technol. A* **2003**, *21*, S117–S128. https://doi.org/10.1116/1.1601610.
44. Stephenson, A.W.; Baddeley, C.J.; Tikhov, M.S.; Lambert, R.M. Nucleation and growth of catalytically active Pd islands on Au(111)-22 × studied by scanning tunnelling microscopy. *Surf. Sci.* **1998**, *398*, 172–183. https://doi.org/10.1016/S0039-6028(98)80021-6.
45. Bräuer, G.; Szyszka, B.; Vergöhl, M.; Bandorf, R. Magnetron sputtering—Milestones of 30 years. *Vacuum* **2010**, *84*, 1354–1359. https://doi.org/10.1016/j.vacuum.2009.12.014.
46. Ludwig, R.; Kukla, R.; Josephson, E. Vacuum Web Coating—State of the Art and Potential for Electronics. *Proc. IEEE* **2005**, *93*, 1483–1490. https://doi.org/10.1109/JPROC.2005.851489.

8.5 Publication III

In Situ and *Ex Situ* Quantification of Nanoparticle Fluxes in Magnetron Sputter Inert Gas Condensation: A Cu Nanoparticle Case Study

Florian Knabl, Christine Bandl, Thomas Griesser, Christian Mitterer

Journal of Vacuum Science and Technology A, 42(2) (2024) 023201

In Situ and *Ex Situ* Quantification of Nanoparticle Fluxes in Magnetron Sputter Inert Gas Condensation: A Cu Nanoparticle Case Study

Florian Knabl[1], Christine Bandl[2], Thomas Griesser[2], Christian Mitterer[1]

[1] Department of Materials Science, Montanuniversität Leoben, 8700 Leoben, Austria

[2] Department of Polymer Engineering and Science, Montanuniversität Leoben, 8700 Leoben, Austria

Abstract

Magnetron sputter inert gas condensation was coupled with quadrupole mass spectrometry for the *in situ* characterization of a nanoparticle beam. The proposed method allows us to determine the size distribution and the mass flux of the nanoparticles. The measured quadrupole mass spectrometer grid current is converted into a nanoparticle flux and subsequently into a mass flux. Cu nanoparticles were deposited onto Si substrates using different filtering modes of the quadrupole mass spectrometer. Characterization was carried out using a combination of x-ray photoelectron spectroscopy and scanning electron microscopy. Quantitative analysis of the elemental composition of the Si surface revealed a Gaussian distribution of the deposited nanoparticles over the diameter of the rotating substrate holder with a good quantitative agreement with the predictions made from the *in situ* quantification method.

1. Introduction

Nanoparticles (NPs) are defined as particles with dimensions typically ranging from 1 to 100 nm, exhibiting unique properties and behaviors compared to bulk materials.[1] NPs find wide-ranging applications across multiple disciplines. They contribute to the development of composite materials employed for hydrogen storage through surface-based hydrogen adsorption.[2] Environmental applications encompass the utilization of NPs in sensors,[3] water purification,[4] and pollutant remediation.[5] Additionally, nanoparticles enhance the functionality of materials and coatings, e.g. by offering antibacterial/-microbial properties[6,7] and acting as catalysts[8,9] to improve efficiency and selectivity in chemical reactions. For the synthesis of nanoparticles, various methods are employed, including chemical precipitation, sol-gel synthesis, and physical techniques such as laser ablation and magnetron sputter inert gas condensation (MS-IGC).[10,11] Each method offers distinct advantages in terms of particle size control, composition, and scalability.

MS-IGC combines magnetron sputtering, which involves bombarding a target material with ions to release atoms or clusters, with the controlled condensation of these species in an inert gas environment. This method was first reported by Haberland et al.[12] in 1991 and subsequent papers.[13,14] NP nucleation, growth and agglomeration occur within a high pressure aggregation chamber with pressure of a few 10 mbar. Then, the inert gas carries the NPs through an orifice and into a low-pressure expansion zone with a pressure of a few 0.1 mbar. This causes rapid cooling and NP development ceases. NPs leave the aggregation chamber, where the majority of NPs carries a single charge as reported by Popok and Gurevich[15] and by Zamboni et al.[16] While the fraction of neutral particles is typically low for MS-IGC,[12] the fractions of positively and negatively charged particles vary quite significantly depending on the synthesis parameters and the material used.[17–21] NPs synthesized via MS-IGC exhibit a sharp NP size distribution, a defined chemical composition, and in most cases spherical morphology. To further enhance the versatility of the technique, in-flight coating of NPs can be achieved by incorporating a linear magnetron after the expansion zone.[22] MS-IGC is a clean technique when compared to wet chemical methods, as chemical remnants are fully avoided. Various filtering techniques are used to obtain even sharper NP size distributions.

Mass spectrometry, which is often used in combination with MS-IGC, is an analytical technique that measures the mass-to-charge ratio of ions. It involves the ionization of species, generating ions that are subsequently separated based on their mass-to-charge ratio using electric and/or magnetic fields. The separated ions are then detected and analyzed, allowing for the identification and quantification of the components present in the gas phase. Mass spectrometer techniques successfully applied for the characterization and filtering of NP beams include time-of-flight[13,14,23,24] and quadrupole mass spectrometry (QMS).[19,25–29]

Quadrupole mass spectrometers can be used to filter for certain NP masses as well as for determining the overall NP mass distribution depending on the mode of operation. NP sizes can be calculated out of NP masses assuming single-charged NPs of spherical shape and bulk crystal density. NP mass and size are linked explicitly and the two terms may thus be used interchangeably.

The characterization of NP fluxes synthesized by MS-IGC involves several techniques, including but not limited to the following examples: Quartz crystal microbalances[30] are employed to determine the deposition rate, while time-of-flight mass spectrometry and QMS are utilized for mass filtering. Additionally, the fractions of neutral and charged NPs can be analyzed using electrostatic deflection plates,[31] and NP beams can be guided onto the substrate holder using einzel lenses.[27]

As schematically visualized in Fig. 1, we apply a quantitative method for the *in situ* characterization of NP beams synthesized by MS-IGC using QMS. First, a methodology for quantitatively assessing the total NP flux (in NPs/s) and the mass flux (in kg/s) of the NP deposition process was developed. In a subsequent step, the quantitative method was successfully applied within a case study to Cu NPs and confirmed by X-ray photoelectron spectroscopy, enabling to translate the NP flux into a spatial distribution of NPs on the surface. The suggested method enables the determination of the total mass of deposited nanoparticles and allows for the optimization of deposition parameters based on mass flux. This novel approach enables improved process control over nanoparticle deposition by means of magnetron sputter inert gas condensation.

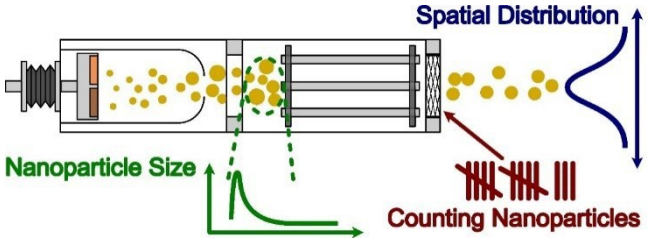

Fig. 1. In situ quadrupole mass spectroscopy is applied for counting NPs and determining their size distribution as synthesized by magnetron sputter inert gas condensation. Ex situ X-ray photoelectron spectroscopy is used to determine the spatial distribution of the deposited NPs.

2. Materials and Methods

A. Magnetron Sputter Inert Gas System

A schematic illustration of the MiniLab 125 deposition system from Moorfield Nanotechnology, and the NL-DX3 nanoparticle deposition source from Nikalyte is presented in Fig. 2. The deposition chamber contains an additional 50.8 mm diameter planar magnetron for thin film deposition (not used in this work) and a rotatable substrate holder. A load-lock chamber allows for rapid sample exchange and features a gate valve and a magnetic manipulator for sample handling.

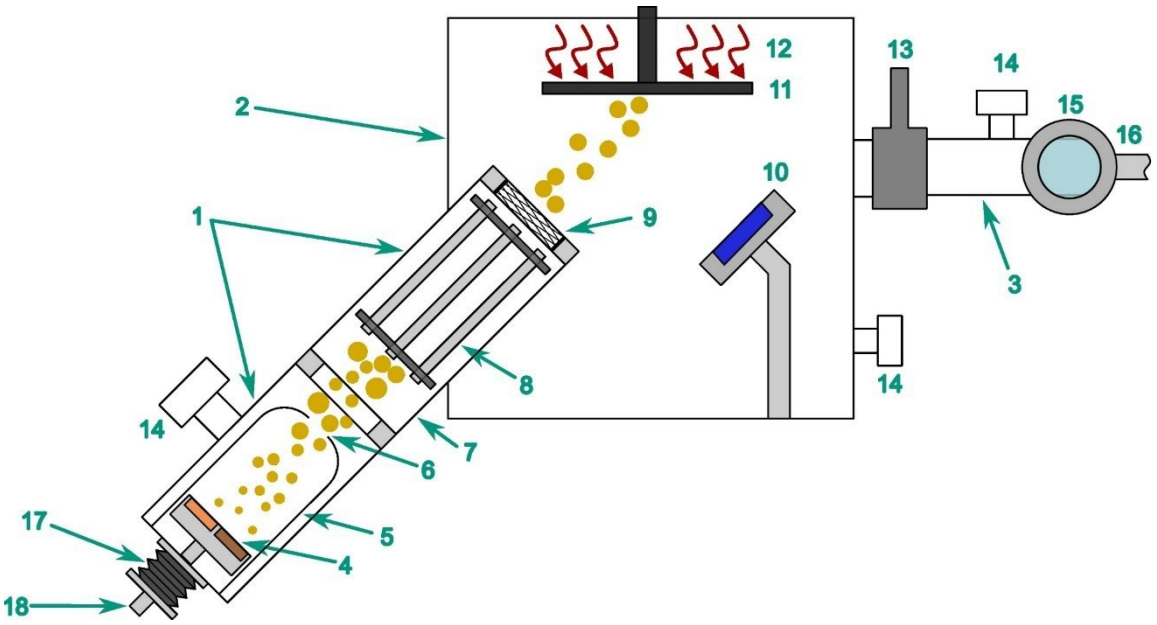

Fig. 2. A schematic of the NP deposition system used within this work consisting of (1) NP source by Nikalyte, (2) deposition chamber, (3) load-lock chamber, (4) three 25.4 mm diameter magnetrons, (5) aggregation chamber terminated by the (6) orifice, (7) expansion zone with the (8) quadrupole mass filter, (9) mesh grid, (10) 50.8 mm diameter magnetron for thin film deposition, (11) substrate holder, (12) heating, (13) gate valve, (14) pumping systems, (15) view port, (16) sample manipulator, (17) linear translator, and (18) feedthroughs for water, gas, and power.

The NP source is mounted to the deposition chamber at an angle of 45°. It consists of a water-cooled aggregation chamber for NP synthesis and a differentially pumped expansion zone for mass filtering. The cylindrical aggregation chamber (diameter 125 mm) contains three water-cooled planar magnetrons with a diameter of 25.4 mm. The targets are connected to separate DC power supply units (3× TDK Genesys GEN600-1.3 DC PSU), enabling independently controlled and simultaneous sputtering. The aggregation chamber terminates in a hemispherical shape containing a flat exchangeable plate with orifice diameters from 2 mm to 5 mm. The aggregation length, defined as the distance between the targets and the

orifice, strongly influences the residence time of the NPs within the aggregation chamber. It can be adjusted simultaneously between 50 mm and 150 mm for the three targets using a linear translator. Ar and He may be introduced in the vicinity of the metal targets using calibrated mass flow controllers. Aggregation length, orifice diameter, gas flow, gas composition, pumping speed, and sputtering power determine the overall pressure and affect both the mean free path and the residence time of the NPs within the aggregation chamber. NPs leave the high-pressure aggregation chamber through the orifice into the low-pressure expansion zone. When leaving the aggregation chamber, most of the NPs carry a single charge and are thus susceptible to electromagnetic manipulation.

The differentially pumped expansion zone contains the NL-QMS quadrupole mass spectrometer by Nikalyte, representing a section with a total length of 300 mm. It contains an assembly of four parallel rods referred to as quadrupole mass filter (QMF). The entrance and opening apertures of the QMF have a diameter of 25 mm. The charged NPs travel through an electric field created by four parallel rods. A DC voltage U is applied to all four rods, and an AC voltage V with a frequency f is applied to each pair of opposing rods, using opposite polarities. The applied electric field affects the NPs traveling through the QMF, allowing only NPs of a certain mass-to-charge ratio to pass through the filter. All other species are ejected from the beam. The quadrupole mass spectrometer can be operated in filter or scan mode. In filter mode, a constant set of U, V, and f is applied to the QMF, resulting in an electric field that allows only NPs of a certain mass to pass through. In scan mode, the QMF continuously iterates through NP masses or NP sizes using a fixed step size, thereby detecting the contributions from different NP sizes. In scan mode, the overall NP flux is the average of the recorded steps. NP detection is performed by measuring the grid current I obtained from a wire mesh grid located after the rod assembly. Each NP is assumed to contribute a single charge. The mesh grid operates with a bias voltage of ±22 V, referred to as “positive” (thus primarily detecting negatively charged NPs) and “negative” (vice versa). The coverage rate of the grid, determined to be roughly 30 % based on photogrammetric analysis of a scale reference photograph using the software ImageJ, implies a ratio of 3:7 for detected to transmitted NPs.

The deposition chamber contains shutters for both the substrate holder and the 50.8-mm-diameter magnetron for thin film deposition. The substrate holder is located ~210 mm from the mesh grid of the NP source and ~145 mm from the 50.8 mm diameter magnetron. The substrate holder can be rotated, heated up to 500 °C, and biased up to +1000 V using a DC power supply (Magna Power SL series 1kW DC). A gas inlet is located in the vicinity of the 50.8 mm diameter magnetron for thin film deposition (powered by a TDK Genesys GEN600-1.3, 800W DC power supply), allowing to introduce up to three different gases (Ar, O_2, N_2)

simultaneously using three independent mass flow controllers. Pressure measurements in the deposition chamber and load lock chamber were performed using wide-range gauges (Edwards WRG-S14.5-36V). A high-resolution temperature-compensated capacitance manometer (Inficon type CDG045D) situated in the deposition chamber allows for accurate pressure measurement within the deposition chamber.

B. Nanoparticle Synthesis

Within this work, Cu NPs were synthesized using a Cu target (Kurt J. Lesker Company Ltd, 99.999 % purity) with 25.8 mm diameter and 3.2 mm thickness. Sputtering was performed using a constant current of 250 mA (roughly 80 W), an aggregation length of 90 mm, an orifice diameter of 3 mm, and a deposition time of 15 min. Ar was introduced into the system via the feedthrough depicted in Fig. 2, maintaining a constant flow rate of 40 sccm. Pressures of 5×10^{-7} mbar and 1.1×10^{-3} mbar were recorded before and during deposition within the deposition chamber, and 4.5×10^{-1} mbar were recorded inside the aggregation chamber during deposition. Single crystal Si (100) substrates with dimensions of roughly 21 mm × 7 mm and a thickness of 325 µm were used. The substrates were ultrasonically cleaned in an isopropanol bath for 10 min and dried using hot air prior to fixing them to the substrate holder, which was rotated at 10 rpm and kept at ground potential throughout the deposition. No additional heating was applied. Under these conditions, the depositions were thus carried out in the soft landing regime with kinetic energies well below 1 eV/atom.[27,32]

The quadrupole mass spectrometer scan mode was used to record the NP size distribution prior to the NP deposition in a NP size range from 1 nm to 20 nm and a step size of 0.1 nm. An AC voltage V of 250 V and a DC voltage U of 2.5 V were used, resulting in a U/V ratio of 0.02. The operational range of the frequency f extends from 500 kHz to 1 Hz. For performing scans, the frequency was swept in a range from 77.54 kHz to 0.87 kHz. For the two samples deposited in filter mode, the filter was set to 2.67×10^6 amu (NP diameter 6.5 nm, frequency 4.68 kHz, see section 3 for details).

NP size distributions were recorded three times in both positive and negative scan mode prior to performing the actual deposition. A self-written Python code was used to average the obtained recordings and for subsequently calculating both the NP flux and the mass flux as a function of the NP mass. The equations used are given in section 3. Mass flux data was smoothed using a Savitzky–Golay filter.

C. Characterization Techniques

Scanning electron microscopy (SEM) micrographs were recorded using a Tescan Clara scanning electron microscope. Before the SEM analysis, all samples underwent plasma cleaning using a Diener electronic Tetra 30 plasma cleaner. The plasma cleaning process

involved an N_2 flow rate of 80 sccm, operating at 10 % power, and a cleaning duration of 20 min. X-ray photoelectron spectroscopy (XPS) measurements were carried out with a Thermo Scientific Nexsa G2 X-ray photoelectron spectrometer system, which employs a monochromatic, micro-focused, low-power Al K□ X-ray (1486.7 eV) source. The X-ray beam was focused to a spot size of 100 µm. XPS spectra were collected using a pass energy of 200.0 eV with a step size of 1.0 eV. Scanning was performed in a rectangular grid with measurements of 7 points along the sample width and a distance of 0.5 mm between points, for which homogenous chemical composition is expected due to the rotational symmetry of the deposition. All measurements were conducted on samples without previous baking or sputter-cleaning.

3. Method Development

Expanding upon the fundamental operation principles of quadrupole mass spectrometry,[33–35] a quadrupole mass filter was used within this work to characterize a beam of charged nanoparticles. This section offers a comprehensive description suitable for those who are not thoroughly familiar with NP deposition. In particular, to facilitate wide-spread use of the suggested methodology, a full description is provided, including equations 3 – 5, which have – despite their apparent simplicity –not been published to the best of the authors' knowledge. The developed methodology may be generalized for other magnetron sputter inert gas condensation sources and various materials.

The motion of charged ions or NPs within the applied electric field is described by the Mathieu equations, which reveal certain stability regions within the space of operating parameters (*U*, *V*, and *f*). These regions allow particles of a certain mass-to-charge ratio to pass through. All other species experience accelerations that grow beyond all limits, resulting in those species being ejected from the NP beam.[36] While the quadrupole field affects the movement of the ions in radial direction, the NPs experience no acceleration along the transverse axis and thus leave the QMF with the same transverse speed, assuming that no further electrostatic potentials are present.

In the context of MS-IGC, it is widely accepted that NPs are predominantly single-charged. A study by Popok and Gurevich demonstrated that, across different deposition parameters, the fraction of single-charged particles never fell below 72 %.[15] If a single charge is assumed, the mass filtered by the QMF for a *U/V* ratio of 0.16784 (located at the edge of a region of stability[36]) can be calculated as

$$m = \frac{V}{7.219\, f^2\, r_0^2}\,, \qquad (1)$$

where *m* is the NP mass in amu, *V* is the AC voltage in V, *f* is the AC frequency in MHz, and r_0 is the inner distance from the center of the QMF to the outer rods in cm.[35] It has to be noted that in literature various equations are provided, using different pre-factors and in some cases not mentioning the units used for calculation. Operating the QMF can be described using the equation

$$m = 6.77409 \cdot 10^4 \cdot \frac{V}{f^2}, \quad (2)$$

empirically determined from different sets of *U*, *V*, and *f*. It uses the same units as in equation (1). It is important to highlight that the *U*/*V* ratio has a significant impact on the mass resolution.[37] Maintaining a constant *U*/*V* ratio ensures a consistent mass resolution for all detected species. The NP flux *j* can now be calculated using

$$j = \frac{I}{e}, \quad (3)$$

where *e* is the elementary charge (as each NP contributes a single Coulomb to the grid current), and *I* is the current measured at the wire mesh grid. The mass flux $\dot{m}$ for a given NP mass can be calculated using

$$\dot{m} = j \cdot m = \frac{I}{e} \cdot m, \quad (4)$$

as the mass of the NP *m* is known due to the choice of the parameters *U*, *V*, and *f*. In a final step the total deposited mass M_{total} can be calculated using

$$M_{total} = \dot{m} \cdot t = j \cdot m \cdot t = \frac{I}{e} \cdot m \cdot t, \quad (5)$$

where *t* is the deposition time. This equation can be used to calculate the mass flux contribution for each fraction of NP mass. Equations (3)–(5) account for the situation at the grid itself. For establishing the corresponding values of the NP beam leaving the quadrupole mass spectrometer, the given values must account for the coverage rate of the grid. For the particular setup presented within this work, all values would need to be multiplied by a constant factor of 7:3.

An example for Cu NPs synthesized by the MS-IGC process used in this work is given in Fig. 3. The peak of the grid current curve corresponds to the most commonly synthesized fraction of NPs for the given set of conditions. The mass flux curve is calculated by equation (4). The peak of this curve corresponds to the NP fraction contributing the largest fraction of mass flux. As a result of equation (4), the peak is shifted to higher NP masses compared to the curve determined by measuring the QMS grid current. Detected grid currents are in the range of nA, calculated NP fluxes are in the range of 10^9 NP/s, and the mass flux is in the range of ng/s.

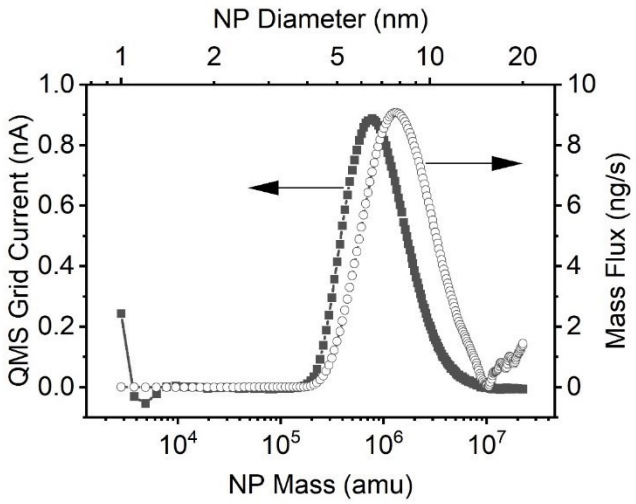

Fig. 3. In situ QMS data and calculated mass flux ratios for Cu NPs deposited using an Ar flux of 40 sccm, an aggregation length of 90 mm, and a constant magnetron sputter current of 250 mA. The tail in the mass flux curve for masses beyond 10^7 amu is an artifact caused by minimal grid currents multiplied by large NP mass values. This artifact can be discarded.

3. Results and Discussion

A. In Situ Quadrupole Mass Spectrometry

Our developed methodology was applied to Cu NPs deposited onto Si substrates using four distinct operational modes of the mass filter: positive and negative scan modes, as well as positive and negative filter modes. To characterize the NPs synthesized via MS-IGC, we employed the QMF to capture the NP size distribution. In Fig. 4a, we present the NP size distribution at the start of the deposition, while Fig. 4c illustrates the distribution at the end of the process. The evolution of the grid current over the deposition time is detailed in Fig. 4b. For scan mode, the grid current was averaged over the steps, whereas in filter mode, we recorded it at the specific filter setting.

For mass flux calculations, we applied Eq. 4 to estimate the mass fluxes at both the start and the end of the deposition process. These values are shown in Fig. 4d and 4f, respectively. Fig. 4e tracks the evolution of mass flux during the deposition time. In scan mode, the mass flux was calculated as the mean value of the corresponding mass flux values from the individual scan steps, while in filter mode, the mass flux was derived directly from the grid current value set by the filter.

The recorded NP size distributions in Fig. 4a and 4c revealed a log-normal distribution of NP sizes when the QMF was operated using a negative grid bias. Log-normal distributions are commonly reported in literature for NPs synthesized by MS-IGC.[14,17,38,39] The positive grid

current curves showed a bimodal log-normal distribution of NP sizes, occasionally observed in the synthesis of different monometallic NPs through MS-IGC.[40,41] The most common NP size shifted from a small diameter (~3 nm or 8 × 10^4 amu) to a larger diameter (~5.5 nm or 4 × 10^5 amu) over the course of the deposition. The peak of the negative grid current curves in Fig. 4a was detected at a NP diameter of 6.5 nm. This was used as the filter setting for both positive and negative filter mode depositions, as there was a significant NP flux for both modes.

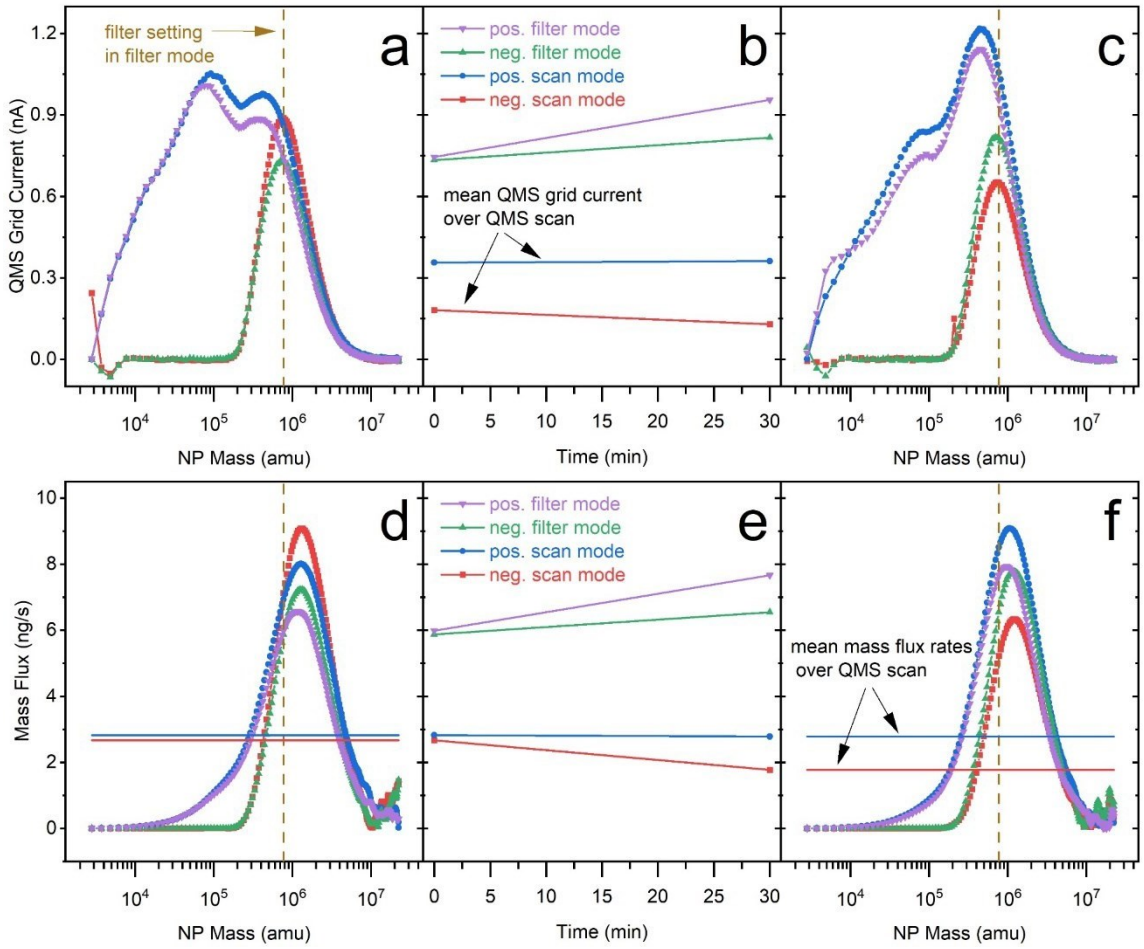

Fig. 4. In situ QMS grid current (a-c) and mass flux data (d-e) for different samples using identical deposition parameters (sputtering current of 250 mA, Ar flow of 40 sccm, aggregation length of 90 mm). Graphs (a) and (d) show the recorded nanoparticle distributions at the start of the deposition. Graphs (b) and (e) show the development over the deposition time of 30 min. Graphs (c) and (f) show the recorded nanoparticle distributions at the end of the deposition. Please note that for filter mode the actual distribution of deposited NPs is much sharper due to filtering. The total mass flux in filter mode was determined by the mass flux at the set filter position, while the total mass flux in scan mode was calculated by averaging over all data points. As it is the case in Fig. 3, the tail in mass flux above 10^7 amu is an artifact caused by close-to-zero grid current data.

Applying a positive bias to the mesh grid yields a stronger grid current (see Fig. 4a and 4c), indicating a larger fraction of negatively charged NPs. Furthermore, a significant number of small (< 4 nm), negatively charged NPs was detected using a positive grid bias. In comparison, there were no small positively charged NPs present, as concluded from the lack of a detectable grid current for the negative grid bias measurements.

All mass flux curves (Fig. 4d, Fig. 4f) followed a log-normal distribution with the peak shifted to larger NP masses compared to the QMS grid current curves. However, the presence of small (< 4 nm) NPs introduced a deviation from the log-normal distribution when a positive grid bias was applied. The blue and red horizontal lines represent the time-averaged mass flux for depositions carried out in the positive and negative scan modes, respectively. These mass fluxes were calculated as the averages of the individual scan steps. At the beginning of the deposition, the positive scan mode exhibited a slightly higher overall mass flux, despite having a lower peak grid current. This was attributed to a broader distribution. As the deposition progressed, this distinction became even more pronounced.

Fig. 4b and 4e reveal the trend of deposited NPs over the deposition time. We found a minor decrease and a stable NP output in case of the negative and positive scan mode deposition, while an increase was recorded in both filter modes.

A decrease in deposition rate for various NP materials synthesized by MS-IGC is extensively covered in literature[21,26,29,42,43] and attributed to both a gradual decrease of oxygen impurities[21] in the aggregation zone, as well as on target race track formation[43] over its lifetime. The decrease is commonly remedied by introducing small quantities of oxygen to the inert gas. Adding oxygen to the NP beam adds uncertainty to the characterization step. Assuming that oxidation stops after the NPs leave the aggregation chamber, the mass would be determined accurately by the QMF. The crystal density would be unknown, however, as the copper oxides have different crystal densities compared to the bulk phase (6.0 g/cm³ for Cu_2O, compared to 9.0 g/cm³ for Cu), and the extent of oxidation is not known. Consequently, the NP diameter could only be estimated with larger uncertainties. Furthermore, there is uncertainty about the time of oxidation, i.e. does this process continue after the NPs passed the QMF? All these effects considered, the introduction of oxygen was not investigated any further within this work. A shift in the NP size distribution towards larger NP sizes was reported in literature for Cu targets.[43] When depositions are carried out in filter mode, the total mass of deposited NPs is assumed to be proportional to the mass flux value of the filtered NP mass. In scan mode, the total mass of deposited NPs is assumed to be proportional to the average of the individual mass flux values for each scan step.

B. Ex Situ Characterization

The SEM micrograph in Fig. 5 shows the Cu NPs deposited on the Si substrate after depositing in positive filter mode. The micrograph indicates a surface coverage clearly below a single layer of NPs. This is in good agreement with the peak Cu content of ~5 at% determined via XPS, as shown later. It is important to note that while SEM micrographs serve to visualize the deposited NPs, they are limited in their capacity for precise quantification. To obtain comprehensive data regarding NP size distribution with the meaningful statistical significance, more sophisticated techniques such as transmission electron microscopy and small-angle X-ray scattering would be required.

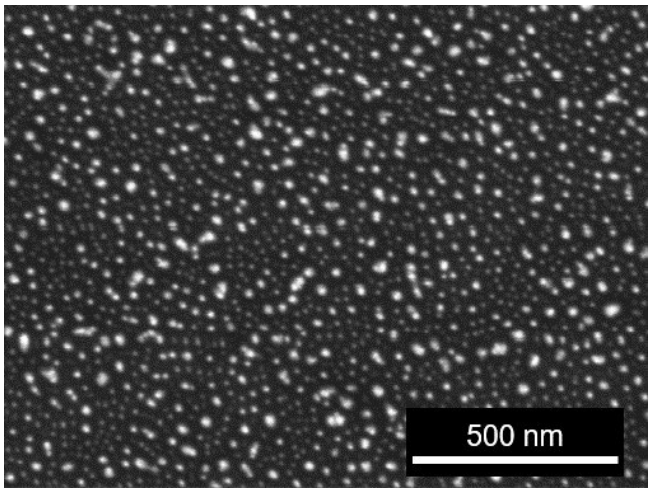

Fig. 5. SEM micrograph of NPs deposited in positive filter mode. Note that several NPs formed larger agglomerates.

XPS measurements were conducted to verify the correlation between the detected NP flux and the quantities of NPs found on the substrate. XPS is used to assess the homogeneity and spatial distribution of deposited Cu NPs, as SEM showed submonolayer coverage of NPs. Given the information depth of a few nm, XPS allows to probe the volume of deposited NPs, which correlates with the deposited Cu NPs' mass — data not readily obtained through alternative methods like energy-dispersive X-ray spectroscopy. The radial symmetry of the spatial distribution of NPs deposited using the rotating substrate holder was confirmed, with a maximum Cu content recorded at ~2 mm from the center of the substrate holder. To simplify the analysis, we recorded data from one side of the symmetric distribution, excluding data points within 2 mm of the deposition center. Subsequent samples were prepared under identical sputter parameters but with different QMF deposition modes. Fig. 6a displays Cu content as a function of the deposition radius, showing the highest content for the positive filter mode, approximately ~5 at% Cu. The error bars in Fig. 6a represent the standard deviation calculated from the seven measured data points at each radial position.

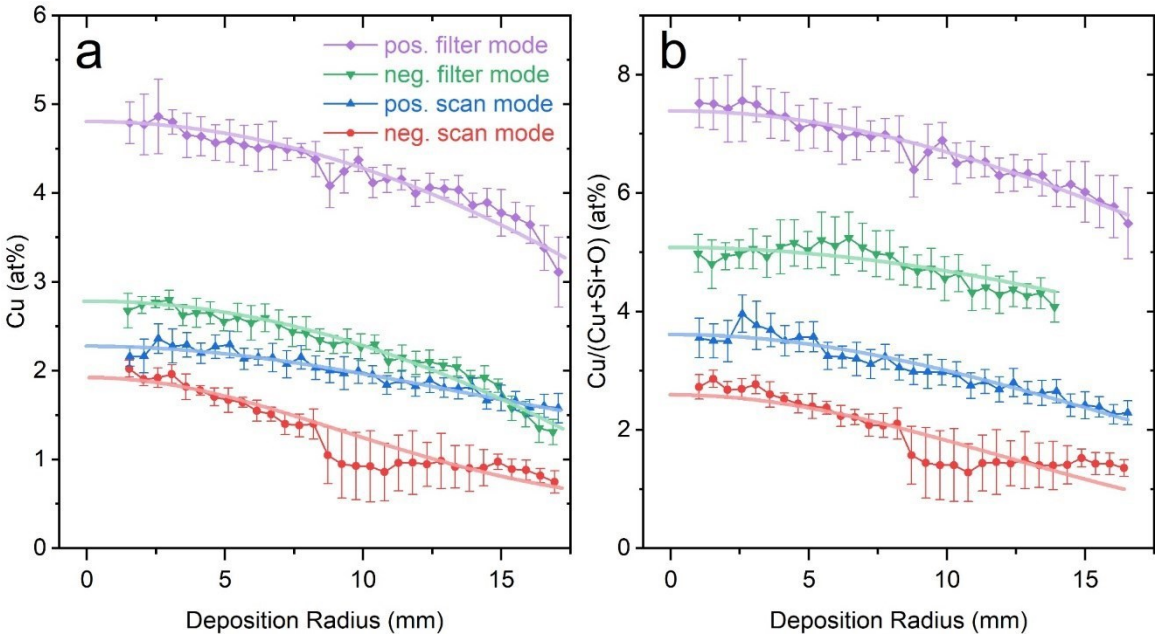

Fig. 6. Chemical composition of the sample surface determined by XPS as a function of deposition radius from the center of the substrate holder, using the atomic concentration of Cu (a) and the atomic ratio Cu/(Cu+Si+O) (b) as the relevant key parameter. Gaussian functions were fitted through the data as indicated by the continuous light-colored lines. Error bars represent standard deviations in (a) and maximum errors based on the standard deviations of the three elements in (b).

Cu, Si, O, and C were identified on the surface via XPS analysis. The determined Si:O ratio was remarkably constant throughout all samples, suggesting that characterizing oxidized NPs is sufficient. Comprehensive investigations on the oxidation dynamics of Cu NPs were already conducted elsewhere.[16,44] The samples showed a significant variation in carbon content across the surface, typically falling in the range of 30 – 40 at%. Higher C content was observed at the outer edges of the samples. This is attributed to sample handling via tweezers, both during the cleaning process prior to deposition as well as during sample transfer from the deposition system to the XPS system, as adventitious carbon can only be avoided via *in situ* XPS measurements.[45]

Based on the XPS results, we propose that the Cu content alone is less meaningful for assessing the spatial distribution of NPs. Since C can be discarded here, the atomic ratio Cu/(Cu+Si+O) was calculated and is depicted in Fig. 6b. Error bars were determined using a maximum error approach, employing the standard deviations of Cu, Si, and O atomic concentrations as maximum error values.

The Cu/(Cu+Si+O) ratio reveals distinct similarities between the predicted NP output (Fig. 4e) and the spatial distribution of NPs on the substrate. The spatial distribution of the deposited NPs was described using a Gaussian distribution, as reported in the literature.[17,30]

Positive and negative filter modes showed a wider NP distribution, with standard deviations of 25 mm and 22 mm, while the standard deviations for positive and negative scan modes were significantly smaller with 16 mm and 12 mm, as seen in Fig. 6b, with all calculated standard deviations having large uncertainties. It can be speculated that the width of the NP beam was influenced by the operational modes of the QMF, resulting in two distinctively different beam widths for the scan and the filter mode. Furthermore, it can be speculated that the integrated area over the fitted Gaussian distribution of the Cu/(Cu+Si+O) parameter plotted in Fig. 6b might be used as a proxy parameter to assess to overall deposited NP sample mass. As XPS is highly surface-sensitive, this approach can only be valid for small NPs (to ensure probing the whole NP volume) and a low NP density (clearly below a single layer of NPs). We would like to highlight that the proposed method based on QMS is capable of performing this task *in situ*, thus allowing to make more accurate predictions of total NP output, which is not possible for other methods such as the established quartz crystal microbalances.[30] This could be useful for the dynamic experimental conditions present within MS-IGC requiring real-time data.

An additional sample was prepared with the positive filter mode set to 1.63×10^7 amu, corresponding to a NP diameter of 18 nm, as there was a close-to-zero grid current (see Fig. 4a) under the given sputtering conditions. Both XPS measurements and SEM investigations did not detect any Cu NPs, thus confirming that filtering works and that the tail in the mass flux curve (see Fig. 4b) is an artifact. It has to be noted that a minor quantity of NPs is expected to be neutral and thus unaffected by the QMF – despite the zero grid current. As the reference samples in positive filter mode yielded a peak Cu content of 5 at%, and traces below 0.5 at% cannot be detected with reasonable accuracy by XPS, we conclude that the fraction of neutral NPs must be below 10 % for the particular deposition settings used within this work. However, additional SEM investigations failed to find any evidence of NPs present, thus implying that virtually all NPs leaving the aggregation chamber are charged. Kashtanov reported roughly 40 % of neutral Ti NPs,[19] Polonskyi et al. reported even larger fractions of neutral Ag NPs for a given set of deposition conditions.[31] To the best of the authors' knowledge, there is no report of neutral Cu NP fractions for MS-IGC found in the literature.

Despite these uncertainties, comparing the data in Fig. 4e and Fig. 6b we conclude that a reasonable qualitative agreement between predicted and experimentally determined NP quantity was obtained. This confirms that the quantitative *in situ* assessment of the NP beam proposed in this work can serve as a tool to estimate size and quantity of NPs deposited.

4. Conclusions

Within this work, a convenient methodology for the quantitative *in situ* assessment of a beam of Cu nanoparticles synthesized by magnetron sputter inert gas condensation was applied. Based on the operating principle of a quadrupole mass spectrometer, the detected grid current was used for characterizing the nanoparticle size distribution obtained for the applied sputter conditions. Furthermore, the methodology allows to assess the total quantity of the deposited nanoparticles. X-ray photoelectron spectroscopy was employed to verify the quantity of Cu nanoparticles deposited onto Si substrates with further confirmation obtained by scanning electron microscopy. The spatial distribution of the deposited nanoparticles follows a Gaussian shape with standard deviations in the range of 12 to 25 mm depending on the operational mode of the quadrupole mass filter. Further investigations confirmed that filtering for nanoparticles with a size that was not actually produced within the aggregation chamber effectively blocks the transfer of all nanoparticles, thus implying that virtually all nanoparticles leaving the aggregation chamber are charged. The developed method enables future researchers to deposit nanoparticles of various materials in both the desired size and quantity.

Acknowledgements

The authors acknowledge helpful discussions with Nikolaos Kostoglou (Montanuniversität Leoben) and Ludvik Martinu (Polytechnique Montréal, Canada). Furthermore, the authors are grateful to Michael Tkadletz (Montanuniversität Leoben) for scanning electron microscopy investigations.

References

[1] S. Foss Hansen, B.H. Larsen, S.I. Olsen, and A. Baun, Nanotoxicology **1**, 243 (2007).

[2] N. Kostoglou, C.W. Liao, C.Y. Wang, J.N. Kondo, C. Tampaxis, T. Steriotis, K. Giannakopoulos, A.G. Kontos, S. Hinder, M. Baker, E. Bousser, A. Matthews, C. Rebholz, and C. Mitterer, Carbon **171**, 294 (2021).

[3] R.K. Joshi, S. Krishnan, M. Yoshimura, and A. Kumar, Nanoscale Res. Lett. **4**, 1191 (2009).

[4] T. Pradeep and Anshup, Thin Solid Films **517**, 6441 (2009).

[5] G.N. Hlongwane, P.T. Sekoai, M. Meyyappan, and K. Moothi, Sci. Total Environ. **656**, 808 (2019).

[6] A. Kuzminova, J. Beranová, O. Polonskyi, A. Shelemin, O. Kylián, A. Choukourov, D. Slavínská, and H. Biederman, Surf. Coat. Technol. **294**, 225 (2016).

[7] S. Kumar, J. Kratochvíl, Y. Al-Muhkhrabi, E. Kratochvílová, D. Kahoun, D. Kaftan, J. Hanuš, J. Štěrba, and V. Straňák, Surf. Interfaces **30**, 101818 (2022).

[8] P. Felfer, P. Benndorf, A. Masters, T. Maschmeyer, and J.M. Cairney, Angew. Chemie Int. Ed. **53**, 11190 (2014).

[9] Y. Zhou, C. Jin, Y. Li, and W. Shen, Nano Today **20**, 101 (2018).

[10] P.G. Jamkhande, N.W. Ghule, A.H. Bamer, and M.G. Kalaskar, J. Drug Deliv. Sci. Technol. **53**, 101174 (2019).

[11] Y. Huttel, Gas-Phase Synthesis of Nanoparticles (John Wiley & Sons, Weinheim, Germany, 2017).

[12] H. Haberland, M. Karrais, and M. Mall, Zeitschrift Für Phys. D Atoms, Mol. Clust. **20**, 413 (1991).

[13] H. Haberland, M. Karrais, M. Mall, and Y. Thurner, J. Vac. Sci. Technol. A **10**, 3266 (1992).

[14] H. Haberland, M. Mall, M. Moseler, Y. Qiang, T. Reiners, and Y. Thurner, J. Vac. Sci. Technol. A **12**, 2925 (1994).

[15] V.N. Popok and L. Gurevich, J. Nanoparticle Res. **21**, 171 (2019).

[16] F. Zamboni, A. Makarevičiūtė, and V.N. Popok, Appl. Nano **3**, 102 (2022).

[17] L. Martínez, K. Lauwaet, G. Santoro, J.M. Sobrado, R.J. Peláez, V.J. Herrero, I. Tanarro, G.J. Ellis, J. Cernicharo, C. Joblin, Y. Huttel, and J.A. Martín-Gago, Sci. Rep. **8**, 7250 (2018).

[18] J. Blažek, J. Kousal, H. Biederman, O. Kylián, J. Hanuš, and D. Slavínská, J. Phys. D. Appl. Phys. **48**, 415202 (2015).

[19] P. V Kashtanov, B.M. Smirnov, and R. Hippler, Physics-Uspekhi **50**, 455 (2007).

[20] B.M. Smirnov, I. Shyjumon, and R. Hippler, Phys. Rev. E **75**, 66402 (2007).

[21] O. Polonskyi, O. Kylián, M. Drábik, J. Kousal, P. Solař, A. Artemenko, J. Čechvala, A. Choukourov, D. Slavínská, and H. Biederman, J. Mater. Sci. **49**, 3352 (2014).

[22] J. Hanuš, M. Vaidulych, O. Kylián, A. Choukourov, J. Kousal, I. Khalakhan, M. Cieslar, P. Solař, and H. Biederman, J. Phys. D. Appl. Phys. **50**, 475307 (2017).

[23] S. Pratontep, S.J. Carroll, C. Xirouchaki, M. Streun, and R.E. Palmer, Rev. Sci. Instrum. **76**, 45103 (2005).

[24] S.R. Plant, L. Cao, and R.E. Palmer, J. Am. Chem. Soc. **136**, 7559 (2014).

[25] M. Gracia-Pinilla, E. Martínez, G.S. Vidaurri, and E. Pérez-Tijerina, Nanoscale Res. Lett. **5**, 180 (2009).

[26] A. Marek, J. Valter, S. Kadlec, and J. Vyskočil, Surf. Coat. Technol. **205**, S573 (2011).

[27] G.E. Johnson, R. Colby, and J. Laskin, Nanoscale **7**, 3491 (2015).

[28] M. Ganeva, T. Peter, S. Bornholdt, H. Kersten, T. Strunskus, V. Zaporojtchenko, F. Faupel, and R. Hippler, Contrib. to Plasma Phys. **52**, 881 (2012).

[29] W. Chamorro-Coral, A. Caillard, P. Brault, P. Andreazza, C. Coutanceau, and S. Baranton, Plasma Process. Polym. **16**, e1900006 (2019).

[30] Batková, T. Kozák, S. Haviar, P. Mareš, and J. Čapek, Surf. Coat. Technol. **417**, 127196 (2021).

[31] O. Polonskyi, P. Solař, O. Kylián, M. Drábik, A. Artemenko, J. Kousal, J. Hanuš, J. Pešička, I. Matolínová, E. Kolíbalová, D. Slavínská, and H. Biederman, Thin Solid Films **520**, 4155 (2012).

[32] V.N. Popok, I. Barke, E.E.B. Campbell, and K.H. Meiwes-Broer, Surf. Sci. Rep. **66**, 347 (2011).

[33] W. Paul and H. Steinwedel, Zeitschrift Für Naturforsch. A **8**, 448 (1953).

[34] W. Paul and M. Raether, Zeitschrift Für Phys. **140**, 262 (1955).

[35] W. Paul, H.P. Reinhard, and U. von Zahn, Zeitschrift Für Phys. **152**, 143 (1958).

[36] P.H. Dawson, Quadrupole Mass Spectrometry and Its Applications (Elsevier, Amsterdam, 2013).

[37] P. Labastie and M. Doy, Int. J. Mass Spectrom. Ion Process. **91**, 105 (1989).

[38] J. Drewes, S. Rehders, T. Strunskus, H. Kersten, F. Faupel, and A. Vahl, Part. Part. Syst. Charact. **39**, 2200112 (2022).

[39] C. Xirouchaki and R.E. Palmer, Philos. Trans. R. Soc. London. Ser. A Math. Phys. Eng. Sci. **362**, 117 (2004).

[40] P. Solař, O. Polonskyi, A. Olbricht, A. Hinz, A. Shelemin, O. Kylián, A. Choukourov, F. Faupel, and H. Biederman, Sci. Rep. **7**, 1 (2017).

[41] J. Vernieres, S. Steinhauer, J. Zhao, A. Chapelle, P. Menini, N. Dufour, R.E. Diaz, K. Nordlund, F. Djurabekova, P. Grammatikopoulos, and M. Sowwan, Adv. Funct. Mater. **27**, 1605328 (2017).

[42] A. Kusior, K. Kollbek, K. Kowalski, M. Borysiewicz, T. Wojciechowski, A. Adamczyk, A. Trenczek-Zajac, M. Radecka, and K. Zakrzewska, Appl. Surf. Sci. **380**, 193 (2016).

[43] M. Ganeva, A. V. Pipa, and R. Hippler, Surf. Coat. Technol. **213**, 41 (2012).

[44] V.N. Popok, S.M. Novikov, Y.Y. Lebedinskij, A.M. Markeev, A.A. Andreev, I.N. Trunkin, A. V Arsenin, and V.S. Volkov, Plasmonics **16**, 333 (2021).

[45] G. Greczynski and L. Hultman, Vacuum **205**, 111463 (2022).

8.6 Publication IV

Enhancement of Copper Nanoparticle Yield in Magnetron Sputter Inert Gas Condensation by Applying Substrate Bias Voltage and its Influence on Thin Film Morphology

Florian Knabl, Dominik Gutnik, Prathamesh Patil, Christine Bandl, Tijmen Vermeij, Christian M. Pichler, Barbara Putz, Christian Mitterer

Submitted for publication

Enhancement of Copper Nanoparticle Yield in Magnetron Sputter Inert Gas Condensation by Applying Substrate Bias Voltage and its Influence on Thin Film Morphology

Florian Knabl[1], Dominik Gutnik[1,2], Prathamesh Patil[3], Christine Bandl[4], Tijmen Vermeij[2], Christian M. Pichler[3,5], Barbara Putz[1,2], Christian Mitterer[1]

[1] Department of Materials Science, Montanuniversität Leoben, 8700 Leoben, Austria

[2] Empa, Swiss Federal Laboratories for Materials Science and Technology, 3602 Thun, Switzerland

[3] CEST Centre for Electrochemistry and Surface Technology GmbH, 2700 Wiener Neustadt, Austria

[4] Department of Polymer Engineering and Science, Montanuniversität Leoben, 8700 Leoben, Austria

[5] Institute of Applied Physics, TU Wien, 1040 Wien, Austria

Keywords: magnetron sputter inert gas condensation; nanoparticle synthesis; low energy ion scattering spectroscopy; thin film; magnetron sputtering;

Abstract

Large-scale synthesis of high-purity nanoparticles is an intense topic of scientific research, with magnetron sputter inert gas condensation recognized as a promising, environmentally friendly technique avoiding wet chemical processes. This study explores the deposition of size-selected nanoparticles under varied substrate bias voltages and reports on a consequent increase in deposition rates up to 32 %. These alterations in substrate bias voltage induce a progressive change in the morphology of the resulting nanoparticle thin films, attributable to the increased kinetic energy of the nanoparticles. Comprehensive characterization via quadrupole mass spectroscopy of the nanoparticle flux, scanning electron microscopy, X-ray photoelectron spectroscopy, and low-energy ion scattering spectroscopy of the deposited nanoparticles corroborates the enhanced nanoparticle yield associated with increased substrate bias voltage. These findings signify a methodological advancement, enhancing the efficiency of magnetron sputter inert gas condensation and moving the technology a step further towards feasible industrial production.

1. Introduction

The exploration of nanoparticles (NPs) has become an integral part of materials science, with practical applications ranging from catalysis[1], photocatalysis[2], hydrogen sensing[3], hydrogen storage,[4] functionalized textiles for oil-water separation[5] to antibacterial[6] and antiviral[7] surfaces. Such applications are possible as NPs exhibit distinct physical and chemical properties, which can significantly differ from their bulk counterparts due to their small size and thus high surface-to-volume ratio. This has led to an increased research focus on the controlled synthesis and characterization of NPs to better understand their synthesis-structure-property behavior.

Magnetron sputter inert gas condensation (MS-IGC) is a physical vapor deposition technique for NP synthesis, offering a pathway to generate high-purity particles via a dry process. Initially presented by Haberland et al. in 1991,[8] it combines NP formation by inert gas condensation with enhanced deposition rates achieved by magnetron sputtering. The process commences with the sputtering of atoms from a target material within an aggregation chamber, typically maintained at a pressure between 10 to 100 Pa. Still in the vapor phase, these atoms then undergo condensation, beginning with the formation of diatomic clusters through a three-body collision step involving an inert gas, often argon. As these nascent clusters migrate through the aggregation chamber, they accumulate additional atoms, leading to progressive growth. Upon entering a differentially pumped high-vacuum chamber, the growth of these NPs is considered to stop and a beam of NPs with a sharp size distribution is obtained. The NPs comprise a mixture of positively charged, negatively charged, and neutral particles, with their individual fractions being according to literature largely different.[9–11] The dominant NP fraction carries a single charge,[12] making them susceptible to electrostatic manipulation. For instance, insertion of a biased grid enables to measure an electrical current, which allows to determine the NP flux *in situ*.[13] For the Cu NPs addressed in this work, we know from an earlier study that the predominant contributions originate from negatively charged nanoparticles.[13] This allows the selection of NPs based on their mass-to-charge ratio, utilizing either time-of-flight or quadrupole mass spectrometry (QMS). Specifically, a quadrupole mass filter can be employed to isolate NPs of a desired mass — and by inference, assuming a known crystal density and spherical geometry, a specific size — resulting in a refined size distribution. At the time of writing, MS-IGC did not yet achieve a commercial breakthrough and a subsequent large-scale application in industry, in particular due to a still insufficient deposition rate.[14]

Advancements in the MS-IGC technique have focused on enhancing the efficiency and stability of NP synthesis. Notably, the introduction of trace amounts of reactive gases such as O_2,[15] H_2/CH_4,[16] and water vapor[14] into the inert gas stream has shown promise in increasing

the yield and process stability. From an engineering point of view, the development of a full-face erosion magnetron[14] aims to optimize target material utilization, addressing the prevalent issue of a decreasing deposition rate associated with race track formation during sputtering[17] and optimization of the gas flow within the aggregation chamber through computational fluid dynamics models can reduce nanoparticle losses to chamber walls.[18] Separately, in his early work MS-IGC pioneer Haberland already applied a substrate bias voltage to accelerate metallic NPs towards the substrate.[8,19] This was later-on studied by various authors, reporting smoothening or roughening phenomena of initially rough or smooth surfaces, respectively,[20] flattening of individual nanoparticles with increasing bias voltage[21] or the formation of thin film structures with varying degrees of porosity[22]. These works identify three principal deposition regimes for nanoparticles, namely soft landing, pinning, and implantation, which are distinguished by their respective kinetic energy per atom.[23] However, none of the authors discussed if applying a substrate bias voltage could increase the NP deposition rate and thus the efficiency of the process.

In this study we demonstrate for the first time how the application of a substrate bias voltage enhances the extraction of NPs up to 32 % from a source operating with the MS-IGC principle, by monitoring both the *in situ* QMS signal of the entire nanoparticle flux and the amount and morphology of nanoparticles arriving on the substrate, as visualized in Figure 1.

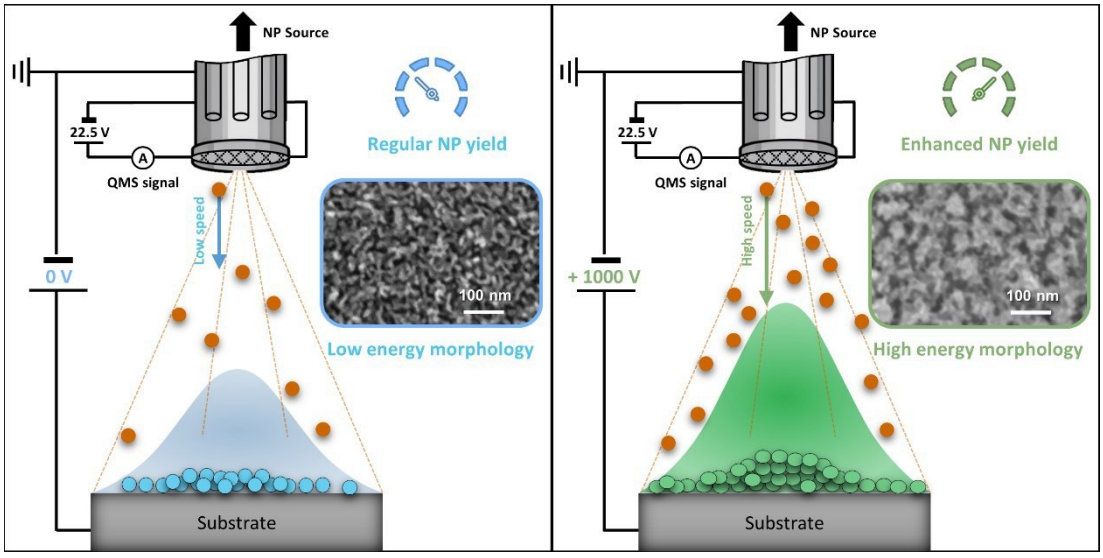

Figure 1. *Synthesis schematic of Cu nanoparticles using the magnetron sputter inert gas condensation (MS-IGC) principle; substrate bias voltages between 0 and 1000 V are used in this work. When the substrate bias is applied, we detect an increase in the NP flux (expressed by an increase in the QMS signal), enhancing the NP yield of the fabrication process. The additional kinetic energies of impinging NPs markedly influence the NP-surface interaction and resulting thin film morphology.*

Two different NP sizes, namely 8 nm and 1.8 nm, are studied in detail, to investigate the influence of particle energy and landing condition. The morphology of the resulting NP thin films is characterized by scanning electron microscopy (SEM), as well as X-ray photoelectron (XPS) and low-energy ion scattering spectroscopy (LEIS). Our findings indicate that applying a substrate bias voltage does allow to extract an increased quantity of NPs out of the NP source, while simultaneously affecting the morphology of the thin film formed by NP deposition.

2. Results & Discussion

2.1. Nanoparticle synthesis

As shown in Figure 2, an increase in the positive bias voltage (300 V and 1000 V) applied to the substrate during NP deposition causes a corresponding rise in the QMS grid current, which serves as an indicator of the NP flux within the system[13] and thus implies an increase in extracted NPs. This effect was consistently evident across the overall NP size distribution, as demonstrated in Figure 2a, as well as in the QMS grid current signal obtained when monitoring a specifically filtered NP size during deposition, as shown in Figure 2b.

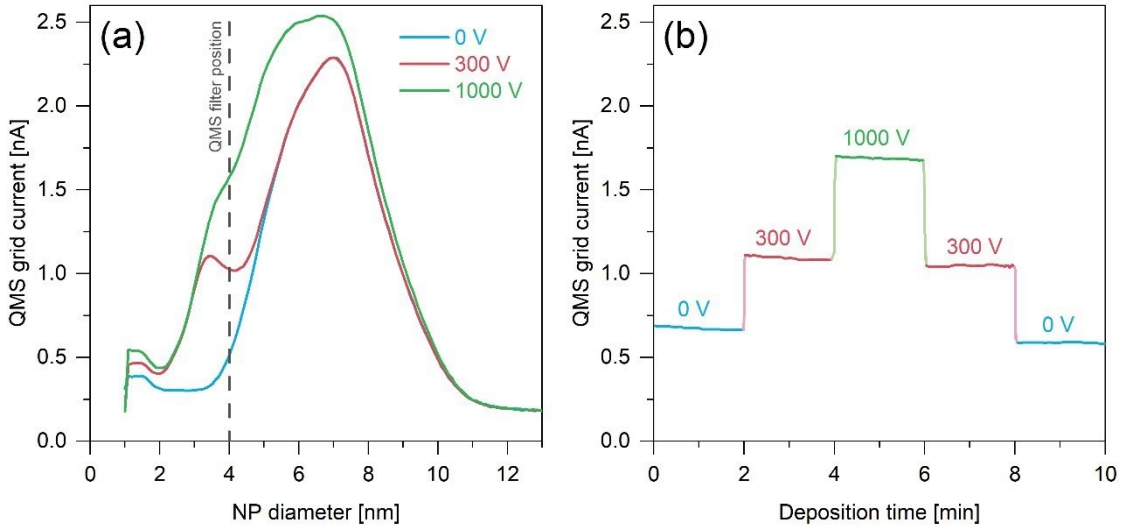

Figure 2. *In situ QMS data revealing an apparent increase in NP flux with applied substrate bias voltage. This increase is visible in the (a) NP size distribution as determined by the QMS and the (b) time-resolved QMS grid current for a selected NP size (e.g. 4 nm, filter position indicated in a) by dashed line in (a)), with increases corresponding to the application of 300 V and 1000 V bias voltage, illustrating the reversible nature of the substrate bias voltage effect on the NP flux.*

Substrate bias variation to enhance the NP yield was performed for two different nanoparticle sizes: 8 nm and 1.8 nm diameter. Figure 3a shows representative NP size

distributions, measured before and after deposition (dark/lighter shade, respectively, 0 V bias), which exhibit either a Gaussian or a bimodal Gaussian shape, depending on the deposition parameters.

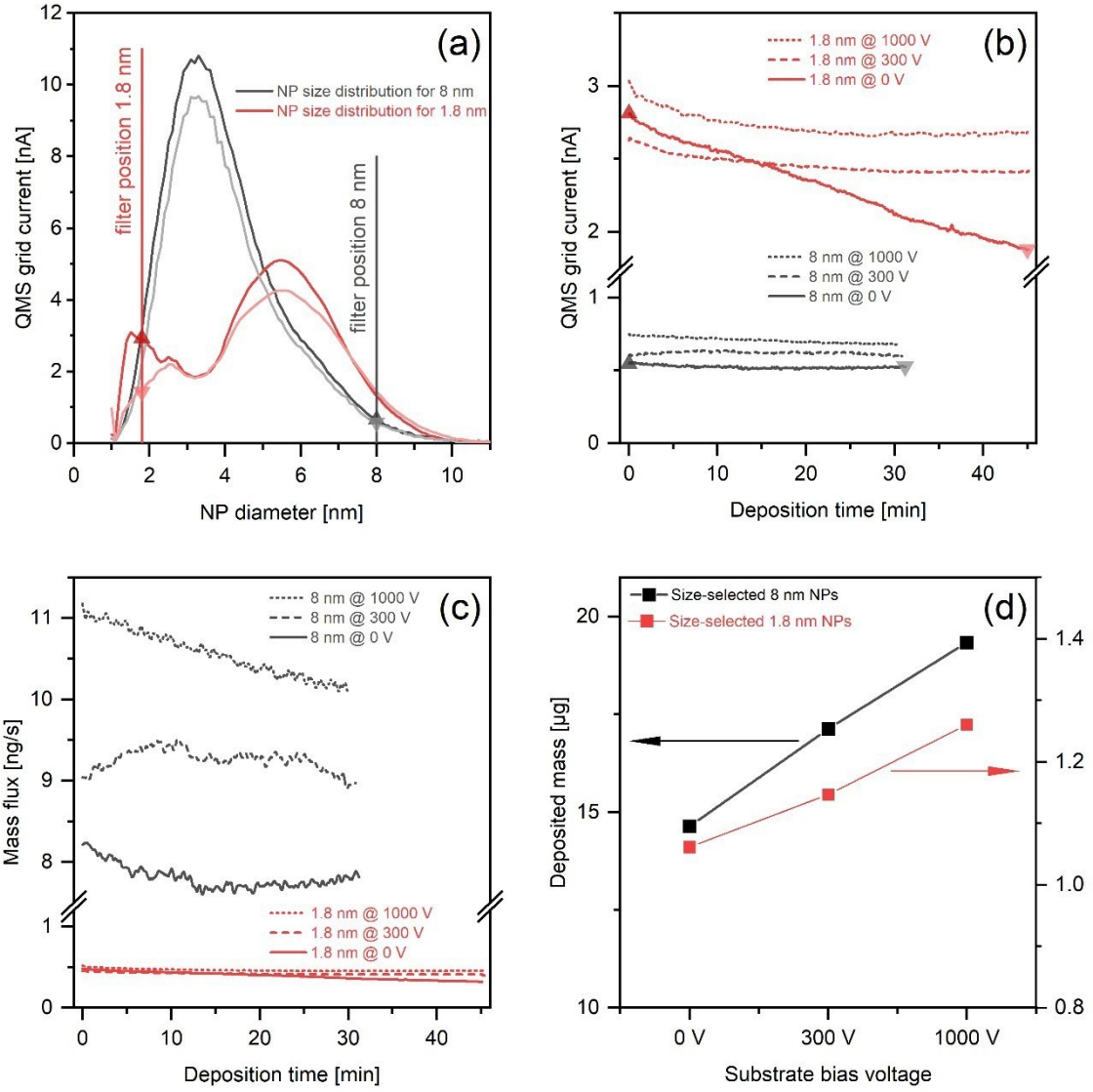

Figure 3. *In situ QMS analysis of NP deposition dynamics. (a) Size distribution of NPs before (darker shade) and after (lighter shade) deposition. Filter positions are indicated by vertical lines. (b) Temporal evolution of QMS grid current, indicative of the NP flux during deposition. Both in panels (a) and (b) up-pointing (▲) and down-pointing (▼) triangles indicate the QMS grid current at the beginning and end of the deposition time. (c) Temporal evolution of the calculated mass flux, showing the impact of the substrate bias voltage on the deposition rates for NPs of both sizes. (d) Relationship between applied substrate bias voltage and the resulting NP deposition mass, taking the deposition time into account*

These distributions were selected for our experiments, given that they yielded robust QMS grid current signals (indicative of the NP flux in NPs s^{-1}) for our targeted NP sizes of 8 and

1.8 nm. The filter positions are indicated with vertical lines in Figure 3a and the corresponding QMS grid currents recorded at the start and end of the depositions are marked by up-pointing (▲) and down-pointing (▼) triangles, respectively. We opted not to select the peaks from the NP size distributions in favor of achieving a more substantial difference in NP mass. By comparing NP size distributions before and after deposition, we confirmed that the process maintained a comparable NP size range consistently across all experiments.

During deposition, the QMS was operated in filter mode, allowing only size-selected NPs of either 8 nm or 1.8 nm to deposit on the substrate and the QMS grid current was monitored to assess the size-specific NP flux, as shown in Figure 3b. Notably, the 1.8 nm NPs without substrate bias experienced a significant 50.7 % reduction in deposition rate over the 45 min time, the most substantial change observed within the investigated time-period. Depositions at 300 V and 1000 V for 1.8 nm NPs showed similar, albeit less dramatic, decreases, aligning with documented behavior in MS-IGC literature. [10,15,17,24–26] This pronounced effect at 0 V for 1.8 nm NPs is likely due to the shorter aggregation length used in their synthesis, rendering the MS-IGC process more sensitive to subtle variations, such as target erosion. The 8 nm samples display a significantly lower absolute grid current and thus NP flux. This is, however, offset by the difference in mass with an 8 nm NP possessing approximately 90 times more mass than a 1.8 nm NP. As depicted in Figure 3b, the QMS results indicate that an elevated substrate bias voltage leads to an increase in the grid current signal for 8 nm NPs as well, implying a greater deposition rate of NPs.

In Figure 3c, the QMS grid current, which reflects the nanoparticle flux in NPs s^{-1}, is converted into the corresponding mass flux in ng s^{-1}.[13] Due to the significant mass disparity between 8 nm and 1.8 nm NPs, fewer 8 nm NPs can generate a substantially greater mass flux. This is because the mass flux $\dot{m}$ is obtained by multiplying the NP's mass m by its flux, the latter being directly proportional to the QMS grid current I_{QMS}, thus $\dot{m} \propto I_{QMS} \times m$.

With increasing substrate bias voltage, there is an anticipated rise in the mass of deposited 8 nm NPs. While two of the three recorded curves adhere to the commonly observed trend of decreasing NP flux throughout the deposition process, the curve at 300 V deviates, exhibiting a slight uptick in deposition rate over time — rising from 9.0 to 9.5 ng s^{-1} and then approximating the initial value after a 30 min deposition period. The observed phenomenon can be attributed to two competing effects; firstly, a reduction in the deposition rate originating from a decrease in oxygen impurities in the aggregation chamber;[10] and secondly, a gradual shift in the NP size distribution towards larger mean sizes, a consequence of ongoing race track formation.[17] Integration of the data from Figure 3c yields the total deposited mass, as illustrated in Figure 3d. Consistent with the already discussed

observations, these results underscore the trend that the deposited mass escalates with an increase in substrate bias voltage for both NP sizes.

2.2. Nanoparticle thin film morphology

SEM micrographs captured near the NP beam center (position indicated in Figure 5d), where NP loading reaches its maximum, are presented in Figure 4, for both NP sizes. These images indicate a more pronounced coverage with NPs with higher substrate bias voltage, thus indicating enhanced material deposition and thin film thickness.

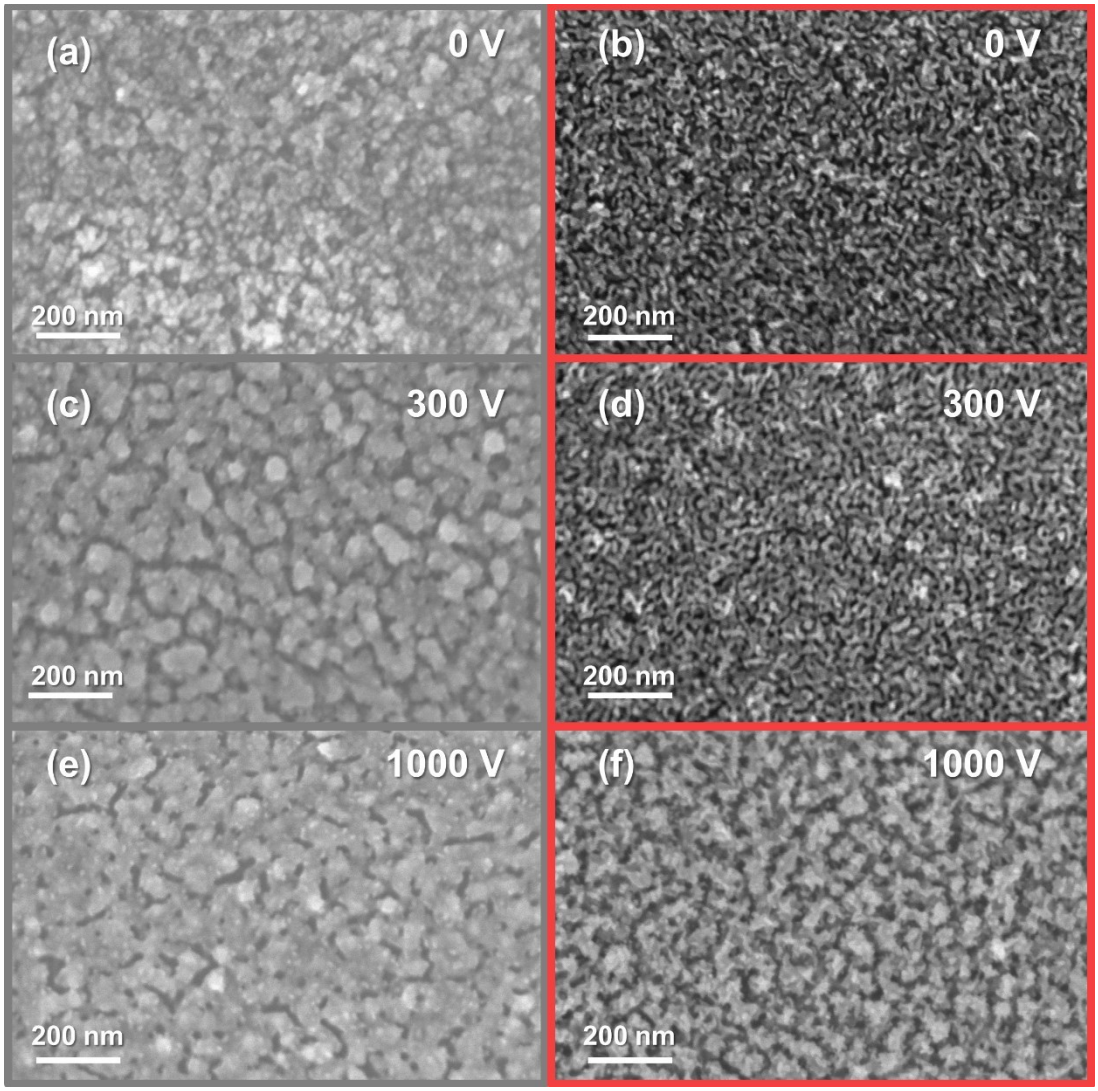

Figure 4. *SEM micrographs of thin films created from size-selected 8 nm (left side) and 1.8 nm (right side) NPs deposited at substrate bias voltages of 0 V (a-b), 300 V (c-d), and 1000 V (e-f). The micrographs indicate an increase in deposited material and distinct morphological changes with rising substrate bias voltage. Micrographs were captured near the NP beam center to highlight the region of maximum NP loading.*

The film thickness of our sample series ranges from 10 nm for 1.8 nm NP samples to 40 nm for 8 nm NP samples, as determined by cross-sectional focused ion beam (FIB) analysis. Additionally, the morphology undergoes a notable transformation with increasing substrate bias voltage. Specifically, size-selected 8 nm NPs (Figure 4a, 4c, 4e) transition from a semi-dense distribution to larger agglomerates as the substrate bias voltage increases, leading to less pronounced surface features and fewer open channels separating the agglomerates. At 1000 V, the thin film becomes denser with larger agglomerates and a reduction of channels. In summary, the application of a substrate bias voltage not only increases NP loading but also induces significant morphological changes, resulting in a denser thin film.

For the 1.8 nm size-selected NP thin films, a uniform distribution of finely dispersed NPs characterizes the morphology at 0 V (see Figure 4b, 4d, 4f). As the substrate bias voltage increases, a higher NP loading is evident, where the surface of the formed thin film transitions from small, finely distributed agglomerates to slightly larger, possibly patterned morphologies. At 1000 V, the morphology markedly shifts to even larger agglomerates, separated by clearly defined channels. In conclusion, increasing the substrate bias voltage enhances NP loading and promotes the coarsening of the surface topography.

Image analysis of the presented high-resolution SEM micrographs was conducted to assess the prevalence of channels or pores on the sample surface, showing a decrease in the area attributed to channels or pores with increasing substrate bias voltage for both NP sizes.

An examination of the morphological evolution from the center of the NP beam outward reveals a notable decrease in NP loading. This observation is in agreement with subsequent findings from XPS and LEIS investigations, detailed in the following paragraphs, and an earlier study by our group.[13]

2.3. Nanoparticle coverage

To quantify NP deposition, XPS analysis was conducted, investigating the surface chemical composition within the topmost 5 – 10 nm layer of the deposited NP thin films. Figure 5a summarizes representative wide-scan XPS spectra near the beam center, confirming the presence of Si, C, O, and Cu elements. Notably, the Cu peak intensity demonstrates a positive correlation with substrate bias voltage, suggesting an increased copper accumulation at higher substrate bias voltages. This trend is confirmed by the high-resolution Cu spectra shown in Figure 5b, which indicate a progressive rise in Cu content for both NP diameters as the substrate bias voltage is increased. In contrast, high-resolution Si scans reveal only minor Si signals, which diminish as the substrate bias voltage increases. Peak fitting indicates that the Si signals comprise both covalently bonded Si^0 (99.4 eV) and Si^{4+} (103.5 eV),[27] the latter of which are indicative of the native SiO_2 oxide layer on the substrate.

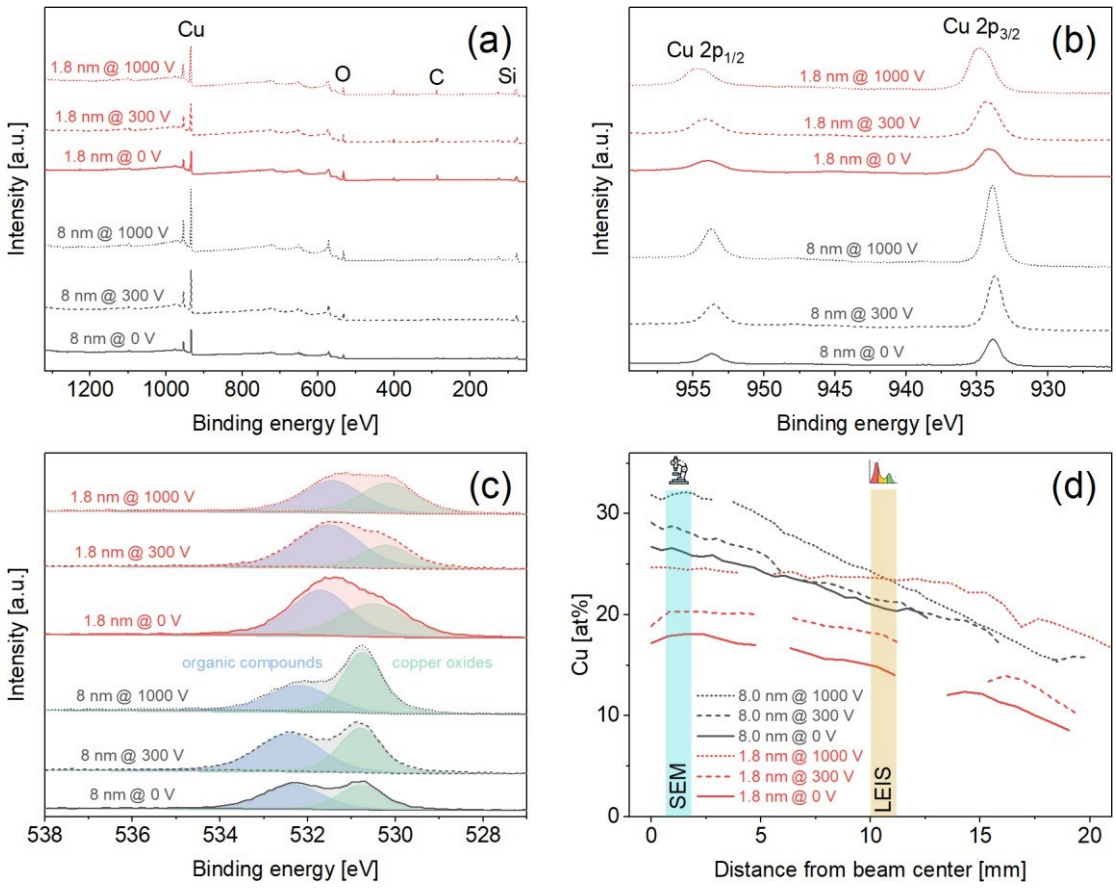

Figure 5. *Results from XPS analysis comparing thin films of size-selected 8 nm (black) and 1.8 nm (red) NPs deposited on Si substrates, showing the influence of substrate bias voltage on chemical composition and distribution. (a) XPS survey spectra highlighting the presence of elemental peaks for Cu, O, C, and Si. (b) High-resolution Cu spectra, showing an increase in Cu content with increasing substrate bias voltage. (c) High resolution O spectra, revealing contributions from organic compounds and copper oxides. (d) Quantitative analysis of Cu loading (in at%) plotted against the distance from the center of nanoparticle beam, illustrating the spatial distribution of NPs on the substrate. Approximate positions of SEM micrographs and LEIS measurements are indicated by the shaded regions. Data points overlapping with sample clamps were omitted to avoid skewed results.*

Due to inherent difficulties in performing an accurate peak fitting of Cu 2p photoemission spectra,[28] we performed peak fitting on the O 1s spectra (Figure 5c). This revealed contributions from both organic carbon-oxygen bonds most likely associated with adventitious carbon as well as copper oxide bonds.[29,30] For the 8 nm NP samples, an increase of copper oxide content with substrate bias voltage is clearly visible. 1.8 nm NP samples showed higher organic compound contributions alongside copper oxide, and no clear trend in copper oxide levels with bias voltage was observable. It has to be noted that organic compounds and possible contributions from SiO_2 cannot be discriminated due to their similar

peak positions. However, based on the survey scans as well as the negligible high-resolution Si signal, peaks at higher binding energies are likely tied to organic compounds. Detailed investigations on the NP oxidation behavior are not within the scope of this manuscript and were already performed by other authors.[31,32]

Quantitative XPS analysis revealed a gradual decrease in Cu content (representative of NP loading of the Si substrate surface) with increased distance from the beam center, shown in Figure 5d. This is consistent with SEM observations and a prior study.[13] Additionally, also here the Cu content demonstrates a positive correlation over the whole distance from the beam center with substrate bias voltage, with Cu loading in size-selected 8 nm depositions rising from 26 at% to 32 at% at the beam center. A similar pattern was observed for the 1.8 nm samples. Notably, the lateral spread of NPs remained consistent across varying substrate bias voltages, suggesting that the electric field does not significantly influence the lateral distribution of NP deposition. Carbon contamination was present, accounting for 20 to 35 at% of the surface composition for 8 nm and 1.8 nm NPs, respectively. Silicon and oxygen levels rose with distance from the beam center, with silicon showing an increment from 15 at% to 20 at% for the 8 nm NPs, and from 5 at% to 20 at% for the 1.8 nm NPs. Oxygen displayed a similar pattern, increasing from about 25 at% to 40 at% some 20 mm away from the beam center. In summary, the XPS results corroborate the trends observed in the *in situ* QMS data, with a higher Cu NP loading for 8 nm depositions compared to 1.8 nm NPs, albeit the difference is small. However, the increase in Cu loading with rising substrate bias voltage is clearly evident, while the lateral NP distribution remains unaffected by the substrate bias voltage.

2.4. Surface chemistry

LEIS offers even greater surface sensitivity than XPS, owing to its reliance on the scattering of low-energy ions, which probes only the outermost atomic layer.[33] This technique provides insights from the surface with minimal penetration depth, with representative 3 keV He^+ LEIS spectra depicted in Figure 6a, which predominantly reveal Cu and O on the sample surface, alongside a minor Si presence. A gentle sputter cleaning using Ar ions, conducted before measurements within the vacuum chamber, effectively removed organic contaminants from the surface, as evidenced by the absence of a C signal and the low background noise.

Figure 6b illustrates an increase in the Cu signal as the substrate bias voltage rises, with all spectra captured at an intermediate distance of 10 mm from the NP beam center. Spatially resolved LEIS measurements confirmed a decrease in the Cu signal with increasing distance

from the NP beam center. LEIS data does not allow to distinguish between the oxidation states of Cu,[33] or assign the detected oxygen to either the copper oxide or SiO_2.

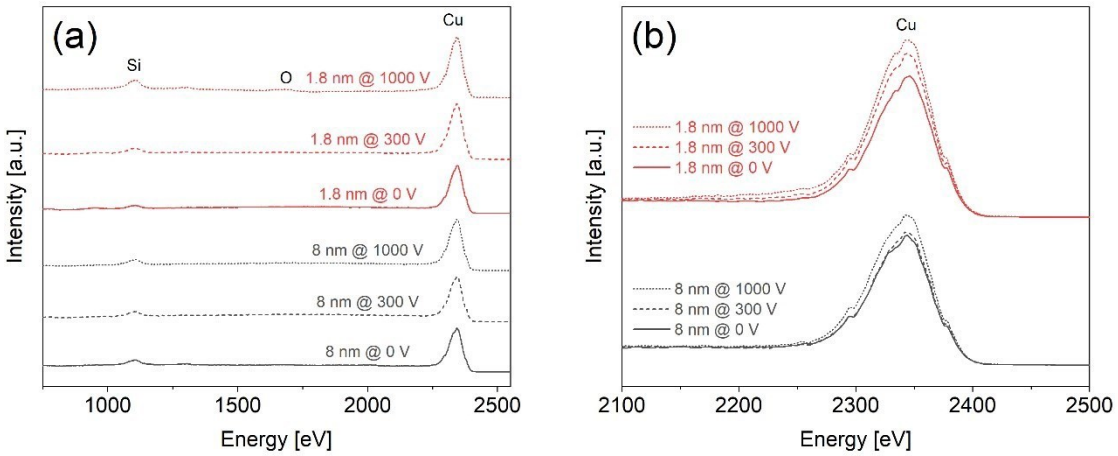

Figure 6. *Results from LEIS analysis comparing thin films of size-selected 8 nm (black) and 1.8 nm (red) NPs deposited on Si substrates, showing the influence of substrate bias voltage on chemical composition of the top atomic layer. (a) LEIS 3 keV He^+ spectra highlighting the presence of elemental peaks for Cu, O, and Si. (b) Cu spectra, showing an increased Cu signal with increasing substrate bias voltage.*

LEIS provided a stronger Cu signal for 1.8 nm samples than for 8 nm samples at the same substrate bias voltage. This is not the case for XPS, implying that the greater number of small Cu NPs are capable of achieving a greater surface coverage compared to the lower number of large 8 nm NPs. Thus, in summary, LEIS not only corroborates the XPS findings but also underscores the ability to enhance surface coverage — and consequently, the NP deposition rate — with increased substrate bias voltage.

Conducting a quantitative analysis of thin NP deposits, especially those with a thickness below 10 nm, presents notable challenges. XPS encounters its own limitations with an informational depth capped at approximately 10 nm. From comparison and agreement between our XPS and LEIS data, we can conclude that our Cu NP deposits are equal or thicker than 10 nm in the center of the NP beam. This is in good agreement with the findings derived by FIB cross-sectional analysis.

2.5. Enhanced nanoparticle source efficiency

The observed increase in the QMS grid current signal as a function of the substrate bias voltage suggests a rise in NP flux. To confirm that this signal indeed represents a true increase in NP yield and is not an artifact of the measurement process, we undertook a validation exercise.

One could argue that the applied substrate bias voltage affects the electric circuit of the quadrupole mass spectrometer grid, where small currents in the range of nA are measured. However, this is unlikely as the quadrupole mass spectrometer grid operates on a battery-powered circuit, ensuring it remains isolated and independent from the deposition system's power supply. Furthermore, one could speculate that the applied substrate bias voltage affects the plasma present within the deposition chamber, therefore affecting the QMS grid current signal due to the detection of plasma-derived charged species. Such a substrate bias voltage, in particular if pulsed, would certainly affect the plasma properties. However, in the case of MS-IGC, the plasma is confined within the aggregation zone. If any plasma-derived charged species, such as electrons or charged Ar ions, were to leave the aggregation chamber and reach the expansion zone containing the quadrupole mass spectrometer, they would be ejected within the quadrupole field due to their incorrect mass-to-charge ratio, thus not affecting the detected QMS grid current signal.

The presence of a plasma within the deposition chamber renders the QMS grid current signal useless due to charged species arriving at the grid. This was confirmed by performing a co-deposition of NPs along with conventional cobalt sputtering using the planar 50.8 mm magnetron sputter target located within the main deposition chamber.[13] Once the conventional sputter process commences within the deposition chamber, the QMS grid current signal becomes non-viable.

Curda et al. simulated an electrostatic field within a MS-IGC deposition chamber under comparable conditions using a potential of ±100 V, proving that NPs are affected in a distance of few cm.[34] This suggests that the provided substrate bias voltage is of sufficient strength to affect NPs traversing through the quadrupole and possibly even within the aggregation chamber. However, the latter is less likely, as the aggregation chamber is grounded and the orifice has an opening of only 3 mm.

The reason for the increased NP deposition cannot clearly be pinpointed as of now. We suggest that it is not associated with a higher NP production rate, but rather with reduced losses. This could be associated either with an increased ratio of NPs leaving the aggregation chamber rather than being lost to the chamber walls, or a reduced filtering resolution of the quadrupole mass spectrometer, with the latter as the more likely reason.

The QMS records *in situ* the entire NP flux passing from the NP source into the main chamber. Only a fraction of these recorded NPs land on different positions of the substrate holder for subsequent analysis. The application of a substrate bias voltage clearly enhanced the QMS grid signal, a direct measure of the amount of extracted NPs. Within the tested range, the maximum increase was recorded at 32 % for the case of 8 nm samples. However, no

general statements can be made, as the increase is likely to depend on various synthesis parameters and appears to be NP-size-dependent. Furthermore, MS-IGC suffers from a low repeatability. The phenomenon of enhanced NP flux was reversible, with the magnitude of the observed effect substantially exceeding the well-known decrease in deposition rate over time (see Figure 3b) due to erosion-induced race track formation on the target[17] and a decrease in oxygen impurities in our system's aggregation chamber.[10]

The notion of an improved NP efficiency of the NP source is in contrast to the well-established fundamentals of thin film growth on biased substrates,[35] which lead to a densification of the film morphology and to reduced growth rates due to re-sputtering effects. In MS-IGC in conjunction with QMS, such an electric field is unlikely to significantly change the sputter conditions around the sputter target due to the de-coupled nature of the individual highly functionalized process chambers.

2.6. Discussion on nanoparticle thin film formation mechanisms

Increasing the kinetic energies of single-charged NPs by 300 eV and 1000 eV constitutes a considerable addition to the NPs' total energy, significantly influencing the NP-surface interaction. In literature, three principal deposition regimes, namely soft landing, pinning, and implantation, are distinguished by their respective kinetic energy per atom.[23]

This is particularly relevant when considering the vast difference in atom numbers between small (approximately 260 atoms for spherical 1.8 nm NPs) and large NPs (about 23,000 atoms for 8 nm NPs). With an assumed speed of 100 m s^{-1}[36] and thus a kinetic energy below 0.01 eV $atom^{-1}$ for non-accelerated NPs, the application of a 1000 V substrate bias voltage to 1.8 nm negatively charged NPs results in an energy of approximately 4 eV $atom^{-1}$, surpassing the threshold for soft landing[23] and reaching beyond the intermediate pinning regime into the implantation regime, as the binding energy of small Cu clusters can be expected to be in the range of 2 eV $atom^{-1}$.[37] The chosen range of substrate bias voltages in this work thus provides a comprehensive spectrum of nanoparticle landing conditions.

In his early work, Haberland et al. already applied a positive substrate bias voltage to accelerate metallic NPs towards the substrate, resulting in the formation of highly reflective and strongly adhering Mo NP films on polished Cu substrates.[8,19] Size-selected Ag NPs were studied by Shyjumon et al. under substrate bias voltages ranging from -500 to -2500 V to attract positively charged NPs, noting an increasing flattening of NPs with increasing kinetic energy.[21] These findings are in line with our own, where we noted a densification in the thin film's structure corresponding with an increase in substrate bias voltage. The underlying mechanism can be attributed to the high-velocity impacts (e.g., single-charged 1.8 nm NPs with a kinetic energy of 1000 eV at a 1000 V bias voltage reach speeds of 3500 m s^{-1}), which

create localized high-temperature spots upon each NP's impact.[19] In the case of the non-accelerated NPs forming thin films, only negligible NP deformation is expected for both small and large NPs.[23] With rising impact energy, increased flattening and plastic deformation is expected. In the case of 8 nm NP samples deposited at 1000 V, despite a low total impact energy of around 0.05 eV atom^{-1}, this still represents an increase of more than 1000 % in impact energy compared to the non-accelerated deposition, with an impact velocity of ~ 400 m s^{-1}, thus explaining the observed changes in the morphology as a function of the substrate bias voltage.

Regarding morphological changes, Rattunde et al.[20] reported two opposing effects related to the application of a substrate bias voltage up to 30 kV to Cu NPs: For initially rough substrate surfaces, a smoothening is observed, while impinging NPs logarithmically increase the roughness of an initially smooth surface. Michelakaki et al.[22] demonstrated that by adjusting the substrate bias voltage to alter the kinetic energy of Hf NPs, one can produce porous thin films, whose mechanical properties increasingly resemble those of conventionally sputtered ones as the substrate bias voltage rises. This mechanical similarity to dense sputtered films is in agreement with our observations of increased density with increasing bias voltage.

3. Conclusions

In this study, we have demonstrated that the application of a substrate bias voltage can significantly increase the deposition rate of size-selected nanoparticles by magnetron sputter inert gas condensation coupled with quadrupole mass spectrometry. This enhanced nanoparticle yield was monitored *in situ* for different nanoparticle sizes and subsequently verified through scanning electron microscopy, X-ray photoelectron spectroscopy, and low-energy ion scattering spectroscopy. Our results indicate a significant enhancement of up to 32 % in surface coverage by NPs with increasing substrate bias voltage, along with a distinct evolution in surface morphology, illustrating the beneficial impact of the kinetic energy on film characteristics. The advancements in process efficiency detailed in this work mark a step forward in the optimization of magnetron sputter inert gas condensation for industrial applications.

4. Experimental Section

4.1. Materials

Cu NPs were produced by magnetron sputter inert gas condensation using Cu targets supplied by Kurt J. Lesker Company Ltd, with a purity of 99.999 %, a diameter of 25.4 mm, and a thickness of 3.2 mm. Cut single-crystal Si (100) wafers with a thickness of 525 µm (MicroChemicals GmbH) were employed as substrates.

To ensure a clean substrate surface for the deposition of NPs, a two-step cleaning process was implemented. Initially, samples were ultrasonically cleaned for 10 min in an isopropanol bath and subsequently dried using hot air. The substrates were then exposed to a low-pressure plasma environment using a Tetra 30 plasma system by Diener electronic. During this stage, an Ar gas flow was maintained at 80 sccm, and the plasma was generated at 20 % of the system's full power capacity of 1 kW for a duration of 10 min, effectively removing any remaining contaminants and preparing the substrate surface for NP deposition.

4.2. Nanoparticle synthesis

Cu NPs were synthesized using an NL NL-DX3 nanoparticle deposition source (Nikalyte Ltd) attached to a MiniLab 125 deposition system (Moorfield Nanotechnology Ltd), with an extensive description of the system available in an earlier work.[13] NP nucleation and growth occurs within an aggregation chamber containing three individual metal targets, where only one Cu target was sputtered within this work. The length of the aggregation chamber, which we define as the distance between the metal targets and the 3 mm orifice terminating the aggregation chamber, can be tuned using a linear translator, thus influencing the NP growth conditions within the chamber. After terminating the aggregation chamber, the NPs arrive in a differentially pumped expansion zone, and further growth is assumed to stop. NPs leaving the aggregation chamber are assumed to be fully developed, roughly spherical, carrying mostly a single electric charge. In the subsequent expansion zone, a QMS is situated. With the assumptions of a spherical nanoparticle shape, a single electric charge, and a crystal density equivalent to that of bulk copper (9.0 $cm^3\ g^{-1}$), the NP size distribution can be calculated. The NP flux is measured using the current detected at a grid located at the exit of the QMS. As outlined in an earlier study, the recorded data can be used to calculate the mass flux and the total deposited NP mass.[13]

Substrates were mounted on the sample holder and subjected to a constant rotation speed of 10 rpm during deposition to ensure uniform coverage, without the application of external heating. The deposition processes were conducted under a base pressure below 5×10^{-5} Pa, with operational pressures reaching 0.17 Pa for 8 nm NPs and 0.13 Pa for 1.8 nm NPs within the deposition chamber.

For the 8 nm size-selected NPs, deposition parameters were set to a 30 min duration, an argon gas flow rate of 70 sccm, an aggregation length of 90 mm, and a sputter current of 200 mA. For 1.8 nm size-selected NPs, an Ar flow of 40 sccm, an aggregation length of 60 mm, and a sputter current of 200 mA was used for a total deposition time of 45 min. Deposition parameters were chosen to achieve robust QMS grid current signals, as detailed in Section 2.1. For all samples, the same target was utilized to maintain consistency across all samples.

Prior and after deposition, the quadrupole mass spectrometer was used to determine the NP size distribution, operating in positive grid bias mode. Throughout the deposition process, nanoparticles were filtered by size (specifically 8 or 1.8 nm, equivalent to 1.44×10^6 amu and 1.64×10^4 amu, respectively) and continuously monitored throughout the deposition. The chosen positive substrate bias voltage (0 V, 300 V, 1000 V) was applied, then the substrate shutter was opened, resulting in a distinct step in the detected grid current. NP size distributions were recorded with a closed shutter and at 0 V for all samples, to ensure comparable measurement conditions and to allow for direct comparison of the deposition process without taking the effect of the substrate bias voltage into account.

4.3. Characterization methods

SEM micrographs were recorded using a Hitachi S4800 scanning electron microscope. All micrographs were recorded using a secondary electron detector for surface topology with an acceleration voltage of 3 kV. FIB cross-sections and corresponding SEM micrographs to estimate the NP thin film thickness were made in a Tescan Lyra3. The NP thin film was protected by electron and ion beam deposited Pt layers. Cross-sectional FIB milling was conducted by step-wise reduction of the ion current from 2 nA to around 25 pA. The corresponding film thicknesses were measured by tilting of the sample and using the built-in tilt correction.

Image analysis of SEM micrographs for assessing the morphological development was performed in ImageJ. For this purpose, a Gaussian blur filter was used to reduce noise in the micrographs. Three greyscale thresholds were used to distinguish and quantify unfilled portions or groves of the NP films. Trends in the development of mean size and total number of those pores and the relative unfilled area were evaluated for all depositions.

XPS measurements were carried out with a Thermo Scientific Nexsa G2 x-ray photoelectron spectrometer system, which employs a monochromatic, microfocused, low-power Al Kα x-ray (1486.7 eV) source. The x-ray beam was focused to a spot size of 300 µm. Wide-scan XPS spectra were collected using a pass energy of 100.0 eV with a step size of 1.0 eV. High-resolution XPS spectra were collected using a pass energy of 20.0 eV with a step size of 0.1 eV. Scanning was performed in a rectangular grid with measurements of three

points along the sample width and a distance of 0.5 mm between points, for which homogenous chemical composition is expected due to the rotational symmetry of the deposition. All measurements were conducted on samples without previous baking or sputter-cleaning. To compensate for potential charging effects during the measurement process, all acquired spectra were charge referenced to the C1s peak at 284.8 eV (sp^2 hybridized carbon).

The LEIS spectra were obtained using an ionTOF Qtac100 spectrometer, employing He ions as the probing species with an energy of 3 keV. The primary ion beam was directed at the sample surface with a perpendicular incidence angle, and scattered ions were detected at a scattering angle of 145°. Prior to each measurement, the samples were cleaned *in situ* by sputtering with an Ar ion beam of 1 keV for 25 s. A time of flight filter was used to reduce the background signal from lighter elements.

Acknowledgements

Funding support by the Austrian Research Promotion Agency (FFG, Project Nr. 896659 AMAGADE) and Gesellschaft für Forschungsförderung Niederösterreich (Project FTI21-D002) is gratefully acknowledged. Barbara Putz acknowledges funding from the Swiss National Science Foundation under the Ambizione grant agreement No PZ00P2_202089.

References

[1] Y. Zhou, C. Jin, Y. Li, W. Shen, *Nano Today* **2018**, *20*, 101.

[2] Y. J. Lin, S. J. Ding, K. Chen, D. J. Yang, Y. Xie, Z. H. Hao, L. Zhou, Q. Q. Wang, *J. Nanoparticle Res.* **2019**, *21*, 137.

[3] S. Haviar, J. Čapek, Š. Batková, N. Kumar, F. Dvořák, T. Duchoň, M. Fialová, P. Zeman, *Int. J. Hydrogen Energy* **2018**, *43*, 22756.

[4] N. Kostoglou, C. W. Liao, C. Y. Wang, J. N. Kondo, C. Tampaxis, T. Steriotis, K. Giannakopoulos, A. G. Kontos, S. Hinder, M. Baker, E. Bousser, A. Matthews, C. Rebholz, C. Mitterer, *Carbon* **2021**, *171*, 294.

[5] M. Vaidulych, A. Shelemin, J. Hanuš, I. Khalakhan, I. Krakovsky, P. Kočová, H. Mašková, J. Kratochvíl, P. Pleskunov, J. Štěrba, O. Kylián, A. Choukourov, H. Biederman, *Plasma Process. Polym.* **2019**, *16*, 1900003.

[6] N. Khomiakova, D. Nikitin, A. Kuzminova, M. Cieslar, Y. Al-Muhkhrabi, D. Kahoun, J. Lieskovská, J. Hanuš, J. Kratochvíl, P. Pleskunov, J. Vyskočil, A. Choukourov, O. Kylián, H. Biederman, *Vacuum* **2023**, *217*, 112586.

[7] T. Patlejchová, E. Kratochvílová, H. Mašková, D. Kahoun, O. Kylián, Y. Al-Muhkhrabi, O. Mashchenko, J. Štěrba, J. Kratochvíl, *ACS Appl. Nano Mater.* **2023**, *6*, 23090.

[8] H. Haberland, M. Karrais, M. Mall, *Zeitschrift für Phys. D Atoms, Mol. Clust.* **1991**, *20*, 413.

[9] O. Polonskyi, P. Solař, O. Kylián, M. Drábik, A. Artemenko, J. Kousal, J. Hanuš, J. Pešička, I. Matolínová, E. Kolíbalová, D. Slavínská, H. Biederman, *Thin Solid Films* **2012**, *520*, 4155.

[10] O. Polonskyi, O. Kylián, M. Drábik, J. Kousal, P. Solař, A. Artemenko, J. Čechvala, A. Choukourov, D. Slavínská, H. Biederman, *J. Mater. Sci.* **2014**, *49*, 3352.

[11] M. Ganeva, T. Peter, S. Bornholdt, H. Kersten, T. Strunskus, V. Zaporojtchenko, F. Faupel, R. Hippler, *Contrib. to Plasma Phys.* **2012**, *52*, 881.

[12] V. N. Popok, L. Gurevich, *J. Nanoparticle Res.* **2019**, *21*, 171.

[13] F. Knabl, C. Bandl, T. Griesser, C. Mitterer, *J. Vac. Sci. Technol. A* **2024**, *42*, 023201.

[14] Y. Huttel, L. Martínez, A. Mayoral, I. Fernández, *MRS Commun.* **2018**, *8*, 947.

[15] A. Marek, J. Valter, S. Kadlec, J. Vyskočil, *Surf. Coat. Technol.* **2011**, *205*, S573.

[16] G. Krishnan, S. de Graaf, G. H. ten Brink, P. O. Å. Persson, B. J. Kooi, G. Palasantzas, *Nanoscale* **2017**, *9*, 8149.

[17] M. Ganeva, A. V. Pipa, R. Hippler, *Surf. Coat. Technol.* **2012**, *213*, 41.

[18] S. Ali-Ogly, J. Kousal, D. Nikitin, P. Pleskunov, J. Hanuš, A. Choukourov, H. Biederman, *J. Phys. D. Appl. Phys.* **2022**, *55*, 12.

[19] H. Haberland, M. Karrais, M. Mall, Y. Thurner, *J. Vac. Sci. Technol. A* **1992**, *10*, 3266.

[20] O. Rattunde, M. Moseler, A. Häfele, J. Kraft, D. Rieser, H. Haberland, *J. Appl. Phys.* **2001**, *90*, 3226.

[21] I. Shyjumon, M. Gopinadhan, O. Ivanova, M. Quaas, H. Wulff, C. A. Helm, R. Hippler, *Eur. Phys. J. D* **2006**, *37*, 409.

[22] I. Michelakaki, N. Boukos, D. A. Dragatogiannis, S. Stathopoulos, C. A. Charitidis, D. Tsoukalas, *Beilstein J. Nanotechnol.* **2018**, *9*, 1868.

[23] V. N. Popok, I. Barke, E. E. B. Campbell, K. H. Meiwes-Broer, *Surf. Sci. Rep.* **2011**, *66*, 347.

[24] G. E. Johnson, R. Colby, J. Laskin, *Nanoscale* **2015**, *7*, 3491.

[25] W. Chamorro-Coral, A. Caillard, P. Brault, P. Andreazza, C. Coutanceau, S. Baranton, *Plasma Process. Polym.* **2019**, *16*, e1900006.

[26] A. Kusior, K. Kollbek, K. Kowalski, M. Borysiewicz, T. Wojciechowski, A. Adamczyk, A. Trenczek-Zajac, M. Radecka, K. Zakrzewska, *Appl. Surf. Sci.* **2016**, *380*, 193.

[27] F. J. Himpsel, F. R. McFeely, A. Taleb-Ibrahimi, J. A. Yarmoff, G. Hollinger, *Phys. Rev. B* **1988**, *38*, 6084.

[28] J. A. Torres-Ochoa, D. Cabrera-German, O. Cortazar-Martinez, M. Bravo-Sanchez, G. Gomez-Sosa, A. Herrera-Gomez, *Appl. Surf. Sci.* **2023**, *622*, 156960.

[29] Thermo Fisher Scientific Inc., Oxygen X-ray photoelectron spectra, oxygen electron configuration, and other elemental information, https://www.thermofisher.com/at/en/home/materials-science/learning-center/periodic-table/non-metal/oxygen.html, accessed: March, 2024

[30] S. Poulston, P. M. Parlett, P. Stone, M. Bowker, *Surf. Interface Anal.* **1996**, *24*, 811.

[31] V. N. Popok, S. M. Novikov, Y. Y. Lebedinskij, A. M. Markeev, A. A. Andreev, I. N. Trunkin, A. V Arsenin, V. S. Volkov, *Plasmonics* **2021**, *16*, 333.

[32] F. Zamboni, A. Makarevičiūtė, V. N. Popok, *Appl. Nano* **2022**, *3*, 102.

[33] C. V Cushman, P. Brüner, J. Zakel, G. H. Major, B. M. Lunt, N. J. Smith, T. Grehl, M. R. Linford, *Anal.*

Methods **2016**, *8*, 3419.

[34] P. Curda, D. Kaftan, T. Kozak, S. Kumar, P. Sezemský, V. Stranak, *Appl. Surf. Sci.* **2023**, *640*, 158307.

[35] I. Petrov, P. B. Barna, L. Hultman, J. E. Greene, *J. Vac. Sci. Technol. A* **2003**, *21*, S117.

[36] P. Solař, K. Škorvánková, A. Kuzminova, J. Kousal, O. Kylián, *Vacuum* **2022**, *202*, 111114.

[37] Y. D. Qu, X. L. Liang, X. Q. Kong, W. J. Zhang, *Phys. Met. Metallogr.* **2017**, *118*, 528.

9 Appendix: Declaration of the Use of AI-Based Tools

The purpose of this appendix is to outline the areas within this thesis where AI tools have been utilized in order to comply with the “Richtlinie des Vizerektors für Lehre und Internationales sowie des Studiendekans für den Einsatz KI-basierter generativer Werkzeuge”, as published in "Mitteilungsblatt 108" on April 4, 2024, only a few days before thesis submission.

The author would like to point out that the percentages indicated in the “AI contribution” column represent an estimated extent of the AI-assisted work. This is distinct from “fully AI-generated work”, which does not apply to this thesis.

Table 1: AI contribution to different subjects of this thesis

Subject	AI contribution	Tool/ Version	Comments	Prompts
Software code	50 %	ChatGPT 3.5, ChatGPT 4.0	Mainly used for writing code with respect to data handling for quadrupole mass spectrometry and X-ray photoelectron spectroscopy	
Analysis and interpretation of data	20 %	ChatGPT 3.5, ChatGPT 4.0	Minor contribution as a side effect of AI-generated feedback on text provided by the author.	
Discussions, descriptions, conclusions	20 %	ChatGPT 3.5, ChatGPT 4.0	Minor contribution as a side effect of AI-generated feedback on text provided by the author.	
Conceptualization, brainstorming, and idea collection	20 %	ChatGPT 3.5, ChatGPT 4.0	Minor contribution as a side effect of AI-generated feedback on text provided by the author.	
Enhancement of language clarity	20 %	ChatGPT 3.5, ChatGPT 4.0	Main application of AI within this thesis. Common prompts used include: • Review this text • Provide suggestions for improvement • Suggest three alternative phrases to (mediocre phrase)	
Paraphrasing	20 %	ChatGPT 3.5, ChatGPT 4.0	“Paraphrasing” and “enhancement of language clarity” cannot be separated from each other, thus the same statements applies.	
Structuring the thesis	5 %	ChatGPT 3.5, ChatGPT 4.0	No relevant contributions, but prompts were used occasionally to ensure completeness.	

The author declares that no AI was used in creating research questions, summarizing text, and translating text. Furthermore, no AI was applied for literature review tasks such as AI-generated suggestions on important literature, extraction of key statements out of scientific publications, or creating excerpts out of scientific publications. Furthermore, no AI support was utilized for creating diagrams, figures, schematic drawings, tables, or any other type of illustration.